





**KU Leuven**  
**Biomedical Sciences Group**  
**Faculty of Pharmaceutical Sciences**  
**Laboratory for Radiopharmaceutical Research**



# **EVALUATION OF NOVEL PET LIGANDS FOR IMAGING NEUROINFLAMMATION**

Bala Attili

Dissertation presented in partial fulfilment of the requirements for the degree of Doctor in Pharmaceutical Sciences

Jury:

Promoter:	Prof. Dr. Guy Bormans
Chair:	Prof. Dr. Myriam Baes
	Prof. Dr. Jef Rozenski
Jury members:	Prof. Dr. Eveline Lescrinier
	Dr. Cindy Casteels
	Prof. Dr. Leonie Wyffels
	Prof. Dr. Bertrand Kuhnast

---

Thursday, June 21, 2018, 4 PM

Auditorium Pentalfa  
Campus Gasthuisberg O&N I  
Herestraat 49  
3000 Leuven.

Promoter: Prof. Dr. Guy Bormans

Laboratory for Radiopharmaceutical Research  
Faculty of Pharmaceutical Sciences  
Herestraat 49, O&N II, box 821  
B-3000 Leuven

---

Dedicated to my Mother, Father and Prof. Guy Bormans

---



## ACKNOWLEDGEMENTS

*Gururbrhama gururvishnuhu  
gururdaevoa maheasvarah  
guru ssaakshaatpara brahma  
tsmai sree guravaenamah*

*Guruvu (Teacher) is revered greatly by us as he is a wealth of knowledge. And by offering our sincere obedience to him we expect to gain knowledge from him. Master or Teacher is the one who would direct us to the path of enlightenment, and save us from the darkness of ignorance. Hence Teacher should be given profound honour and respect.*

For me receiving the doctoral degree is a dream come true. For accomplishing this conquest, many people have significantly contributed over the past four years. I would like to take this occasion to thank everyone.

I would like to express my heartfelt gratitude to my thesis advisor Prof. Guy Bormans for his continuous support throughout my doctoral research. His patience, motivation and immense knowledge have indeed paved the way to my success. His guidance helped in all the time of research and writing this thesis. Guy, thank you very much for the positive learning environment and the wide variety of projects you provided me. Teachers like you are hard to find. I had a great time with you during conferences; I never forget the 100 km walk we did in SfN congress, Washington, USA.

I would like to thank my jury members Prof. Myriam Beas, Prof. Eveline Lescrinier and Dr Cindy Casteels for probing my scientific understanding from the past four years. Your constructive suggestions and critical evaluation have helped me to improve. I appreciate all the hard work you've done on reading and perusing my thesis. Thank you! Prof. Jef Rozenski for agreeing to be the chair of my examination committee. I wish to express my gratitude to my external jury members Prof. Bertrand Kuhnast and Prof. Leonie Wyffels for their time spent on my thesis manuscript and the invaluable suggestions for further improvement.

I am indebted to Dr Sofie Celen for her constant support and encouragement; who never hesitated to run with me for many radiolabelling experiments. Long days spent in the clean rooms are never forgettable.

Special thanks to Dr Muneer Ahamed for the suggestions in organic synthesis and helping me with the NMRs. I got invaluable support from you during my first years; it has been a pleasure working with you.

Much of the work in this dissertation could not be possible without help from you Julie; thanks a lot for your help in the animal work. Ivan, Pieter, Jana, Jeroen and Jan your technical skills and timely advice always been a great support, I am very thankful to you all.

I would like to thank Prof. Alfons Verbruggen and Prof. Matthias Schonberger for your curious questions during lab meetings. They were insightful.

Tjibbe, your experience and troubleshooting skills are remarkable, and I will always be thankful for you. Marva, Kim, Sofie, Bert, Stef, Martin and everyone in the Radiopharmacy from UZ Leuven. I wholeheartedly appreciate everything you have done for me.

---

I thank everyone at Department of Nuclear medicine. Prof. Michel Koole, thank you very much for stimulating discussions and helping me in analysing the complex PET data between your tight schedules. Dr Chris Van den Haute, I enjoyed working with you on the CB2R project. I would like to say thanks Prof. Wim Vanduffel and Christophe Ulens for providing and assisting in monkey studies. Christophe, thank you for your coming with monkeys and patiently waiting until the PET scan finish.

Thank you very much to Dr Steve De Vos, Dr Romain Gosmini, Dr Kenji Shoji, Dr Xavier Bock from Galapagos for the excellent collaboration and scientific knowledge exchange over the past three years. It was a great pleasure working with you.

Dr Petya Georgieva, it was great working with you on TSPO glioma imaging, although the work was not a part of this dissertation. Dr Keimpe Wierda thank you very much for your help in acute brain sections. Manesh, thank you for your help with NMR.

Thanks to MOSAIC colleagues, in particular, Bryan and Sarah for your skilful help and time that is you have spent on cell binding studies. I would like to express my gratitude to Melissa, Shweta, Bart, Akhila, Rita, An, Pieter and Jens.

Maarten, many thanks for your help during my first year in the lab especially with MAGL project and the pleasing talks. Dieter, thanks for sharing tips and tricks in radiochemistry lab as well as the interesting discussions on PET targets for neuroinflammation. Lieven, it was great to work with you, your assistance in metabolite analysis and monkey scans is highly appreciated. Frederik, thanks for being a great buddy in the lab. Thanks for teaching me squash.

Koen 'my Snehituda'- I enjoyed working with you, now it's your time to finish up, and I wish you lot of success. Maxime it was nice working with you together with Eugenia, I wish you good luck for your forthcoming thesis defence.

Uta, many thanks for the conversations we had in and outside the lab. I truly cherish them. Joan and Emilie, thank you very much for your help in organic synthesis. Joost thanks a lot for the lovely time we had in Leuven. Terence, Kaat, Ermal, Yvonne, Ines, Mathilde and Adrian! Thank you all, for giving me a great time in the lab.

I would like to thank An and Chantal for your help in all the administration works during these years.

It is a real honour and pleasure to be a KU Leuven student and alumni in future. The state of art facilities and help from faculty are impressive. I thank INMiND FP-7 consortium for supporting my PhD research.

I would like to thank all my friends Kiran, Sai, Pallavi, Soumya, Satti, Mohan, Sunil, Phani, Mahesh, Vijay, Dammu, Nagaraju, Pranov, Pradeep, Shruti, Abhijith, Eshwar... (never-ending list) for their affection and support.

Last but not the least, I am grateful to my family who always allows me to follow my passions. I thank my better half Aiswarya and her amazing family for their love, belief and care. I am fortunate to have you in my life.

Bala Attili  
Leuven

---



# TABLE OF CONTENTS

<b>LIST OF ABBREVIATIONS</b> .....	<b>III</b>
<b>CHAPTER-I</b> .....	<b>1</b>
GENERAL INTRODUCTION .....	1
AIM AND THESIS OUTLINE .....	29
<b>CHAPTER-II</b> .....	<b>31</b>
SYNTHESIS AND PRECLINICAL EVALUATION OF [ <sup>11</sup> C]MA-PB-1 FOR <i>IN VIVO</i> IMAGING OF BRAIN MONOACYLGLYCEROL LIPASE (MAGL) .....	31
<b>CHAPTER-III</b> .....	<b>57</b>
PRECLINICAL EVALUATION OF [ <sup>18</sup> F]MA3, A CB <sub>2</sub> RECEPTOR AGONIST RADIOTRACER FOR POSITRON EMISSION TOMOGRAPHY .....	57
<b>CHAPTER-IV</b> .....	<b>79</b>
SYNTHESIS AND PRECLINICAL EVALUATION OF [ <sup>11</sup> C]BA-1 A PET TRACER FOR <i>IN VIVO</i> IMAGING OF CSF-1 RECEPTORS .....	79
<b>CHAPTER-V</b> .....	<b>99</b>
SYNTHESIS AND PRECLINICAL EVALUATION OF [ <sup>11</sup> C]G1055611 A NOVEL GPR84 PET LIGAND FOR VISUALISATION OF NEUROINFLAMMATION .....	99
<b>CHAPTER-VI</b> .....	<b>123</b>
GENERAL DISCUSSION AND FUTURE PERSPECTIVES .....	123
<b>SUMMARY</b> .....	<b>133</b>
<b>SAMENVATTING</b> .....	<b>136</b>
<b>CURRICULUM VITAE</b> .....	<b>139</b>
<b>SCIENTIFIC ACKNOWLEDGEMENT AND CONFLICT OF INTEREST</b> .....	<b>141</b>
<b>REFERENCES</b> .....	<b>143</b>



## LIST OF ABBREVIATIONS

% ID	% of injected dose
2-AEA	2-arachidonylethanolamide
2-AG	2-arachidonoylglycerol
3D	Three-dimensional
3D-MAP	3D maximum a posteriori
A <sub>1</sub> R	Adenosine-1 receptor
A <sub>2A</sub> R	Adenosine-2A receptor
AA	Arachidonic acid
AAV	Adeno-associated viral vector
ABC	ATP-binding cassette
ACTB	β-actin
AD	Alzheimer's disease
ALS	Amyotrophic lateral sclerosis
AMPA	α-amino-3-hydroxy-5-methyl-4-isoxazolepropionic acid
ATP	Adenosine triphosphate
BBB	Blood-brain barrier
BCRP	Breast cancer resistance protein
B <sub>max</sub>	Target protein expression
BP <sub>ND</sub>	Binding potential (Non Displaceable)
CB1R	Cannabinoid type-1 receptor
CB2R	Cannabinoid type-2 receptor
CNS	Central nervous system
COX	Cyclooxygenases
CSF-1	Colony stimulating factor-1
CSF-1R	Colony stimulating factor-1 receptor
CT	Computed tomography
C <sub>t</sub>	Cycle threshold
DAMP	Damage-associated molecular patterns
DCM	Dichloromethane
DIPEA	N,N-Diisopropylethylamine
DLU mm <sup>-2</sup>	Digital light units per square millimetre
DMF	Dimethylformamide
DMSO	Dimethyl sulfoxide
EAE	Experimental autoimmune encephalomyelitis
EC <sub>50</sub>	Half-maximal effective concentration
ECS	Endocannabinoid system
eGFP	Enhanced green fluorescent protein
FAAH	Fatty acid amide hydrolase
FFA	Free fatty acid
GAPDH	Glyceraldehyde 3-phosphate dehydrogenase
GMP	Good manufacturing practices

GPCR	G-protein coupled receptor (GPCR)
GPR84	G-protein coupled receptor84
HABs	High-affinity binders
HEK 293	Human embryonic kidney cells 293
HPLC	High-performance liquid chromatography
HSC	Haematopoietic stem cells
<i>i.m.</i>	Intramuscular
<i>i.p.</i>	Intraperitoneal
<i>i.v.</i>	Intravenous
IC <sub>50</sub>	50% inhibitory concentration
IL-10	Interleukin 10
IL-1 $\beta$	Interleukin 1 $\beta$
IL-34	Interleukin 34
IL-4	Interleukin 4
K <sub>d</sub>	Dissociation constant
KO	Knock-out
KTP	Ketoprofen
LABs	Low-affinity binders
LAL	Limulus amoebocyte lysate
LC-MS	Liquid Chromatography-Mass Spectrometry
logD	Distribution coefficient at pH 7.4
LPA	Lysophosphatidic acid
LPS	Lipopolysaccharide
MABs	Mixed intermediate- affinity binders
MAGL	Monoacylglycerol lipase
MAO	Monoamine Oxidase
MCFAs	Medium chain fatty acids
MDR1a/1b	Multidrug resistance-associated proteins
MMPs	Matrix metalloproteinases
mRNA	Messenger RNA
MS	Multiple sclerosis
NAWM	Normal-appearing white matter
NMR	Nuclear magnetic resonance
NO	Nitric oxide
NSAID	Nonsteroidal anti-inflammatory drug
<i>p.i.</i>	Post tracer injection
P1 receptor	Adenosine receptors
PAMP	Pathogen-associated molecular patterns
PBS	Phosphate-buffered saline
PD	Parkinson's disease
PET	Positron emission tomography
PGE2	Prostaglandin E2
P-gp	Permeability-glycoprotein
PRRs	Pattern recognition receptors

PSA	Polar surface area
QA	Quinolinic acid
RA	Rheumatoid arthritis
RNA	Ribonucleic acid
ROS	Reactive oxygen species
RP-HPLC	Reversed phase high-performance liquid chromatography
RT-qPCR	Real-time quantitative polymerase chain reaction
SCIDY	Spirocyclic iodonium ylide
SCL	Solute carrier
SD	Standard deviation
SNP	Single nucleotide polymorphism
SPMS	Secondary progressive multiple sclerosis
SRTM	Simplified reference tissue model
SUV	Standardised uptake value
TAC	Time activity curve
TAM	Tumour associated macrophage
TFA	Trifluoroacetic acid
TGF-1 $\beta$	Transforming growth factor 1 $\beta$
TLC	Thin layer chromatography
TMS	Tetramethylsilane
TNF- $\alpha$	Tumour necrosis factor- $\alpha$
TSPO	Tryptophan rich-sensory protein oxygen, 18 kDa translocator protein
UPLC	Ultra-High Performance Liquid Chromatography
UV	Ultra Violet
VOI	Volume of interest
VT	Distribution volume



# **CHAPTER-I**

## **GENERAL INTRODUCTION**





## **1. Neuroinflammation**

Inflammation is a highly dynamic and multifaceted process combining local and systemic reactions of various cell types, chemical signals and signalling pathways [1]. The fundamental purpose of inflammation is restoring the tissue homeostasis after injury or infection [1,2]. Inflammation contributes to tissue repair and regeneration (e.g. wound healing, scar formation, and suppression of infection); however, prolonged inflammation causes detrimental effects (e.g. allergy, chronic infections, and neurodegeneration) [1].

The term inflammation refers to a multicellular process characterised by changes in local vascular effects, activation of resident immune cells, infiltration of mobile immune cells and cytokine production [3]. Neuroinflammation is the inflammatory response within the Central Nervous System (CNS), often observed in diseases including stroke, multiple sclerosis (MS), Alzheimer's disease (AD), Parkinson's disease (PD), neurotrophic viral infections, neoplasias, traumatic brain injuries, bacterial and fungal infections [1]. In these brain pathologies, immune activation is triggered and contributes on one hand to "collateral" tissue damage with loss of neurons, and on the other hand to neuroregeneration and tissue repair [4]. Some authors suggested replacing the term neuroinflammation by "microglial activation" or CNS pseudo inflammation as microglia are the resident macrophages of the brain [3].

Microglial cells are the resident tissue mononuclear phagocytes of myeloid lineage, originating from erythromyeloid progenitors formed in the yolk sac, which makes them different from all other CNS macrophages formed in bone marrow [5,6]. In resting conditions, microglia display a ramified morphology and perform a surveying activity. In this state, they have been widely referred to as resting or quiescent microglia [7]. The activation of microglia is a unique adaptation reaction of the brain innate immune system, occurring in pathological conditions after injury or infection [2]. In the incident of brain damage, microglia rapidly migrate to the

site of injury, using the directional guidance provided by chemotactic mediators. During this condition, neurotransmitters, lipids, neurohormones, cytokines and/or chemokines bind to surface receptors switching the function of microglia [8]. The pattern recognition receptors (PRRs) that are expressed on the microglial surface can sense either damage-associated or pathogen-associated molecular patterns (DAMPs and PAMPs) [8].

Depending on the signalling molecules, microglia activation can be associated with the pro- or anti-inflammatory phenotypes. The classically activated or pro-inflammatory phenotype microglia can release pro-inflammatory mediators such as reactive oxygen species (ROS), nitric oxide (NO), interleukin 1 $\beta$  (IL-1 $\beta$ ) and tumour necrosis factor- $\alpha$  (TNF-  $\alpha$ ) [8]. On the other hand, the alternatively activated or anti-inflammatory phenotype of microglia release anti-inflammatory molecules like interleukin-4 and 10 (IL-4 and IL-10), transforming growth factor 1 $\beta$  (TGF-1 $\beta$ ), and arginases [8]. These two microglial states are named M1 (pro-inflammatory) and M2 (anti-inflammatory) microglial phenotypes (Figure 1). This working hypothesis is now considered as over-simplified as microglia can adapt a spectrum of functional phenotypes which can be dynamically switched [9,10].

During activation, microglia undergo functional and morphological changes and modulation of expression of several receptors, enzymes, and ion channels [7]. Hence, it is highly relevant to quantify activation-specific biomarkers non-invasively for diagnosis and follow up the progression of disease after therapy. The ideal functional imaging method to quantify the activated microglial non-invasively is positron emission tomography (PET) imaging. PET is a technique with high sensitivity that enables dynamic regional quantification of minute quantities of targeted selective radioactive probes. PET can thus visualise biological changes of various disorders at the molecular level, which typically occur before anatomical changes.

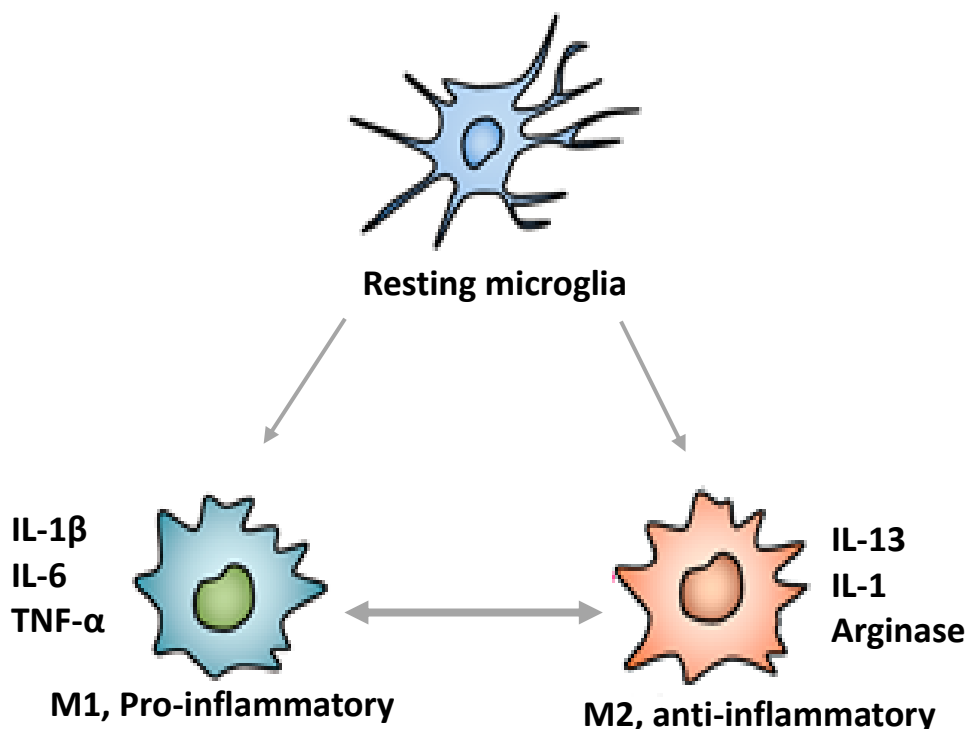


Figure 1: Schematic representation of microglial activation and surface markers expressed on M1 and M2 microglial phenotypes. *INF- $\gamma$*  and *LPS* induce M1 phenotypes, which express pro-inflammatory markers such as *IL-1 $\beta$* , *IL-6* and *TNF- $\alpha$* . *IL-4* and *IL-10* induce M2 phenotypes, which express anti-inflammatory makers such as *IL-13*, *IL-1* and *arginase*.

## 2. PET imaging

PET is an important technique for non-invasive imaging/assessment of biological processes by targeting disease-specific biomarkers. PET is a nuclear imaging technique, whereby a chemical compound with high affinity and selectivity for enzymes/receptors, transporters and misfolded proteins that have altered expression during the pathological process, is labelled with a positron emitting radionuclide like e.g. carbon-11 ( $^{11}\text{C}$ ,  $t_{1/2}=20.4$  min) or fluorine-18 ( $^{18}\text{F}$ ,  $t_{1/2}=109.8$  min) (Table 1). These radionuclides are produced by bombarding stable nuclei with protons accelerated to high energies by a cyclotron. However, some radionuclides are produced from generators, e.g. gallium-68 ( $^{68}\text{Ga}$ ,  $t_{1/2}=68$  min), germanium-68-/gallium-68 generator. The radionuclides are unstable due to the excess of protons and decay by conversion of a proton to a neutron and emission of a positron, the antiparticle of the electron. The positron travels a short

distance and combines with an electron to form positronium, the mass of which is converted into energy, i.e. two gamma rays of 511 keV that travel in opposite directions and penetrate biological tissues (Figure 2). The gamma rays are simultaneously detected by coincidence detectors in a PET camera, and the detection events are converted to three dimensional (3D) images representing the quantitative spatial distribution of radiotracer [11].

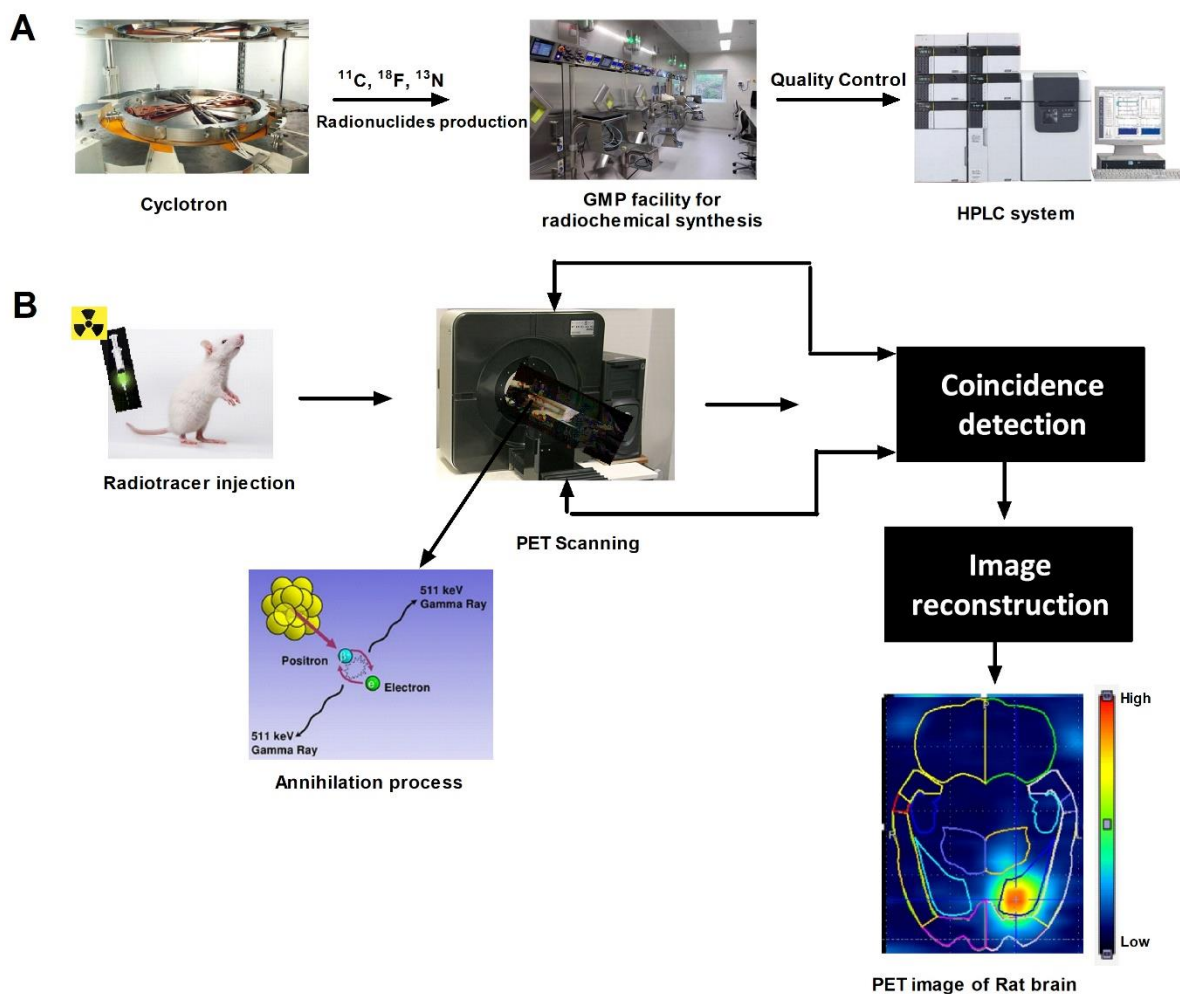


Figure 2: Schematic drawing of radiotracer synthesis and positron emission tomography (PET) imaging. A. Cyclotron produced radionuclides are incorporated into small organic molecules in the good manufacturing practice (GMP) compliant facility (for clinical application), where radiotracer synthesis, purification and sterile formulation preparation is performed. B. Subject under investigation is injected with a radiolabelled tracer, which has a high affinity for the receptors or enzymes of interest. The subject is scanned in a positron emission tomography scanner, millions of coincidence detections are converted to an image showing a quantitative spatial distribution of the radiotracer.

The most commonly used PET radionuclides are shown in Table 1. The radionuclides nitrogen-13 ( $^{13}\text{N}$ ) and oxygen-15 ( $^{15}\text{O}$ ), due to their very short half-lives are available only in chemical forms in which they are produced in the cyclotron target (e.g.  $^{13}\text{N}$ -ammonia) or require instant high yield reactions (e.g.  $^{15}\text{O}$ -water). Iodine-124 ( $^{124}\text{I}$ ), copper-64 ( $^{64}\text{Cu}$ ) and zirconium-89 ( $^{89}\text{Zr}$ ) are longer lived radionuclides that can be used to label biomolecules with slow plasma clearance (e.g. antibodies).  $^{68}\text{Ga}$  is an increasingly used PET isotope due to availability from a  $^{68}\text{Ge}/^{68}\text{Ga}$  generator and does not require an on-site cyclotron [12]. For the research presented in this thesis, we used  $^{11}\text{C}$  and  $^{18}\text{F}$ . These radionuclides are produced in a cyclotron by proton irradiation of nitrogen-14 [ $^{14}\text{N}$  (p,  $\alpha$ )  $^{11}\text{C}$ ] or oxygen-18 [ $^{18}\text{O}$  (p,n)  $^{18}\text{F}$ ] respectively.  $^{11}\text{C}$  decays to boron-11 ( $^{11}\text{B}$ ) by positron emission, has a half-life of 20.4 min.  $^{18}\text{F}$  decays to  $^{18}\text{O}$  by positron emission and has a half-life of 109.8 min. The shorter half-life of  $^{11}\text{C}$  is associated with a lower radiation dose and thus allows to perform multiple scans (that can even be acquired within one day) in the same subject and is frequently used in drug occupancy studies [13]. However, an onsite cyclotron is required for studies with  $^{11}\text{C}$  and fast and efficient incorporation of  $^{11}\text{C}$  into the target molecule is required.

The half-life of  $^{18}\text{F}$  is long enough to perform multi-step radiochemical reactions, and transportation to remote PET centres that have no cyclotron is possible.

Radionuclides obtained in a cyclotron or from a generator, are transferred to lead shielded hot-cells where the radionuclides are incorporated into precursor molecules using automated synthesis modules. After the radiochemical reaction, the crude reaction mixture is usually purified using preparative high-performance liquid chromatography (HPLC). Subsequently, the purified radiotracers are collected and formulated and sterile filtered to allow intravenous (*i.v.*) injection into humans or animals. The radiochemical (radio-HPLC, radio-TLC), radionuclidic (gamma spectrometry), chemical (HPLC, TLC) and microbiological (LAL test, sterility test)

purity of the radiotracers is determined before or after (sterility test results take 14 days) human/ animal administration.

Table 1: Common radionuclides used in PET [14]

Radionuclide	Half-life	Mode of decay	$E_{\max}$ of $\beta^+$ (keV) max range in $H_2O$ (mm)	Chemistry
$^{11}C$	20.4 min	$\beta^+$ (100%)	960 keV 3.9 mm	Fast organic chemistry
$^{13}N$	9.97 min	$\beta^+$ (100%)	1198 keV 5.1 mm	Fast organic chemistry
$^{15}O$	2.03 min	$\beta^+$ (100%)	1732 keV 8.0 mm	Fast on-line gas phase chemistry
$^{18}F$	109.8 min	$\beta^+$ (97%) EC (3%)	634 keV 2.3 mm	Fast organic chemistry
$^{64}Cu$	12.7 h	$\beta^+$ (20%)	653 keV 2.4 mm	Chelation chemistry
$^{68}Ga$	68 min	$\beta^+$ (89%) EC (11%)	1899 keV 8.9 mm	Chelation chemistry
$^{89}Zr$	78.4 h	$\beta^+$ (23%) EC (77%)	897 keV 3.6 mm	Chelation chemistry
$^{124}I$	4.17 d	$\beta^+$ (23%) EC (77%)	1535 keV(50%) 6.9 mm 2138 keV (50%) 10.2 mm	Organic chemistry

The ideal PET tracer should have a high affinity for the target of interest and should have an equilibrium dissociation constant ( $K_d$ ) value in subnanomolar to low nanomolar range. The affinity of the developed tracer should be at least 5-10 times higher than the target protein expression ( $B_{\max}$ ). High selectivity for the target is also essential with an affinity preferably 100 times lower for any other binding site with the same expression level [14–16].

The blood-brain barrier (BBB) prevents hydrophilic and large molecules from entering the brain and is the foremost limitation in developing drugs that target the CNS. Favourable molecular characteristics for entering the brain by passive diffusion over the BBB are low molecular mass (< 500 Da), a polar surface area (PSA) less than 90 Å<sup>2</sup> and lack of formal charge at physiological pH and a distribution coefficient at pH 7.4 (logD) between 1 and 3. In addition, tracer uptake in the brain can be impeded when the tracer is a substrate for ATP-binding cassette (ABC) transporter family efflux pump (e.g. P-glycoprotein (P-gp)), multidrug resistance-associated proteins (MDR1a/1b), breast cancer resistance protein (BCRP) and solute carrier (SCL) family influx transporter [15]. Substrates for P-gp are highly lipophilic, carry a positive charge at physiological pH and have multiple aromatic rings [15,16]. Highly lipophilic molecules usually show high non-specific binding to lipophilic membranes and proteins [14]. Besides, their formulation for intravenous injection will be challenging due to adsorption of lipophilic drugs on the surface of vials, injection lines, filter membranes and syringes.

After crossing the BBB, the ideal PET tracer should show low non-specific binding in the target tissue, and high but reversible specific binding to the target allowing kinetic modelling and determination of binding potential. The PET scanner detects annihilation radiation and does not discriminate between the different chemical forms of the positron-emitting radionuclide. The presence of a radiometabolite in the brain can, therefore “contaminate” the specific parent tracer signal and preclude or hinder tracer quantification.

### **3. The current state of the art for Neuroinflammation with PET**

Traditionally neuroinflammation was studied non-invasively using TSPO PET tracers, currently several interesting biomarkers and specific PET tracers have been developed for imaging neuroinflammation such as MMP, MAO, COX, adenosine receptors, histamine receptors, P<sub>2</sub>X<sub>7</sub> receptors. It would be of real clinical interest to study different microglial activation states. This

would not be possible with a single target or tracer approach. Potentially studied targets and developed PET tracers for neuroinflammation were outlined here.

### ***3.1. Translocator protein***

Tryptophan rich-sensory protein of oxygen (TSPO, 18 kDa translocator protein) is an 18 kDa protein mainly found on the outer mitochondrial membrane in peripheral organs and the CNS. TSPO is involved in various cellular functions like cholesterol transport, steroid hormone synthesis, mitochondrial respiration, permeability transition pore opening, apoptosis and cell proliferation [17]. TSPO is the most widely studied neuroinflammation related PET target. The expression of TSPO is low in healthy brain tissue [18]. During disease conditions, TSPO expression is highly upregulated and has been recognised as a biomarker to study neuroinflammation [19,20]. As per a recent review, more than 80 radiotracers have been developed for TSPO [21]. The isoquinoline derivative (R)-[<sup>11</sup>C]PK11195 (Figure 3) is one of the first, widely studied TSPO PET tracers, although it has several limitations such as low brain uptake, high non-specific binding in brain and difficulties for accurate quantification of TSPO binding [22].

Single nucleotide polymorphism (rs6971) in the TSPO gene leads to the occurrence of three human genotypes (C/C, T/T and C/T) with different affinity states [23]. Second-generation TSPO tracers bind to these three human TSPO genotypes with high affinity (high affinity binders, HABs), low affinity (low affinity binders, LABs), or mixed (intermediate, MABs) affinity. Hence genetic information from patients is required for correct TSPO quantification [24]. Differences in affinity between high affinity binders and low affinity binders were approximately 50-fold with PBR28, 17-fold with PBR06 and 4-fold with DAA1106, DPA713 and PBR111 [25,26]. A recent study conducted with [<sup>18</sup>F]DPA714 reported a distribution



volume (VT) of  $47.6 \pm 6.3\%$  higher in HABs compared to MABs [22]. (R)- $^{[11C]}$ PK11195 does not differentiate HABs and LABs due to low specific binding in the brain [27].

$^{[18F]}$ DPA714 is one of the most widely used 2<sup>nd</sup> generation TSPO PET tracers.  $^{[18F]}$ DPA714 biodistribution in mice showed the highest uptake in lungs, heart, kidney, spleen and liver. Pre-treatment with non-radioactive DPA714 or (R)-PK11195 blocked 80% uptake in lungs and heart [28]. No radiometabolites were observed in plasma, brain, lungs, spleen, heart at 60 min p.i. [28]. An *in vivo* radiometabolite study performed in rats and baboons confirmed a parent fraction of 15 and 11% respectively in plasma at 120 min post injection (p.i.). These results suggest a high variability in metabolism between mice and other species [29].  $^{[18F]}$ DPA714 is hypothesised to undergo O-dealkylation that leads to the formation of  $^{[18F]}$ fluoroacetaldehyde or its oxidative product  $^{[18F]}$ fluoroacetic acid.  $^{[18F]}$ fluoroacetaldehyde is known to cross BBB thus contaminate the brain PET signal.  $^{[18F]}$ fluoroacetic acid may convert into  $^{[18F]}$ fluoride which tend to bind to bone including skull [30,31]. Due to these reasons, structural modifications of DPA714 were explored to prevent O-dealkylation. Four fluoroalkynyl derivatives of DPA714 were synthesised, of which DPA-C5yne has the highest affinity (0.35 nM) towards TSPO whereas DPA714 has an affinity of 0.91 nM in the same assay [32]. *In vitro* metabolite evaluation by incubation with rat microsomes showed four different metabolites but absence of defluorination for all the four derivatives [32,33].

$^{[18F]}$ GE-180 emerged as a 3<sup>rd</sup> generation TSPO PET tracer for quantification of TSPO. In a recent head-to-head comparison between  $^{[18F]}$ GE-180 and the 2<sup>nd</sup> generation TSPO PET tracer  $^{[11C]}$ PBR28,  $^{[18F]}$ GE-180 showed a 20 times lower VT and relatively difficult kinetic modelling. Hence the authors concluded that  $^{[18F]}$ GE-180 has unfavourable characteristics for TSPO imaging in the human brain compared to  $^{[11C]}$ PBR28 [34].

## Chapter-I

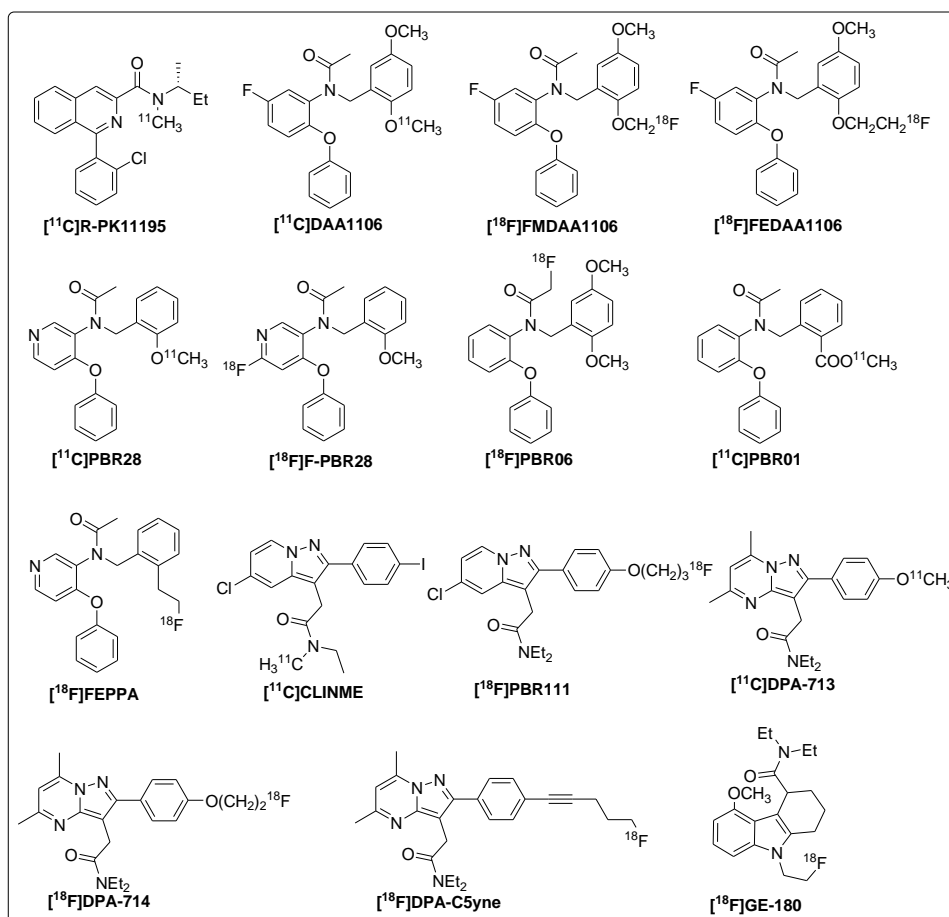


Figure 3: Structures of TSPO PET tracers

### 3.2. Matrix metalloproteinases

Matrix metalloproteinases (MMPs) are extracellular enzymes they are synthesised in the rough endoplasmic reticulum. MMPs are involved in turnover and degradation of extracellular matrix and are known to participate in tissue repair by promoting angiogenesis and neurogenesis. During vascular cognitive impairments, MMPs change the permeability of BBB that might cause white matter damage. MMPs have been involved in the formation and degradation of amyloid proteins in AD [35] and also apoptosis of dopaminergic neurons in PD [36]. Among the MMPs gelatinases, MMP2 and MMP9 are of specific interest due to their involvement in angiogenesis, cancer cell proliferation and metastasis and atherosclerosis [37].

Several PET radiotracers with subnanomolar affinities to various MMPs have been developed; however, none of the developed tracers displayed promising preclinical results [14]. Selivanova *et al.* synthesised a series of sulfonamidopropanoic acid derivatives. Among them, compound 7 was found to have a high affinity for MMP-2 ( $IC_{50}$  1.8 nM) and MMP-9 ( $IC_{50}$  7 nM), and carries an aromatic fluorine atom which was substituted by fluorine-18. [ $^{18}F$ ]7 (Figure 4), showed good *in vitro* metabolic stability in mouse and human plasma as no decomposition was observed up to 2h incubation at 37 °C. Preliminary PET/CT studies with [ $^{18}F$ ]7 showed lack of brain penetration [37] this might be due to the carboxylic acid group which results in a formal negative charge at physiological pH, a low clogD (<1) and high cPSA (127 Å<sup>2</sup>). Hugenberg *et al.* introduced heteroaromatic ring triazole derivatives as MMP inhibitors, which provide potential additional hydrogen bond acceptors and increases binding potencies of the inhibitors to enzymes at the active site of MMPs. Compound 12a is less selective but has high affinity towards MMP-2, 8, 9 and 12. Further radiolabelling 12a was carried out yielding [ $^{18}F$ ]12a (Figure 4) that showed good serum stability and rapid plasma clearance. However, PET study showed that [ $^{18}F$ ]12a also did not enter the brain [38], (clogD of 1.25 and cPSA of 126.6 Å<sup>2</sup>) the structural characteristics and the presence of sulphonamide group may be the possible reasons.

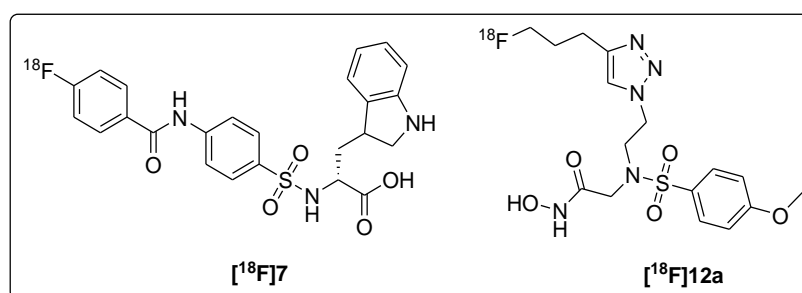


Figure 4: Structures of MMP PET tracers

### 3.3. Monoamine Oxidase

Monoamine Oxidase (MAO) exists as two isoforms namely MAO-A and MAO-B and is an outer mitochondrial membrane enzyme present in the brain and most of the peripheral organs where it primarily catalyses the oxidation of monoamines. MAO-A catalyses serotonin, norepinephrine and tyramine oxidation whereas MAO-B catalyses dopamine, trace amine and phenylethylamine oxidation [39]. MAO-B is mainly expressed on astrocytes and found to play a role in neurodegeneration by disrupting oxidative homeostasis [21].

In a recent review, Fowler *et al.* classified MAO radiotracers into irreversibly trapped radiotracers including suicidal inhibitors and reversibly binding tracers [39]. MAO-A radiotracers [<sup>11</sup>C]clorgyline, [<sup>11</sup>C]harmine, and [<sup>11</sup>C]befloxatone are MAO-A PET-tracers that have been used clinically [39]. L-deprenyl inhibits MAO-B, and MAO-catalysed oxidation of deprenyl showed strong deuterium isotope effect. Rodriguez-Vieitez *et al.* demonstrated that astrocytosis precedes A $\beta$  deposition, by performing a dual tracer study with [<sup>11</sup>C]deuterium-L-deprenyl ([<sup>11</sup>C]DED for astroglial MAO-B) and [<sup>11</sup>C]AZD2184 for beta-amyloid [40]. Further, carbon-11 labelled L-deprenyl and its deuterium analogue [<sup>11</sup>C]deuterium-L-deprenyl (Figure 5) was used in PD, focal epilepsy, amyotrophic lateral sclerosis (ALS) and AD patients to quantify MAO-B [14]. Nag *et al.* developed [<sup>18</sup>F]Fluororasagiline as a specific MAO-B tracer with 84-fold selectivity over MAO-A. *In vitro* autoradiography studies with the post-mortem human brain sections confirmed selective binding of [<sup>18</sup>F]Fluororasagiline to MAO-B. PET studies in a cynomolgus monkey with [<sup>18</sup>F]Fluororasagiline showed high brain uptake in MAO-B rich regions, but time-activity curves showed an increase in radioactivity accumulation over time that was attributed to brain penetrable radiometabolites [41]. For an improved metabolic stability of rasagiline, the same group has developed a deuterated analogue [<sup>18</sup>F]fluororasagiline-D2. A PET study in a cynomolgus monkey showed similar brain uptake

and better stability in monkey plasma with 40% of the fraction of radiometabolites of the non-deuterated analogue [42].

Later the same group developed two  $^{18}\text{F}$  labelled propargyl amines [ $^{18}\text{F}$ ]16 and [ $^{18}\text{F}$ ]18 (Figure 5). *In vitro* autoradiography studies performed on post-mortem brains showed high non-specific binding of [ $^{18}\text{F}$ ]16, hence further evaluation was not carried out. [ $^{18}\text{F}$ ]18 was evaluated further in a cynomolgus monkey PET study, where it showed high brain uptake and irreversible binding. In plasma radiometabolite analysis only 12% parent tracer was found 120 min p.i.. Similar to [ $^{18}\text{F}$ ]Fluororasagiline, according to authors [ $^{18}\text{F}$ ]18 time-activity curves suggested an accumulation of radiometabolites into the brain [43]. Later the selective and reversible MAO-B tracer [ $^{11}\text{C}$ ]SL25.1188 (Figure 5) was evaluated in healthy human volunteers [44]. This study confirmed high brain uptake and good metabolic stability in humans but showed slow kinetics. Therefore, an [ $^{18}\text{F}$ ]fluoropropoxy derivative [ $^{18}\text{F}$ ]SL25.1188 was developed and evaluated further (Figure 5).

[ $^{18}\text{F}$ ]SL25.1188 showed high initial brain uptake and rapid washout, but unfortunately, a lack of MAO-B specific binding was observed in blocking experiments with L-deprenyl. Further evaluation of other derivatives of SL25.1188 is currently ongoing [45].

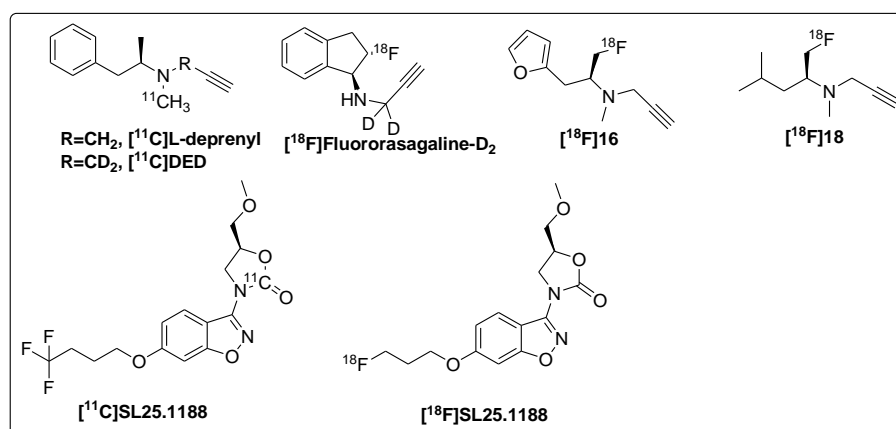


Figure 5: Structures of MAO PET tracers

### 3.4. Cyclooxygenases

Cyclooxygenases (COX) are the enzymes involved in the biosynthesis of prostanoids. Two isoforms namely COX-1 and COX-2 are well known and a 3<sup>rd</sup> isoform COX-3 or COX-1b was also described in the literature, but its physiological function remains yet unknown [46,47]. COX-1 is constitutively expressed in most tissues. Whereas under basal conditions COX-2 expression is low, but it is upregulated during inflammation. The expression of COX-2 is elevated in the brain during neuroinflammation, and its expression is mainly located in activated microglia and astrocytes [14]. Upregulation of COX-1 and COX-2 has been reported in patients with neurodegenerative disorders such as AD, PD and ALS [48–50].

Ketoprofen (KTP) is a commercially available nonsteroidal anti-inflammatory drug (NSAID) and is a selective COX-1 inhibitor. The limitation of KTP is its low brain penetration due to the presence of a carboxylic acid group. To overcome this limitation, Takashima-Hirano *et al.* developed a methyl ester derivative [<sup>11</sup>C]KTP-Me (Figure 6) that was shown to enter the rat brain after lipopolysaccharide (LPS) induced inflammation. The specificity was proved by a blocking study [51]. Metabolite analysis in rat brain confirmed [<sup>11</sup>C]KTP-Me enters the brain and later hydrolysed to [<sup>11</sup>C]KTP [51]. *Ex-vivo* autoradiography studies found a significant reduction of [<sup>11</sup>C]KTP-Me in COX-1 KO mice but not in COX-2 KO mice. PET imaging performed on rats after intrastriatal injections of LPS and quinolinic acid (QA) showed a significant increase of [<sup>11</sup>C]KTP-Me accumulation [52]. Other tracers for COX-2 are [<sup>18</sup>F]celecoxib (Figure 6) that showed rapid defluorination in rats and monkey [53] and [<sup>11</sup>C]rofecoxib (Figure 6) that did not show any increase in tracer uptake in two of the studied rat models of neuroinflammation [54]. The authors suggested that low-affinity of celecoxib (0.04-0.9 μM) and rofecoxib (0.02-0.5 μM) could be the reason behind their failure to image COX-2 expression with PET. Still, there is high demand to develop specific COX-2 PET tracers with increased affinities [55].

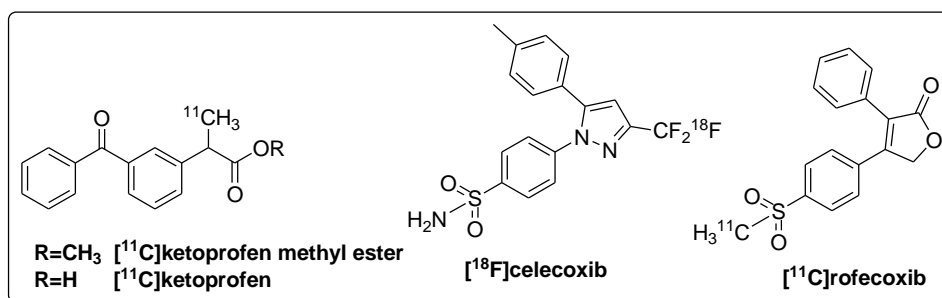


Figure 6: Structures of COX PET tracers

### 3.5. Adenosine receptors

Adenosine receptors (P1 receptors) belong to the purinergic G-protein coupled receptors family. The endogenous ligand for these receptors is adenosine [56]. In humans, four types of adenosine receptors exist namely  $A_1$ ,  $A_{2A}$ ,  $A_{2B}$ , and  $A_3$ .  $A_1$  receptors ( $A_1R$ ) are involved in microglia responses, whereas  $A_{2A}$  have anti-inflammatory and immunological functions as well and they were suggested to play a critical role in the pathophysiology of neurodegeneration [57,58].

Ishiwata *et al.* developed three  $^{11}\text{C}$  labelled adenosine  $A_1$  receptors tracers. Based on their biological evaluation in mice, rats and cats [59–61]  $[^{11}\text{C}]$ MPDX (Figure 7) was selected for further evaluation in humans to map the adenosine  $A_1R$  density [62]. Paul *et al.* evaluated  $[^{11}\text{C}]$ MPDX in a rodent model of encephalitis and concluded that the observed  $A_1R$ s upregulation during the early phase of encephalitis might involve a neuroprotective role for  $A_1R$ s [63].  $[^{18}\text{F}]$ CPFPX (Figure 7), a fluorine-18 derivative of  $[^{11}\text{C}]$ MPDX that was evaluated in healthy rats using a simplified reference tissue model (SRTM) for quantification of  $A_1R$ s with the olfactory bulb as a reference region [64]. Previously,  $[^{18}\text{F}]$ CPFPX was evaluated in healthy volunteers using arterial input function for quantification, which is an invasive procedure [65].

Naganawa *et al.* developed  $[^{11}\text{C}]$ TMSX (Figure 7) an  $A_{2A}$  antagonist it was evaluated in healthy volunteers. They determined the binding potential ( $\text{BP}_{\text{ND}}$ ) value using cerebral cortex and

centrum semiovale as a reference region [66], however blocking studies are still needed for further validation of this tracer. Rissanen *et al.* performed a study with [ $^{11}\text{C}$ ]TMSX in eight patients with secondary progressive multiple sclerosis (SPMS) and seven healthy controls and found significantly increased  $A_{2A}$ Rs in SPMS patients when compared with healthy controls (VT  $0.55\pm 0.08$  vs  $0.45\pm 0.05$ ) [67]. Moresco *et al.* synthesised several derivatives of SCH442416, which is non-xanthine  $A_{2A}$  antagonist to overcome the limitations of xanthine-based molecules, such as photoisomerisation and low signal-to-background ratio. [ $^{11}\text{C}$ ]SCH442416 displayed a high uptake in the striatum (rich in  $A_{2A}$  receptors) in rats and monkeys [68]. Later, Khanapur *et al.* synthesised and evaluated two fluorine-18 labelled analogues of SCH442416 ([ $^{18}\text{F}$ ]10a and [ $^{18}\text{F}$ ]10b, Figure 7). Both tracers showed displaceable binding in the striatum, and metabolic stability similar to [ $^{11}\text{C}$ ]SCH442416 [69]. Zhou *et al.* synthesised [ $^{11}\text{C}$ ]preladenant (Figure 7), this tracer displayed specific binding in the areas with a high  $A_{2A}$ R expression such as striatum [70]. Same group evaluated [ $^{11}\text{C}$ ]preladenant in conscious monkey and healthy human volunteers [71,72]. Later, Barret *et al.* developed a fluorinated analogue of Preladenant ([ $^{18}\text{F}$ ]MNI-444) that was evaluated in non-human primates [73]. Regional brain uptake was consistent with  $A_{2A}$ R brain distribution and dose dependent blocking with tozadenant and preladenant proved  $A_{2A}$ R specificity [73].

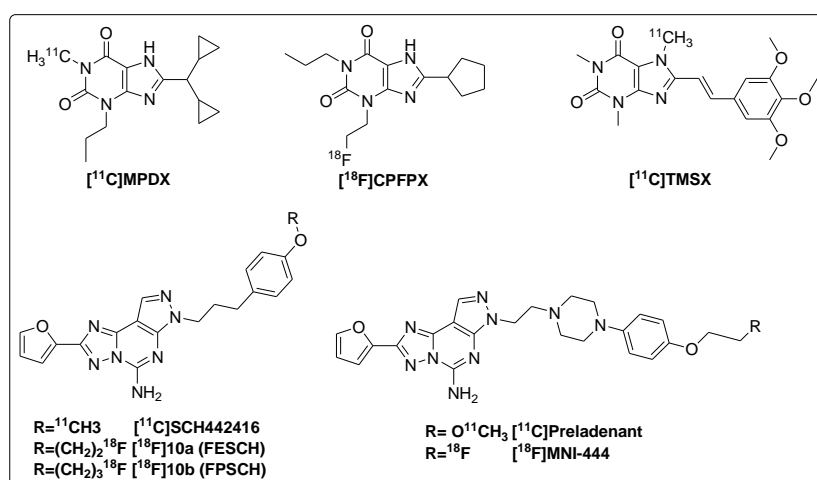


Figure 7: Structures of  $A_{2A}$ R PET tracers



### 3.6. Histamine H<sub>4</sub> receptors

Histamine receptors are the G-protein coupled receptors with histamine as their endogenous ligand. H<sub>1</sub>, H<sub>2</sub>, H<sub>3</sub> and H<sub>4</sub> are the four subtypes of histamine receptors present in the human body, of which H<sub>3</sub> and H<sub>4</sub> are expressed in brain [74]. Upregulation of H<sub>4</sub>R expression on microglia is detected during neuroinflammation [75]. Only two H<sub>4</sub>R PET ligands ([<sup>11</sup>C]JNJ7777120 and [<sup>11</sup>C]VUF10558) have been developed so far [76] (Figure 8).

[<sup>11</sup>C]VUF10558 did not show any brain uptake, but [<sup>11</sup>C]JNJ7777120 did prove brain entry. A recent study demonstrated that JNJ7777120 treatment in experimental autoimmune encephalomyelitis (EAE) mice normalised the clinical and neuropathological signs of the disease [75,76].

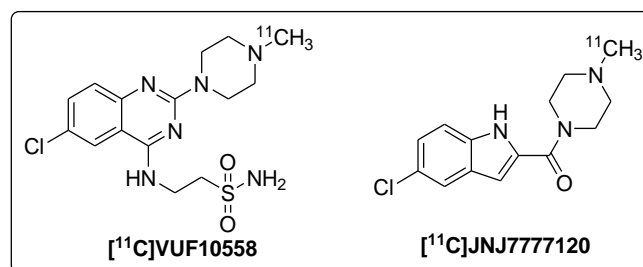


Figure 8: Structures of H<sub>4</sub> PET tracers

### 3.7. P2X<sub>7</sub> receptors

P2X<sub>7</sub>R is a purinergic receptor subtype [77] with adenosine triphosphate (ATP) as its endogenous ligand, activating P2X<sub>7</sub> with a low affinity (mM) [78]. The extracellular concentrations of ATP are strictly regulated in physiological conditions during which P2X<sub>7</sub>R is not activated, and is present as a ‘silent receptor’. Whereas in pathological conditions that involve an increase in ATP concentrations, the P2X<sub>7</sub>R is functionally upregulated. Interestingly, P2X<sub>7</sub>R activation results in a further release of ATP and causes signal amplification [77]. P2X<sub>7</sub>R expression was observed on microglia, astrocytes, oligodendrocytes,

neuronal progenitor cells and mature neurons [79]. It was reported that P2X<sub>7</sub>R mRNA levels in the hippocampus drop by 80 % when microglia are depleted [80]. P2X<sub>7</sub>R has, therefore, gained interest as a therapeutic target for neurodegeneration, neuropsychiatric disorders and chronic pain [81,82].

Janssen *et al.* have evaluated [<sup>11</sup>C]A-740003 (antagonist, IC<sub>50</sub> hP2X<sub>7</sub>R 40 nM) (Figure 9) as a radiotracer for P2X<sub>7</sub>R. Rat studies, however, showed low brain uptake [83]. Ory *et al.* have developed a high-affinity ligand [<sup>11</sup>C]JNJ54173717 (IC<sub>50</sub> hP2X<sub>7</sub>R 4 nM) as P2X<sub>7</sub>R antagonist PET tracer. It showed good brain uptake in rat and non-human primates and blocking studies performed on non-human primates confirmed the [<sup>11</sup>C]JNJ54173717 is a P2X<sub>7</sub>R-specific tracer. This tracer was further evaluated in a rat model with locally overexpressed human P2X<sub>7</sub>R receptors using adeno-associated viral vector (AAV) technology [84]. Currently, [<sup>11</sup>C]JNJ54173717 is being evaluated clinically in patients with neurodegenerative diseases [85]. Very recently, Bhattacharya reported that JNJ54175446 displaced [<sup>18</sup>F]JNJ64413739 (antagonist) in healthy human subjects in a dose-dependent manner [86]. In another study, [<sup>11</sup>C]SMW139 (antagonist, IC<sub>50</sub> hP2X<sub>7</sub>R 32 nM) showed good brain exposure in a rat model with locally AAV induced overexpressed human P2X<sub>7</sub>R receptors. However, the study reported an absence of P2X<sub>7</sub>R receptor upregulation in [<sup>11</sup>C]SMW139 autoradiography experiments performed on post-mortem brain sections from AD patients [87]. Gao *et al.* developed another promising tracer for P2X<sub>7</sub>R, [<sup>11</sup>C]GSK1482160 [88]. This ligand was further evaluated in LPS [89] and EAE models [90]. Biodistribution and microPET studies have confirmed increased brain uptake of [<sup>11</sup>C]GSK1482160 after LPS challenge. Furthermore, brain entry of [<sup>11</sup>C]GSK1482160 was confirmed in non-human primates [90]. Recently, Fantoni *et al.* published [<sup>18</sup>F]EFB, a tracer with high *in vitro* hP2X<sub>7</sub>R affinity. However, [<sup>18</sup>F]EFB low brain uptake as observed in healthy and LPS pre-treated rats precludes its application for *in vivo* brain P2X<sub>7</sub>R imaging [91].

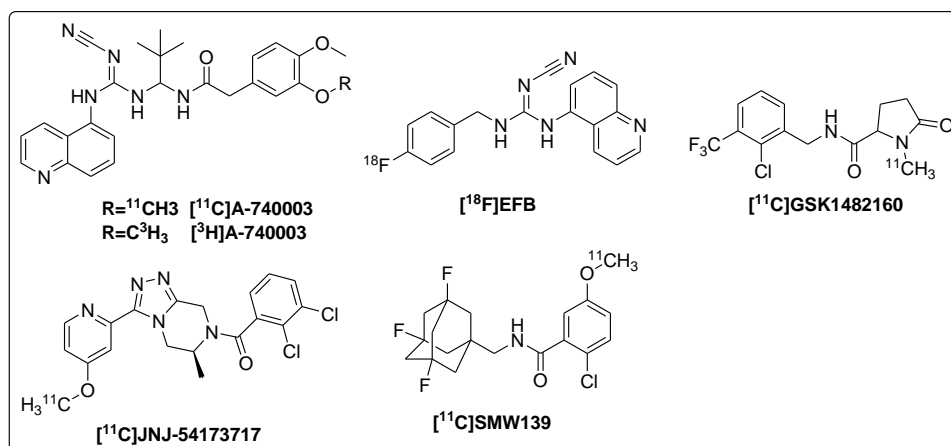


Figure 9: Structures of P2X<sub>7</sub>R PET tracers

### 3.8. Concluding remarks

Unfortunately, several PET tracers that have been discussed above failed due to low affinity or off-target binding or do not have sufficient BBB penetration. Until now, TSPO is the most widely studied target for visualisation of neuroinflammation with PET. However, studies with TSPO PET tracers were not successful in visualising neuroinflammation in AD patients [21]. This might be due to low signal-to-noise ratio and/or low expression of TSPO in AD. Furthermore, TSPO genetic polymorphism (rs6971) results in variable binding affinities of TSPO PET tracers; hence TSPO expression quantification requires the genetic information of individual subjects. Lastly, TSPO is highly expressed in both microglia and astrocytes [92]. In microglia, TSPO expression is associated with both M1 and M2 phenotypes [93], thus may not be able to visualise pro or anti-inflammatory phenotype of microglia with TPSO PET tracers.

Several PET tracers were developed for MMPs; their low brain penetration, however limits their use for imaging neuroinflammation. MMP tracers should require structural modifications for better logD and PSA values to facilitate their passive brain entry. MAO-B PET studies with [11C]DED suggested that astrocytosis precedes amyloid deposition in AD. Many of the COX-2 PET tracers showed either low affinity or nonspecific binding therefore, a high-affinity tracer

is needed to allow COX-2 PET imaging of neuroinflammation. The A<sub>2A</sub>R tracer [<sup>11</sup>C]TMSX significantly showed increased uptake in MS patients compared to healthy control. However, [<sup>11</sup>C]TMSX suffers from low binding potential and high non-specific binding. Other A<sub>2A</sub>R tracers displayed more favourable characteristics for PET imaging, and further studies in animal models of neuroinflammation and patients are required. P2X<sub>7</sub>R is emerging as a potential target for imaging neuroinflammation. Currently, clinical studies with [<sup>11</sup>C]JNJ54173717 and [<sup>11</sup>C]SMW139 are ongoing with neuroinflammation patients [85].

The present thesis explored the development of novel PET tracers for biological targets that are (over) expressed in neuroinflammation and related pathologies including monoacylglycerol lipase (MAGL), Cannabinoid type 2 receptor (CB<sub>2</sub>R), colony stimulating factor-1 receptor (CSF-1R) and G-protein coupled receptor84 (GPR84).

#### **4. Targets studied in this thesis**

##### ***4.1. Endocannabinoid system***

The endocannabinoid system (ECS) is a neuro- and immunomodulatory system that comprises the cannabinoid type 1 (CB<sub>1</sub>) and cannabinoid type 2 (CB<sub>2</sub>) receptors. CB<sub>1</sub>R is chiefly expressed in the central nervous system and is responsible for the CNS effects of cannabis. Whereas CB<sub>2</sub>R is mainly expressed on organs and cells with immune functions such as spleen, tonsils and leucocytes. The cannabinoid system also includes the endogenous ligands 2-arachidonoylglycerol (2-AG) and 2-arachidonylethanolamide (2-AEA or anandamide). 2-AG is a full agonist for both cannabinoid receptors, whereas 2-AEA is in partial agonist for cannabinoid receptors with more selectivity to CB<sub>1</sub>R. These endogenous ligands are degraded by the enzymes monoacylglycerol lipase (MAGL) and fatty acid amide hydrolase (FAAH) respectively [94,95]. In addition to the above mentioned two classical cannabinoid receptors, the non-CB<sub>1</sub>/CB<sub>2</sub> receptors such as GPR18, GPR55 and GPR119 have been proposed to have

a function in endocannabinoid-mediated signalling pathways [95–97]. In the CNS, the endocannabinoid system plays a vital role in the regulation of several physiological functions such as cognition, pain, movement and memory [98,99]. The cannabinoid signal is rapidly terminated due to the breakdown of endocannabinoids by the enzymatic activity of the serine hydrolases, FAAH and MAGL [100].

#### 4.1.1. Monoacylglycerol lipase

Monoacylglycerol lipase (MAGL) is a 33-kDa cytosolic serine hydrolase enzyme that preferentially cleaves monoacylglycerols into fatty acids and glycerol and plays a crucial role in coordinating multiple lipid signalling pathways. In the brain, MAGL is co-localised with CB<sub>1</sub> receptors in axon terminals where it is responsible for approximately 85% of 2-AG hydrolysis [101,102]. Therefore, MAGL is an essential terminating factor of the endocannabinoid signalling activity. Because of its crucial role in several lipid signalling pathways, MAGL is known to be involved in many pathological conditions, such as (neuro)inflammation, cancer, neurodegenerative disorders and several psychological disorders such as anxiety and depression [103].

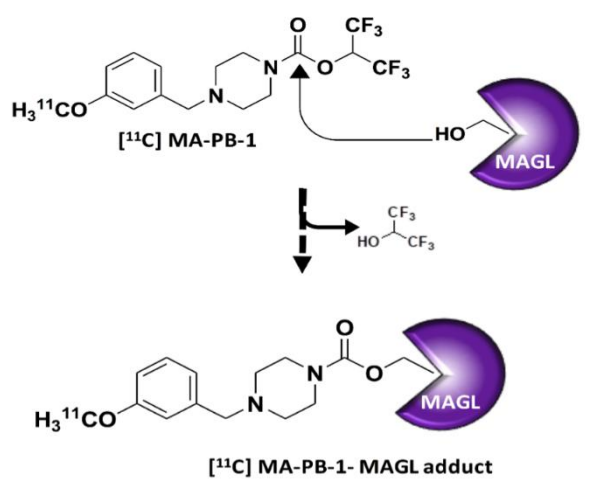


Figure 10: Proposed mechanism of MAGL binding by  $[^{11}\text{C}]$ MA-PB-1. The catalytic serine (Ser122) of MAGL attacks the activated carbamate of  $[^{11}\text{C}]$ MA-PB-1, releasing hexafluoroisopropanol and forming a covalent adduct [104].

The proposed mechanism of inactivation of MAGL by covalent binding of [ $^{11}\text{C}$ ]MA-PB-1 was depicted in Figure 10. Hicks and co-workers reported five PET radioligands for imaging of MAGL namely [ $^{11}\text{C}$ ]-KML29, [ $^{11}\text{C}$ ]-JW642, [ $^{11}\text{C}$ ]-ML-30 and [ $^{11}\text{C}$ ]-JJKK-0048 and a [ $^{11}\text{C}$ ]CH<sub>3</sub>-labeled 1,2,4-triazole urea compound [105]. The lack of MAGL-specific brain uptake led to the conclusion that none of the tracers was suitable for *in vivo* imaging of brain MAGL [105]. Later Wang *et al.* reported [ $^{11}\text{C}$ ]-SAR127303 as a MAGL specific tracer in rats [106]. A comparative study between [ $^{11}\text{C}$ ]-SAR127303 and [ $^{11}\text{C}$ ]-TZPU [107] by Wang *et al.* demonstrated that [ $^{11}\text{C}$ ]-TZPU did not show adequate brain penetration in contrast to [ $^{11}\text{C}$ ]-SAR127303. More recently, Cheng *et al.* explored  $^{11}\text{C}$ -labelled azetidincarboxylate derivatives for MAGL imaging. These new series of MAGL inhibitors are radiolabeled site specifically using [ $^{11}\text{C}$ ]-carbonylation and spirocyclic iodonium ylide (SCIDY) radiofluorination. The lead compound displayed irreversible specific binding *in vitro* and *in vivo* [108].

#### 4.1.2. Cannabinoid type 2 receptors

The CB<sub>2</sub> receptors are principally expressed on peripheral organs and organs with immune functions. The expression of brain CB<sub>1</sub>R was imaged using [ $^{18}\text{F}$ ]MK-9470 PET in monkey and humans [109]. In the brain, the CB<sub>2</sub>R expression is low under physiological conditions and is mainly detected in Purkinje cells of the cerebellum, hippocampal neurons and brain stem [110]. The expression of CB<sub>2</sub>R is upregulated during pathological conditions such as (neuro)inflammation and is predominantly observed in the activated microglia of the brain [111,112]. Of note, there are several contradictory or confusing reports found on CB<sub>2</sub> expression levels and locations due to the absence of well-characterised antibodies [113]. The CB<sub>2</sub>R plays both neuroprotective and immunomodulatory roles. Furthermore, CB<sub>2</sub>R agonists proved to be beneficial for the treatment of neuropathic pain which makes CB<sub>2</sub>R a promising

therapeutic target [114,115]. Finally, CB<sub>2</sub>R activation does not cause psychoactive side effects which are common for CB<sub>1</sub>R agonists [95].

Spinelli *et al.* recently reviewed PET tracers for CB<sub>2</sub>R imaging [95]. Horti *et al.* developed and evaluated [<sup>11</sup>C]A-836339 (agonist, K<sub>i</sub> hCB<sub>2</sub>=0.64 nM) as a CB<sub>2</sub> specific tracer that was evaluated in an LPS induced neuroinflammation mouse model and an Alzheimer's disease mouse model (APP<sup>swe</sup>/PS1dE9 mice) [116]. Recently, Pottier *et al.* used [<sup>11</sup>C]A-836339 to assess CB<sub>2</sub>R expression after cerebral ischemia, LPS and  $\alpha$ -amino-3-hydroxy-5-methyl-4-isoxazolepropionic acid (AMPA) induced models of neuroinflammation in rats [117]. This study demonstrated the lack of increased [<sup>11</sup>C]A-836339 brain retention in the studied animal models. Meletta *et al.* reported [<sup>11</sup>C]RS-016 (K<sub>i</sub> hCB<sub>2</sub>=0.7 nM) as a specific CB<sub>2</sub> PET tracer for visualisation of atherosclerotic plaques. The tracer was however unsuccessful in distinguishing stable from vulnerable plaques [118]. More recently, Caillé *et al.* developed a fluorinated analogue of A-836339 called [<sup>18</sup>F]2f with high affinity for hCB<sub>2</sub>R (K<sub>i</sub> hCB<sub>2</sub>R 0.1 nM). [<sup>18</sup>F]2f showed CB<sub>2</sub>-specific and selective retention in rat spleen [119]. Our group has previously reported [<sup>11</sup>C]NE40 (inverse agonist, K<sub>i</sub> hCB<sub>2</sub>=9.6 nM) (Figure 11) as a specific CB<sub>2</sub>R PET tracer. Specific uptake of [<sup>11</sup>C]NE40 was observed in the rodent spleen and a rat model with local overexpression of hCB<sub>2</sub>R in the brain [120,121]. [<sup>11</sup>C]NE40 was further evaluated for its safety and tolerability in healthy human male subjects through biodistribution and dosimetry studies [122].

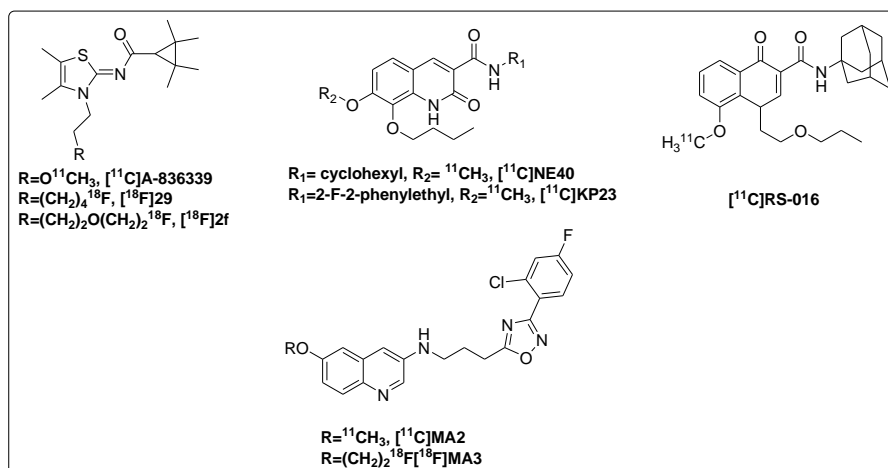


Figure 11: Structures of  $CB_2R$  PET tracers

## 4.2. CSF-1R

CSF-1R, also known as macrophage colony stimulating factor-1 receptor [123] belongs to the class III receptor tyrosine kinase sub-family and is encoded by the *c-fms* proto-oncogene. CSF-1R cognate endogenous ligands are colony stimulating factor-1 (CSF-1) and interleukin-34 (IL-34) [124,125]. The binding of these ligands to CSF-1R triggers an intrinsic tyrosine-specific protein kinase activation, which is vital for proliferation, differentiation and survival of microglia and macrophages [126]. CSF-1R plays an essential role in a broad spectrum of pathological conditions including (neuro)inflammation, cancer, and bone diseases [127–130]. High cell surface expression of CSF-1R was observed on cells such as microglia, macrophages, monocytes, dendritic cells and osteoclasts, while low levels were found in haematopoietic stem cells (HSC) [128].

Green and colleagues reported the importance of CSF-1R for the development of microglia. Their experiments demonstrated that the presence of microglia in the adult mouse brains solely depends on CSF-1R signalling. In the aforementioned intriguing study, the administration of a small molecule CSF-1R inhibitor (PLX3397 from Plexxikon) eliminated 90 % of the microglia from mouse brain (Figure 12). Once the inhibitor was withdrawn, the microglia repopulated the



mouse brain within two weeks. Interestingly, the microglia appeared to originate from the progenitor cells in the brain, rather than infiltrating from the peripheral bloodstream. Henceforth CSF-1R inhibitors can be used to study the role of microglia in neuroinflammation associated with neurodegeneration, traumatic brain injuries and brain cancers [131].

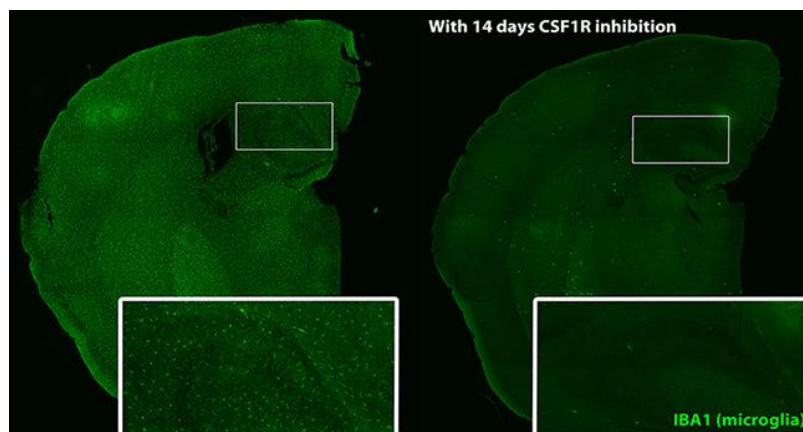


*Figure 12: Inhibition with CSF-1R inhibitor PLX3397 eliminates microglia from the adult mouse brain (Green et al., [131])*

Tumour-associated macrophages (TAMs) are M2 type macrophages derived from monocytes, which are located mainly in the tumour microenvironment [132]. These TAMs release CSF-1, the cytokine responsible for CSF-1R stimulated proliferation, survival and differentiation of macrophages. Overexpression of CSF-1 has been associated with activation and recruitment of TAMs in various cancers types [133]. Overexpression of CSF-1 and CSF-1R in tumours is perceived as an indicator of poor prognosis [134].

Rheumatoid arthritis (RA) is a recurring inflammatory condition resulting in joint destruction, scars and deformity. RA is an autoimmune disease caused by a disruption of bone homeostasis that is controlled by the delicate balance between osteoclast and osteoblast function [135]. The level of synovial macrophages and their release of inflammatory cytokines were found to be the pathological cause of RA. Molecules that can inhibit survival, activation and differentiation

of macrophages via inhibiting CSF-1R or its ligands might have the potential for treatment of RA [128].

Several classes of small molecule CSF-1R inhibitors have been developed, and their characteristics and application have been discussed in a comprehensive review by El Gamal *et al.* [128]. Although small-molecule antagonists with nanomolar affinity [136] have been reported for CSF-1R, there was no specific radiotracer available for visualising CSF-1R with PET. Bernard-Gauthier *et al.* have reported the synthesis of a dual Trk/CSF-1R PET tracer [<sup>18</sup>F]10, but its biological evaluation was not (yet) reported [137].

### ***4.3. G-protein coupled receptor 84***

GPR84 belongs to the orphan receptors of the rhodopsin superfamily and is a member of the free fatty acid (FFA) sensing GPCRs [138–140]. It has been reported that medium chain fatty acids (MCFAs) with carbon chain length of 9-12 can activate GPR84 [141,142]. However no specific endogenous ligand for GPR84 was identified so far, and the physiological functions of GPR84 remain largely unknown [141].

GPR84 was identified to be predominantly expressed on myeloid cells (e.g. monocytes, macrophages, microglia, and neutrophils), suggesting a role of GPR84 in immunological functions [142,143]. In the CNS, several transcriptome analyses confirmed GPR84 expression on microglia [144,145]. GPR84 is highly upregulated under various inflammatory conditions such as endotoxemia and experimental autoimmune encephalomyelitis indicating a direct correlation of GPR84 upregulation with neuroinflammatory conditions [139,146]. Importantly, GPR84 was also found to play a crucial role in experimentally induced neuropathic pain [147].

Currently, there are no specific antibodies available to study GPR84 expression. Therefore, it might be interesting to have radiotracer to visualise the GPR84 expression in healthy and various pathological conditions.

## 5. Aim and thesis outline

Neuroinflammation is a complex well-orchestrated response to various noxious stimuli aiming to restore tissue homeostasis. Under pathological conditions, neuroinflammation can increase tissue damage. Accurate and reliable detection of neuroinflammation is of fundamental clinical interest. To date, numerous neuroinflammation related targets for PET tracer development have been explored, yet, there is a high demand to develop novel diagnostic imaging markers that can distinguish between neurotoxic and neuroprotective microglia. The present doctoral research endeavours to find an ideal biomarker for the visualisation of neuroinflammation.

**Chapter II** describes the synthesis and evaluation of MA-PB-1, a structural analogue of JW642 that shows high affinity to *hMAGL*.

**Chapter III** describes the *in vivo* evaluation of the previously reported brain penetrable CB<sub>2</sub>R agonists PET tracer [<sup>18</sup>F]MA3.

**Chapter IV** describes the development and evaluation of CSF-1R PET tracers based on a high affinity (1 nM) CSF-1R inhibitor with favourable clogD (2.5) and cPSA (72 Å<sup>2</sup>) that was developed by Johnson and Johnson.

**Chapter V** describes exploration of radiolabelled G1055611, a derivative of the GPR84 antagonist GLPG1205 developed by Galapagos.



## CHAPTER-II

### **Synthesis and preclinical evaluation of [<sup>11</sup>C]MA-PB-1 for *in vivo* imaging of brain Monoacylglycerol Lipase (MAGL)**

*Muneer Ahamed<sup>‡a</sup>, Bala Attili<sup>‡a</sup>, Daisy van Veghel<sup>a</sup>, Maarten Ooms<sup>a</sup>, Philippe Berben<sup>a</sup>, Sofie Celen<sup>a</sup>, Michel Koole<sup>b</sup>, Lieven Declercq<sup>a</sup>, Juha R Savinainen<sup>c</sup>, Jarmo T Laitinen<sup>c</sup>, Alfons Verbruggen<sup>a</sup> and Guy Bormans<sup>\*a</sup>*

<sup>a</sup>Laboratory for Radiopharmaceutical Research, department of Pharmaceutical and Pharmacological Sciences, Campus Gasthuisberg O&N2, Herestraat 49 Box 821, BE-3000 Leuven, Belgium.

<sup>b</sup>Department of Nuclear Medicine & Molecular Imaging, UZ Herestraat 49, 3000 Leuven, Belgium.

<sup>c</sup>Institute of Biomedicine, Faculty of Health Sciences, The University of Eastern Finland, Finland.

#### **Corresponding author:**

\*Prof. Guy Bormans, Address: O&N2, Herestraat 49, box 821, BE-3000 Leuven, Belgium; Tel: +32 (0)16 330447; Fax: +32 (0)16 330449; E-mail: guy.bormans@kuleuven.be

<sup>‡</sup>*These authors contributed equally*

European Journal of Medicinal Chemistry (2017), 136:104-113



**ABSTRACT**

MAGL is a potential therapeutic target for oncological and psychiatric diseases. Our objective was to develop a PET tracer for *in vivo* quantification of MAGL. We report [<sup>11</sup>C]MA-PB-1 as an irreversible MAGL inhibitor PET tracer. The *in vitro* inhibitory activity, *ex vivo* distribution, brain kinetics and specificity of [<sup>11</sup>C]MA-PB-1 binding were studied. *Ex vivo* biodistribution and microPET showed good brain uptake which could be blocked by pre-treatment with both MA-PB-1 and a structurally non-related MAGL inhibitor MJN110. These initial results suggest that [<sup>11</sup>C]MA-PB-1 is a suitable tracer for *in vivo* imaging of MAGL.

*Key Words:* MAGL, [<sup>11</sup>C]MA-PB-1, MJN110, biodistribution, PET imaging

## 1. Introduction

The endocannabinoid system consists of cannabinoid receptors, endogenous ligands and other proteins for their synthesis, degradation and transport [148,149]. In the CNS, the endocannabinoid system plays an important role in the regulation of several physiological functions such as cognition, pain, movement and memory [98,99]. Two of the most important and widely studied endogenous lipid transmitters are *N*-arachidonoyl ethanolamine or anandamide (AEA) and 2-arachidonoylglycerol (2-AG) [150]. These two endocannabinoids are synthesised on demand in response to neuronal activity. The signal is then rapidly terminated due to the breakdown of the endocannabinoids by the enzymatic activity of two serine hydrolases: fatty acid amide hydrolase (FAAH) and monoacylglycerol lipase (MAGL), respectively [100].

MAGL is a 33-kDa cytosolic serine hydrolase enzyme that preferentially cleaves monoacylglycerols into fatty acids and glycerol and plays a crucial role in coordinating multiple lipid signalling pathways. In the brain, MAGL was found to be co-localized with CB<sub>1</sub> receptors in axon terminals where it is responsible for approximately 85% of 2-AG hydrolysis [101,102]. Therefore, MAGL is an important terminating factor of the endocannabinoid signalling activity. Additionally, MAGL also plays an important role in the release of arachidonic acid (AA) and other free fatty acids like prostaglandin E<sub>2</sub> (PGE<sub>2</sub>) and lysophosphatidic acid (LPA). It is well established that AA is metabolised to pro-inflammatory prostaglandins and the free fatty acids generate pro-tumorigenic signalling lipids [103,151].

Because of its crucial role in several lipid signalling pathways, MAGL is known to be involved in many pathological conditions, such as inflammation, cancer, neurodegenerative disorders and several psychological disorders such as anxiety and depression [103]. Blockage of MAGL leads to increased 2-AG levels and enhanced endocannabinoid signalling [152]. Additionally, blockage of MAGL also lowers AA levels, which in turn leads to decreased production of pro-



inflammatory prostaglandins. Therefore, MAGL inhibition could play an important role in several diseases. Indeed, previous studies have shown that MAGL blockade has several beneficial outcomes in inflammation, pain, anxiety, neurodegeneration and cancer [103,153–156]. In the recent past, a number of selective and potent MAGL inhibitors have been developed to modulate MAGL activity [104,157–160]. Cravatt *et al.* identified some interesting carbamate containing small molecule inhibitors of MAGL, particularly JW642 was reported to have an IC<sub>50</sub> value of 3.7 nM for *h*MAGL [104].

Non-invasive imaging of MAGL using positron emission tomography (PET) can assist in the translational evaluation of promising drug candidates targeting MAGL. Furthermore, PET imaging of MAGL also allows quantifying MAGL expression *in vivo* thus allowing for identifying modulation of MAGL in relevant pathologies. Therefore, the development of a suitable PET radioligand to visualise MAGL is important.

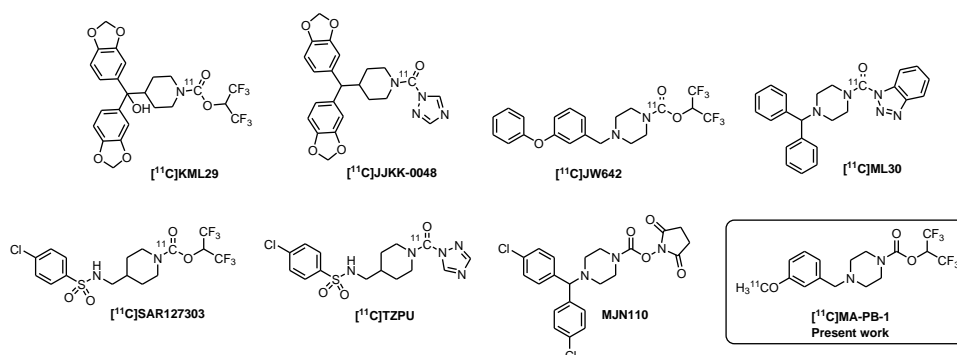


Figure 1: Structures of recently reported MAGL PET tracers and of MA-PB-1 (radiotracer developed and studied in this work), MJN 110 MAGL inhibitor used for blocking studies.

Hicks and co-workers reported PET radioligands for imaging of MAGL [105]. Four ligands labeled with carbon-11 at a carbonyl carbon, namely [11C]-KML29, [11C]-JW642, [11C]-ML-30 and [11C]-JJKK-0048 and a [11C]CH<sub>3</sub>-labeled 1,2,4-triazole urea compound were studied. These compounds were reported to have moderate BBB penetration (0.2-0.8 SUV at 2 and 40 min in mice), but brain retention could not be self-blocked. The lack of MAGL-specific brain

uptake led to the conclusion that none of the tracers was suitable for *in vivo* imaging of brain MAGL. While preparing this manuscript, Hooker *et al.* published [<sup>11</sup>C]-SAR127303 as a specific MAGL tracer in rats [106] and Liang *et al.* published comparative study between [<sup>11</sup>C]-SAR127303 and [<sup>11</sup>C]-TZPU [107]. In their results [<sup>11</sup>C]-TZPU does not show adequate brain penetration whereas [<sup>11</sup>C]-SAR127303 does display good brain penetration and awaits further evaluation in non-human primates.

In this study, we modified the structure of JW642 in which the phenoxy group is substituted with a methoxy group resulting in MA-PB-1. We herein report the synthesis, radiosynthesis and preliminary biological evaluation of [<sup>11</sup>C]MA-PB-1 for *in vivo* imaging of MAGL with PET.

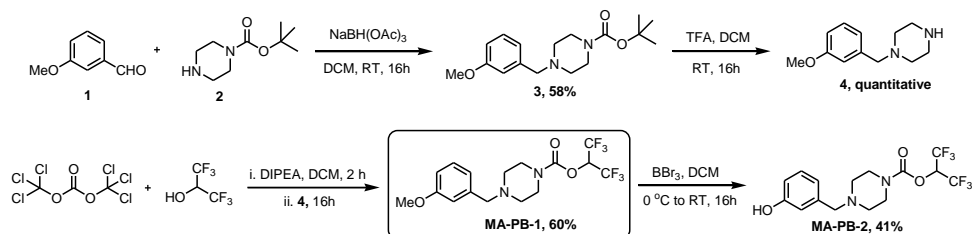
## 2. Results and discussion

Non-invasive imaging of MAGL using PET will allow quantification of regional enzyme expression *in vivo* in healthy and pathological conditions. In general, a successful PET ligand should provide a clear specific signal (signal/noise ratio  $\geq 1.5$ ) to allow quantitative mapping of the target of interest. Ideally, a brain PET tracer should have a high binding affinity with  $B_{\max}/K_d \geq 10$  and a log D of 2–3.5 with PSA value of less than  $90 \text{ \AA}^2$  for adequate brain penetration and optimum specific to nonspecific activity ratio [16,161].

### 2.1. Chemistry

Synthesis of the target compounds MA-PB-1 and MA-PB-2 were carried out based on literature procedures [104] (*Scheme 1*). Compound **4** was synthesised by NaBH(OAc)<sub>3</sub> mediated reductive amination followed by boc deprotection using trifluoroacetic acid (TFA). After complete conversion (monitored by LC-MS) the reaction mixture was neutralized, extracted (DCM/H<sub>2</sub>O), dried and used in the next step without any further purification. The free amine **4**

was converted into MA-PB-1 by adding **4** to a mixture of hexafluoroisopropanol and triphosgene with DIPEA as a base. Finally, MA-PB-1 was demethylated with BBr<sub>3</sub> to yield the phenol precursor MA-PB-2.



Scheme 1: Synthesis of reference and precursor

## 2.2. In vitro affinity studies

Table 1: MAGL inhibitors along with their corresponding IC<sub>50</sub> values, and calculated log D and calculated polar surface area (PSA) values (using Marvin sketch 14.11.10.0), \*results from our assays.

	IC <sub>50</sub> (hMAGL)	clog D (pH 7.4)	cPSA (Å <sup>2</sup> )
<b>KML29</b>	5.9[104] (3.6[160]) nM	4.3	86.7
<b>JJKK0048</b>	4.0[160] nM	2.4	87.9
<b>JW642</b>	37.0*(3.7[104]) nM	5.0	42.0
<b>SAR127303</b>	29.0[106] nM	3.7 (1.9[106])	75.7
<b>ML30</b>	0.5[158] (1.5[160]) nM	3.9	54.3
<b>TZPU</b>	35.9[107] nM	0.9 (0.7[107])	97.2
<b>MA-PB-1</b>	26.0* nM	3.4	42.0
<b>MJN110</b>	11.0* (9.1[162]) nM	3.1	66.9

*Table 1* compares the *hMAGL* IC<sub>50</sub> values and the clog D and cPSA values of various reported *MAGL* inhibitors. IC<sub>50</sub> values should be interpreted with caution as values were compiled from literature reports and were thus not obtained using the same assay except for JW642, MA-PB-1 and MJN110 which were assayed in this study.

JW642 was reported to have a *hMAGL* IC<sub>50</sub> of 3.7 nM [104] and calculated log D and PSA values of 5.0 and 42.0, respectively. In our experiments assessing *hMAGL*-catalyzed hydrolysis of 2-AG [163,164], we observed an IC<sub>50</sub> of 37 nM for JW642. In the parallel assay, we found an IC<sub>50</sub> (*hMAGL*) value of 26 nM for MA-PB-1. Calculated log D and PSA values of MA-PB-1 were 3.4 and 42.0, respectively. The substitution of the phenoxy with a methoxy group although not affecting inhibitor potency in a statistically significant manner decreased the clog D value and is still within the good range for efficient BBB passage.

### **2.3. Radiochemistry**

The radiolabelled compound [<sup>11</sup>C]MA-PB-1 was obtained by alkylation of the phenolic precursor (MA-PB-2) with [<sup>11</sup>C]methyl iodide at 70 °C in DMF in the presence of a base (*Figure 2*). [<sup>11</sup>C]MA-PB-1 was synthesised with a radiochemical yield of 40% (n = 11, based on HPLC recovered activity). The radiolabelled reaction product could be efficiently purified from unreacted precursor and other chemical and radiochemical impurities using the described preparative HPLC system, resulting in [<sup>11</sup>C]MA-PB-1 with a high radiochemical purity (≥99%) and high specific activity (58 - 400 GBq/μmol, n=11), in a total synthesis time of 45 min.

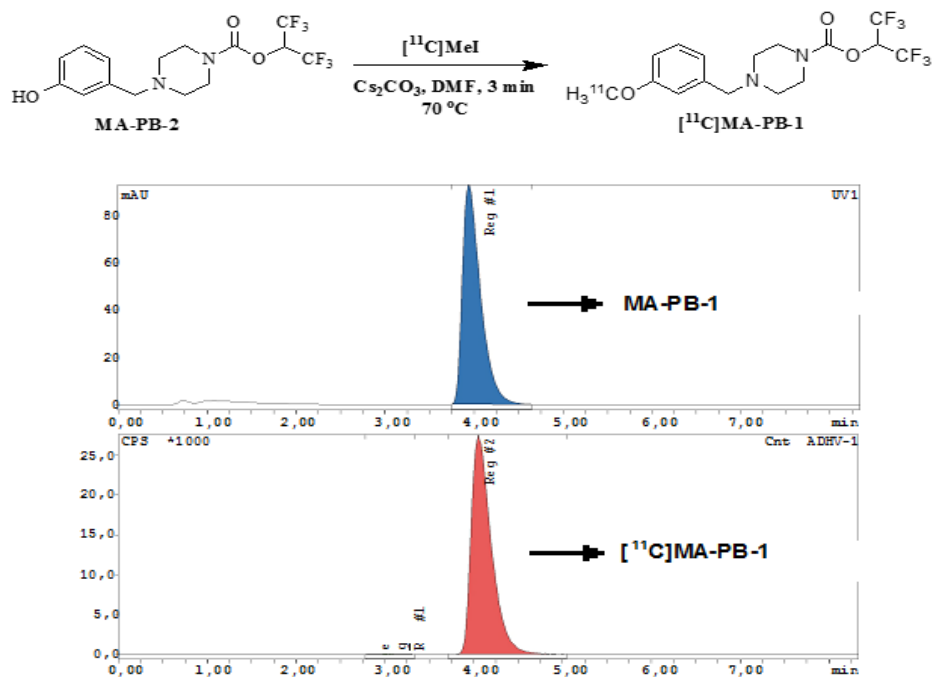


Figure 2:  $\text{MA-PB-2}$  was methylated with  $[^{11}\text{C}]\text{MeI}$  yielding  $[^{11}\text{C}]\text{-MA-PB-1}$  with  $\geq 99\%$  radiochemical purity after preparative HPLC purification. Retention times of reference and radiolabelled  $\text{MA-PB-1}$  were identical (co-injection of  $10\ \mu\text{g/mL}$   $\text{MA-PB-1}$  onto analytical HPLC system). Chromatographic conditions of the quality control: XBridge C18 RP column ( $3.5\ \mu\text{m}$ ,  $3.0\ \text{mm} \times 100\ \text{mm}$ ), Mobile phase:  $\text{CH}_3\text{CN}/\text{NaOAc}$   $0.05\ \text{M}$  pH 5.5 (55:45 v/v), Flow rate:  $0.8\ \text{mL/min}$ , detection: UV 210 nm (upper chromatogram) and radioactivity (lower chromatogram).

#### 2.4. Ex vivo biodistribution and regional brain distribution in mice

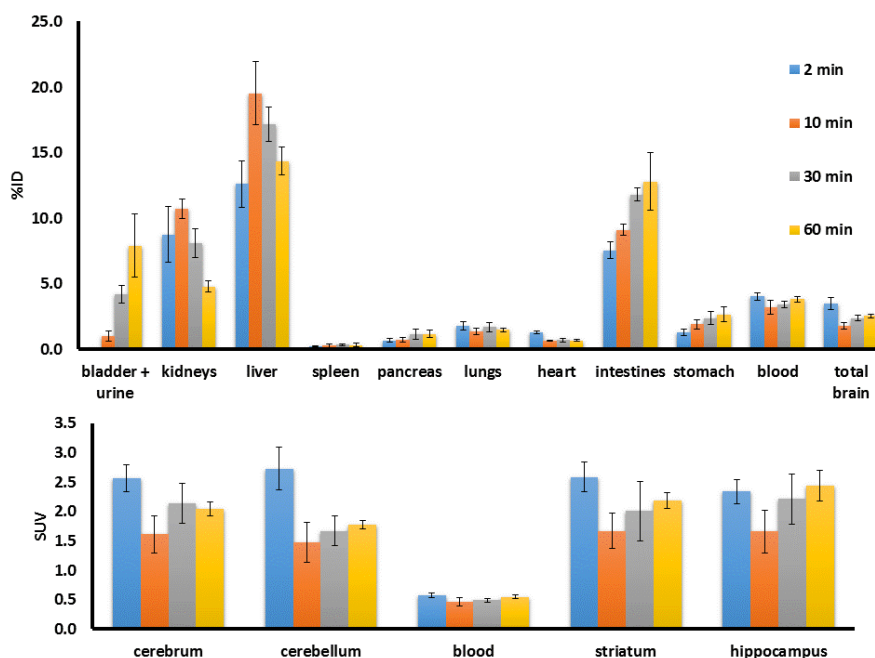


Figure 3: Biodistribution and regional brain distribution of  $[^{11}\text{C}]\text{MA-PB-1}$  in mice at 2, 10, 30 and 60 min post tracer injection in baseline conditions. The top figure shows the general distribution (%ID) of the tracer in adult female NMRI mice at different time points post-injection ( $n=4$  / time point). The bottom figure shows the relative regional brain and blood concentrations (SUV) at different time points post-injection ( $n=4$  / time point).

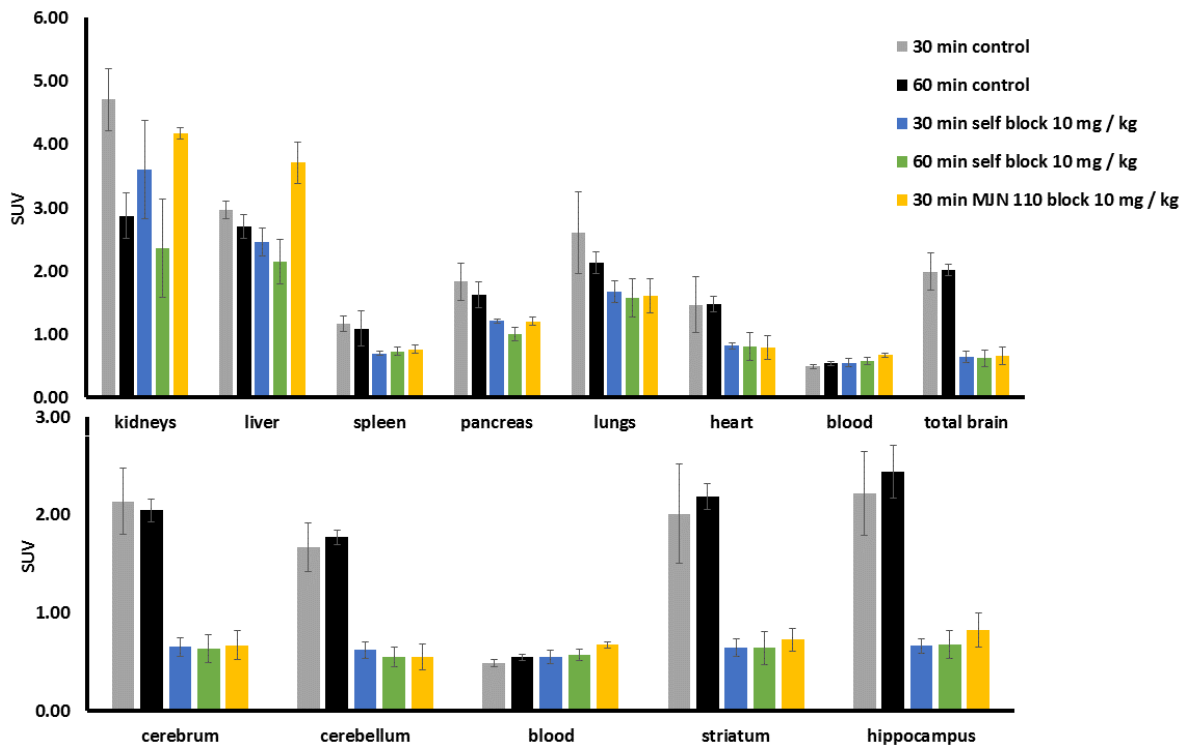


Figure 4: Biodistribution and regional brain distribution of  $[^{11}\text{C}]\text{MA-PB-1}$  in mice at 30 min and 60 min p.i. in baseline conditions and 30 or 60 min after pre-treatment with cold MA-PB-1 (10 mg/kg i.p.) and 30 min after pre-treatment with MJN110 (10 mg/kg, i.p.). The concentration in the different organs, brain regions and fluids is expressed as SUV values.

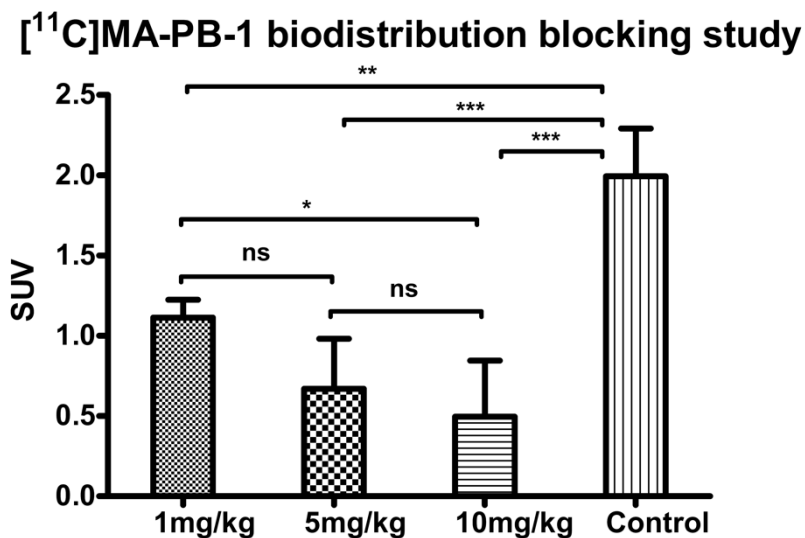


Figure 5: Blocking study with 1 mg/kg, 5 mg/kg and 10 mg/kg doses of MJN110 compared with control conditions. (ns=  $P \geq 0.05$ , \* =  $P \leq 0.05$ , \*\* =  $P \leq 0.01$ , \*\*\* =  $P \leq 0.001$ ). Results expressed as SUV in mouse brain at 30 min post tracer injection.

The data of the baseline biodistribution studies are summarised in *Figure 3* and show a transient accumulation of  $[^{11}\text{C}]\text{MA-PB-1}$  in liver (14.4 %ID at 60 min p.i.) with transfer to the intestines

(12.8 %ID at 60 min p.i.). This can be explained by the lipophilic nature of the compound resulting in hepatobiliary clearance from the blood. Apart from the hepatobiliary clearance, [ $^{11}\text{C}$ ]MA-PB-1 showed a significant clearance through the renal pathway (7.9 %ID in bladder plus urine at 60 min p.i.). Despite the excretion through both the renal and hepatobiliary system, clearance of [ $^{11}\text{C}$ ]MA-PB-1 from blood was rather slow ( $3.8 \pm 0.2$  % ID at 60 min p.i.). This retention does not seem to be caused by MAGL binding of [ $^{11}\text{C}$ ]MA-PB-1 in blood cells or plasma [165] as we did not observe any blocking effect in the blood (*Figure 4*). However, plasma radiometabolite analysis indicated fast metabolism with only 6% of the intact [ $^{11}\text{C}$ ]MA-PB-1 present in blood at 30 min p.i. Retention of radiometabolites in the blood may thus explain the slow blood clearance.

Importantly, [ $^{11}\text{C}$ ]MA-PB-1 showed a high brain uptake (average  $\text{SUV}_{\text{whole brain}} = 2.6$  at 2 min p.i.) which can be explained by its favourable clog D and cPSA values (*Table 1*). Investigation of the regional brain distribution of the tracer showed a uniform distribution of [ $^{11}\text{C}$ ]MA-PB-1 amongst the studied brain regions (*Figure 3*) which are in accordance to the reported uniform MAGL distribution in the brain [166]. After the high initial uptake, [ $^{11}\text{C}$ ]MA-PB-1 partially washed out followed by accumulation in the brain between 10 and 60 min to reach a steady state concentration ( $\text{SUV}_{\text{total brain}} = 1.6 \pm 0.3$ ). These observations are in accordance with the kinetics of an irreversible tracer. Because of the retention of tracer in the brain, high brain-to-blood ratios (calculated as  $\text{SUV brain}/\text{SUV blood}$ ) was achieved (4.1 and 3.7 at 30 and 60 min p.i., respectively) despite the slow clearance of radioactivity from the blood.

To verify the binding specificity, biodistribution studies were performed at 30 and 60 min post tracer injection in mice that were pre-treated with cold MA-PB-1 (10 mg/kg, *i.p.*) 60 min before injection of the tracer. Additionally, a blocking experiment was conducted in which the biodistribution was studied at 30 min post tracer injection in mice that were injected with the non-structurally related MAGL inhibitor MJN110 (10 mg/kg, *i.p.*) 30 min before tracer

injection. Results of both blocking experiments are shown in *Figure 4*. The pre-treated mice showed a significantly lower [ $^{11}\text{C}$ ]MA-PB-1 retention in the brain compared to untreated animals ( $p=0.0007$ ). Whole brain SUV values were about 70% lower in mice pre-treated with cold MA-PB-1 compared to vehicle-treated animals at both the 30 and 60 min post tracer injection scarification time points. As a result, brain-to-blood ratios were significantly lower in the MA-PB-1 pre-treated mice (1.2 and 1.1 at 30 and 60 min p.i., respectively). Pre-treatment of animals with MJN110 also resulted in a significant reduction of total [ $^{11}\text{C}$ ]MA-PB-1 retention (SUV =  $0.7 \pm 0.1$ , 30 min p.i.) in the brain compared to vehicle treated animals. It is noteworthy that blocking studies performed at 1 mg/kg, 5 mg/kg and 10 mg/kg MJN110 demonstrated a significant difference in brain SUV concerning the control. Although blocking generally follows a dose-dependent trend, the observed difference was not significant except between 1 mg/kg and 10 mg/kg (*Figure 5*). We expected that at 1 mg/kg we would observe maximum blocking in line with previously reported results [162], but we observed stronger blocking effect after pre-treatment with 10 mg/kg. Likewise, the blocking effect was also observed in peripheral organs such as spleen, pancreas, heart and lungs, major organs where MAGL expression has been reported in various organs [166].

### ***2.5. Plasma radiometabolite quantification in rats***

Radio-HPLC of rat plasma (at 30 min post tracer injection) showed three peaks. From co-injection of plasma with authentic reference compound, we could identify the peak with retention time of approximately 10 min as intact [ $^{11}\text{C}$ ]MA-PB-1. The major radiometabolite was a polar radiometabolite eluting around 4 min. A second apolar radiometabolite eluted around 15 min. Our data suggest that [ $^{11}\text{C}$ ]MA-PB-1 is rapidly metabolised *in vivo*, since 30 min after injection of [ $^{11}\text{C}$ ]MA-PB-1, only 6% of the radioactivity in plasma was assigned to intact parent tracer. 28% (n=3) of plasma activity could not be extracted from the protein denatured fraction which may indicate covalent binding of the tracer to plasma.



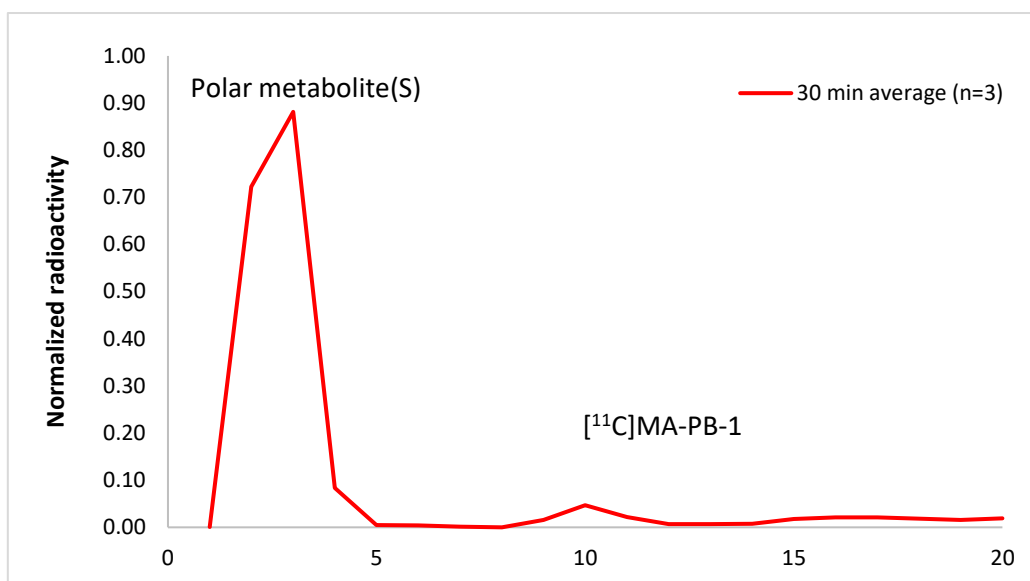


Figure 6: Plasma radiometabolite analysis of [ $^{11}\text{C}$ ]MA-PB-1 30 min post tracer injection and reconstructed chromatogram.

## 2.6. Perfused brain radiometabolite quantification in rats

To quantify radiometabolites formed in or entering the brain, a perfused brain radiometabolite analysis in rats was performed. The extraction efficiency from brain was low (15-30%) suggesting irreversible binding of the tracer to brain MAGL which is associated to the pellet of denatured proteins that precipitate upon addition of  $\text{CH}_3\text{CN}$  to the brain homogenate. A relatively low amount of radiometabolites more polar than the intact tracer was found in brain (<10% of total brain activity; 90% of non-protein bound tracer at 30 min p.i.), indicating that the radiometabolites found in plasma at the same time point show limited brain uptake.

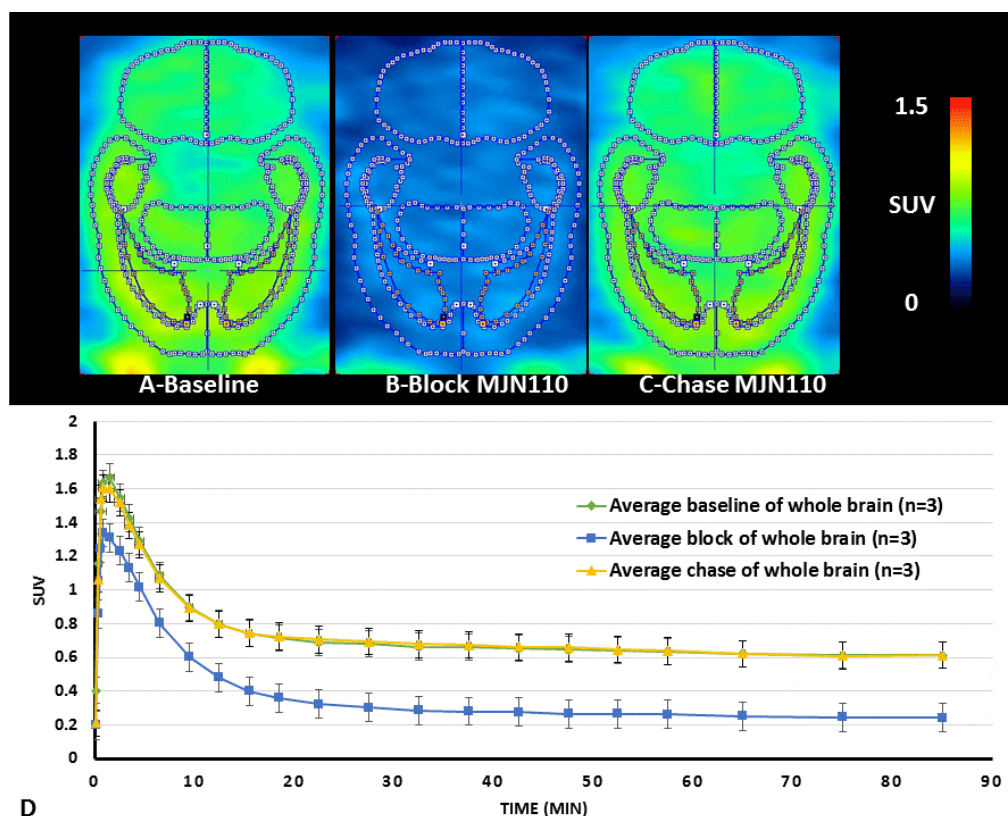
2.7. *In vivo microPET studies in rats*

Figure 7: MicroPET images (horizontal section) showing brain distribution and corresponding TACs describing brain kinetics after i.v. injection of 55 MBq [ $^{11}\text{C}$ ]MA-PB-1 in rats under gaseous anaesthesia (isoflurane 2.5% in  $\text{O}_2$ , 1 L/min). The top figure shows averaged summed images (0-90 min) from three animals: baseline (A), after blocking with MJN110 (10 mg/kg i.p. 30 min before tracer injection, B) and after a chase with MJN110 (10 mg/kg i.v. 20 min after tracer injection, C). The graph (D) shows the TACs, the average whole brain kinetics in baseline conditions, after blocking and in chase conditions as a function of time.

*In vivo* brain distribution and kinetics of [ $^{11}\text{C}$ ]MA-PB-1 were studied using microPET imaging in rats (n=3). A group of female Wistar rats (n=3) was scanned at baseline conditions. Additionally, a blocking and displacement study was set up using MJN110 to check the specificity and reversibility of the tracer binding. Since the same animals were used for baseline, blocking and chase experiments, each baseline scan was used as an internal reference for the other scans. An overview of the microPET results can be found in Figure 7. Averaged microPET images in baseline conditions showed a high-intensity signal in the brain (Figure 7A). Analysis of the corresponding time-activity curves (TACs) showed retention of [ $^{11}\text{C}$ ]MA-PB-1 in the brain. After high initial uptake of [ $^{11}\text{C}$ ]MA-PB-1 (SUV of  $\sim 1.6$  at 2 min), activity

in the brain rapidly decreased to reach stable values starting from 20 min p.i. (average SUV whole brain 30-90 min = 0.6). The initial brain uptake of [<sup>11</sup>C]MA-PB-1 (1.6 and 2.6 SUV in rats and mice, respectively at 2 min p.i.) is comparable with the recently reported [<sup>11</sup>C]-SAR127303 tracer [106] (SUV value of 1.7 at 2 min in rats) and 4 times higher than [<sup>11</sup>C]-TZPU [107] (SUV value 0.4 at 2 min in rats). *In vivo* studies with [<sup>11</sup>C]-SAR127303 and [<sup>11</sup>C]-TZPU showed that the radioactivity in brain remained stable with no significant clearance even after 60 min. However, with [<sup>11</sup>C]MA-PB-1 after the high initial brain uptake, a significant washout from rat brain was observed, with SUV values decreasing from ~1.6 at 2 min p.i. to ~0.6 at 60 min p.i. (*Figure 7D*). This is in contrast with the biodistribution results obtained in mice, where the radioactivity in brain remained stable even at 60 min p.i. and likely this could be attributed to species difference (*Figure 3*).

Specificity of [<sup>11</sup>C]MA-PB-1 binding to MAGL *in vivo* was tested in a blocking study in which the same rats from the baseline scan (n=3) were pre-treated with the structurally unrelated MJN110 (10 mg/kg, *i.p.*, 30 min before tracer injection). After blocking, the retention of [<sup>11</sup>C]MA-PB-1 in the brain was significantly reduced resulting in only background signal in the brain (*Figure 7B*). The significant blocking effect could also be observed *via* the TAC analysis. Equilibrium SUV values in the different brain regions (average SUV total brain 30min - 90min = 0.26) were about 60% lower compared to SUV values in baseline conditions acquired in the same rats. Pre-treatment with cold MA-PB-1 also showed a significant blocking effect both in *ex vivo* biodistribution and *in vivo* microPET studies (data not shown). These microPET data confirm that a high proportion of the [<sup>11</sup>C]MA-PB-1 specifically binds to brain MAGL *in vivo* in rats as was also observed in biodistribution studies in mice.

Finally, in a microPET displacement study, the same rats (n=3) were injected with [<sup>11</sup>C]MA-PB-1 followed by *i.v.* challenge with MJN110 (10 mg/kg) at 20 min post tracer injection. An averaged microPET image of all three rats in the chase experiment is shown in *Figure 7C*.

TACs of the brain after chase are similar to those acquired in baseline conditions. This lack of displacement of radioactivity after injection of a high dose of MJN110 was expected due to the irreversible nature of the [ $^{11}\text{C}$ ]MA-PB-1 binding. Similarly, Hooker *et al.* performed a chase study by injection of cold SAR127303 (20 min p.i. of [ $^{11}\text{C}$ ]-SAR127303) and observed that brain uptake was not affected.

### **2.8. Non-human primate rhesus monkey microPET**

The results of the 90-min baseline and pre-treatment scan of [ $^{11}\text{C}$ ]MA-PB-1 in monkey are shown in *Figure 8*. TACs of the baseline scan of [ $^{11}\text{C}$ ]MA-PB-1 in the brain show a fast and high initial brain uptake (SUV of  $\sim 4.2$  in the whole brain, time to peak uptake: 2.5 min). After 20 min the brain activity reaches a steady state (SUV value of about 2.5), suggesting irreversible binding of the radiotracer. For comparison, the brain SUV of [ $^{11}\text{C}$ ]-SAR127303 gradually increased as a function of time to reach about 0.8 at steady state. A homogeneous distribution of [ $^{11}\text{C}$ ]MA-PB-1 was recorded in all observed brain regions, with lower initial uptake in the caudate and highest in the prefrontal cortex. The SUV signal of the pre-treatment scan was decreased (SUV of 1 after 20 min and 0.3 after 40 min in the whole brain).

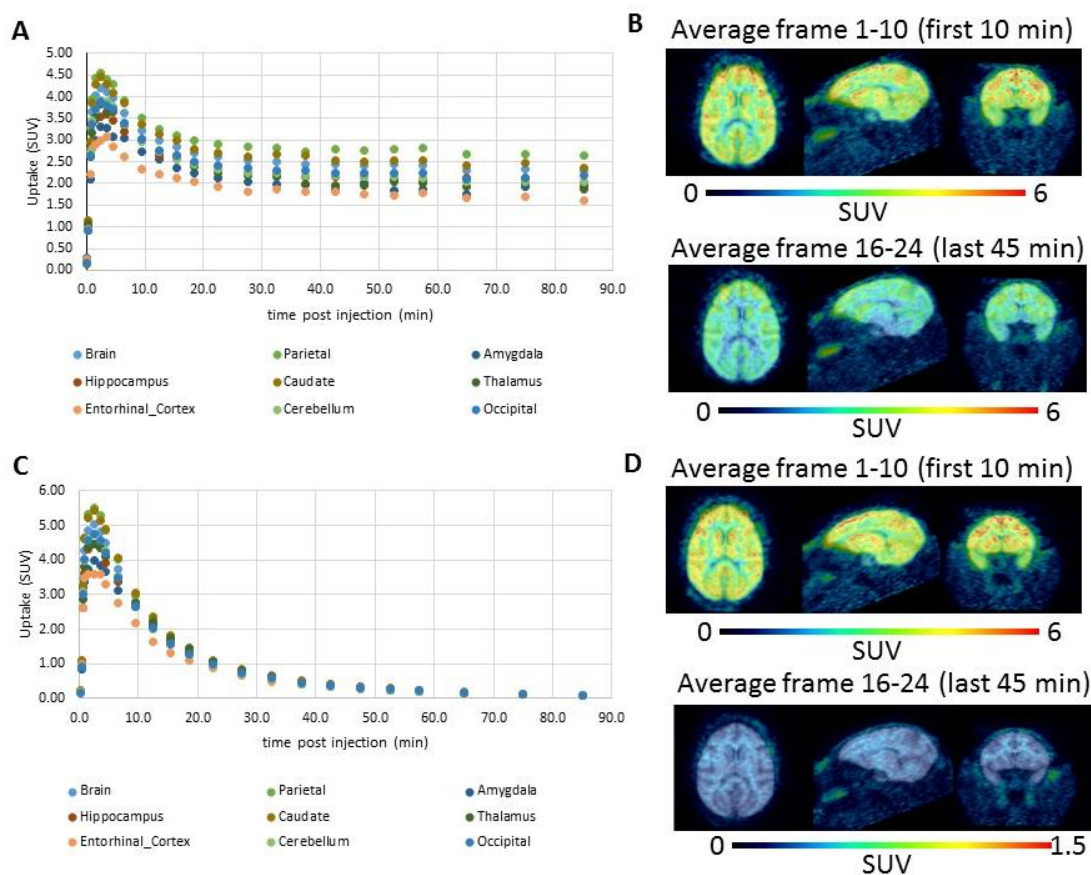


Figure 8:  $\mu$ PET TACs for  $[^{11}\text{C}]\text{MA-PB-1}$  of the whole monkey brain and various brain regions: Baseline (A) and after pre-treatment with MJN110 (1 mg/kg i.v. 10 min before tracer injection, C). Transversal, sagittal and coronal  $\mu$ PET images of the baseline (B) and pre-treatment (D) experiment with  $[^{11}\text{C}]\text{MA-PB-1}$ : averaged images from 1-10 min and from 45-90 min after tracer injection.

### 3. Conclusion

We successfully synthesised MA-PB-1, and radiolabelled  $[^{11}\text{C}]\text{MA-PB-1}$  in good yields, and high radiochemical purity and specific radioactivity. Substitution of the phenoxy group with a methoxy group in JW642 although not affecting inhibitor potency in a statistically significant manner, decreased the clog D which may contribute to increased brain exposure of MA-PB-1. Significant brain uptake of  $[^{11}\text{C}]\text{MA-PB-1}$  was observed in biodistribution and microPET imaging experiments in mice, rats and monkey. Self-blocking experiments confirmed the specificity of binding. Blocking and chasing studies with the structurally non-related MAGL

inhibitor MJN110 in mice, rats and monkey established [<sup>11</sup>C]MA-PB-1 as a MAGL specific irreversible tracer meriting further evaluation.

#### **4. Materials and methods**

##### ***4.1. General materials and methods***

All the chemicals employed in the synthesis were purchased from commercially reliable suppliers (Aldrich, TCI Europe or ACROS) and used without further purification unless stated. <sup>1</sup>H and <sup>13</sup>C Nuclear magnetic resonance (NMR) spectra were obtained on a 400 MHz and 101 MHz Bruker NMR spectrometer in the deuterated solvents as indicated and with tetramethylsilane, TMS ( $\delta = 0$ ), as an internal standard. Chemical shifts ( $\delta$ ) are reported in ppm, and coupling constants are reported in Hertz. Multiplicity is defined by s (singlet), d (doublet), t (triplet), and m (multiplet). The mass spectra were recorded on a Bruker maXis impact UHR-TOF mass spectrometer coupled to a Dionex 3000RS UHPLC system (Bruker-Daltonik, Bremen, Germany).

High-performance liquid chromatography (HPLC) was performed using a Shimadzu LC-2010A HT system connected to a UV spectrometer. Radioactivity in the column eluent was monitored using a 3-in NaI(Tl) scintillation detector connected to a single channel analyser (Gabi box, Raytest, Straubenhardt, Germany). Radioactivity in samples of biodistribution studies and radiometabolite analysis was quantified with an automated gamma counter, equipped with a 3-in NaI(Tl) well crystal coupled to a multichannel analyser (Wallac 1480 Wizard, Wallac, Turku, Finland). The results were corrected for background radiation, detector dead-time and physical decay during counting.

All animals were housed in individually ventilated cages in a thermoregulated (22 °C) and humidity-controlled environment under a 12h/12h day/night cycle with free access to food and

water. All animal experiments were approved by the local Animal Ethics Committee of the University of Leuven (P104/2016) and are in accordance with European Ethics Committee guidelines (decree 86/609/EEC).

## 4.2. Chemistry

### *Tert-butyl 4-(3-methoxybenzyl)piperazine-1-carboxylate, 3*

To a solution of 3-methoxy benzaldehyde, **1** (1.0 g, 7.34 mmol, 1 eq) and *N*-Boc piperazine, **2** (1.05 g, 8.08 mmol, 1.1 eq) in dichloromethane (DCM, 10 mL) at 0 °C was added portionwise NaHB(OAc)<sub>3</sub> (1.87 g, 8.81 mmol, 1.2 eq) and the mixture was stirred at room temperature (RT) for 16h. The reaction mixture was diluted with DCM (150 mL) and washed with H<sub>2</sub>O (2 x 30 mL) and with brine (30 mL). The organic layers were dried over anhydrous MgSO<sub>4</sub> and evaporated under reduced pressure. The crude residue was purified by flash column chromatography using 0-50% EtOAc/heptane mixtures to give compound **3** as a colourless oil (1.30 g, 58%).

<sup>1</sup>H NMR (CDCl<sub>3</sub>, 400 MHz): δ 1.45 (s, 9H, Boc), 2.37-2.40 (m, 4H, 2CH<sub>2</sub>), 3.40-3.44 (m, 4H, 2CH<sub>2</sub>), 3.48 (s, 3H, OMe), 3.80 (s, 1H, CH<sub>2</sub>), 6.79 (d, 1H, *J* 8.0, Ar), 6.87-6.90 (m, 2H, Ar), 7.22 (t, 1H, *J* 7.9, Ar). <sup>13</sup>C NMR (CDCl<sub>3</sub>, 101 MHz): δ 28.61, 53.05, 55.38, 63.15, 79.72, 112.70, 114.78, 121.61, 129.40, 139.75, 154.98, 159.83. HRMS (ESI) Calcd. for C<sub>17</sub>H<sub>27</sub>N<sub>2</sub>O<sub>3</sub> (M+H)<sup>+</sup>: 307.2016. Found: 307.2071.

### *1,1,1,3,3,3-Hexafluoropropan-2-yl 4-(3-methoxybenzyl)piperazine-1-carboxylate, MA-PB-1*

To a solution of triphosgene (0.185 g, 0.624 mmol, 0.33 eq) in dry DCM (5 mL) were added hexafluoroisopropanol (0.197 mL, 1.892 mmol, 1 eq) and diisopropylethyl amine (DIPEA, 0.346 mL, 3.784 mmol, 2 eq) and the reaction mixture was stirred for 2h at RT under N<sub>2</sub>. Compound **3** was boc deprotected using TFA in DCM, the free amine **4** (0.390 g, 1.892 mmol,

1 eq) in DCM (2 mL) was added and the reaction mixture was further stirred at RT for 3h. The mixture was diluted with DCM (100 mL) and washed with H<sub>2</sub>O (2 x 10 mL) and with brine (20 mL). The organic layers were dried over anhydrous MgSO<sub>4</sub> and evaporated under reduced pressure. The crude residue was purified by flash column chromatography using EtOAc/heptane mixtures to give MA-PB-1 as pale yellow oil (0.455 g, 60%).

<sup>1</sup>H NMR (CDCl<sub>3</sub>, 400 MHz): δ 2.42-2.47 (m, 4H, 2CH<sub>2</sub>), 3.50 (s, 2H, CH<sub>2</sub>), 3.54-3.58 (m, 4H, 2CH<sub>2</sub>), 3.80 (s, 3H, OMe), 5.73-5.78 (m, 1H, CH), 6.80 (d, 1H, *J* 8.0, Ar), 6.78 (s, 1H, Ar), 6.89 (d, 1H, *J* 7.2, Ar), 7.23 (t, 1H, *J* 7.9, Ar). <sup>13</sup>C NMR (CDCl<sub>3</sub>, 101 MHz): δ 41.12, 41.52, 49.06, 49.29, 51.93, 59.48, 64.60, 109.38, 111.34, 118.09, 126.08, 135.93, 148.15, 156.48. HRMS (ESI) Calcd. for C<sub>16</sub>H<sub>19</sub>F<sub>6</sub>N<sub>2</sub>O<sub>3</sub> (M+H)<sup>+</sup>: 401.1294. Found: 401.1296. HPLC purity: >98%.

*1,1,1,3,3,3-Hexafluoropropan-2-yl 4-(3-hydroxybenzyl)piperazine-1-carboxylate*, **MA-PB-2**

To a solution of MA-PB-1 (100 mg, 0.25 mmol) in DCM (5 mL) at 0 °C, BBr<sub>3</sub> (~ 0.3 mL) was added and stirred. After 30 min the reaction mixture was allowed to warm to RT and stirred for about 16h. The mixture was neutralised to pH 7, diluted with DCM (50 mL) and washed with H<sub>2</sub>O (2 x 10 mL) and with a saturated NaHCO<sub>3</sub> solution (20 mL). The organic layers were dried over anhydrous MgSO<sub>4</sub> and evaporated under reduced pressure. The crude residue was purified by flash column chromatography using EtOAc/heptane mixtures to give MA-PB-2 as a colourless powder (97 mg, 41%).

<sup>1</sup>H NMR (CDCl<sub>3</sub>, 400 MHz): δ 2.44-2.47 (m, 4H, 2CH<sub>2</sub>), 3.47 (s, 2H, CH<sub>2</sub>), 3.52-3.56 (m, 4H, 2CH<sub>2</sub>), 5.70-5.75 (m, 1H, CH), 6.71 (d, 1H, *J* 8.0, Ar), 6.78 (d, 1H, Ar), 6.87-6.90 (m, 2H, Ar), 7.16 (t, 1H, *J* 7.4, Ar). <sup>13</sup>C NMR (CDCl<sub>3</sub>, 101 MHz): δ 44.30, 44.68, 52.48, 52.70, 53.62, 62.82, 68.32, 114.92, 116.32, 121.69, 129.84, 138.87, 151.64, 156.18. HRMS (ESI) Calcd. for C<sub>15</sub>H<sub>17</sub>F<sub>6</sub>N<sub>2</sub>O<sub>3</sub> (M+H<sup>+</sup>): 387.1137. Found: 387.1140.



### **4.3. Radiosynthesis**

[<sup>11</sup>C]MeI was produced according to the procedure described by Andrés *et al.* [167] and bubbled with a stream of helium through a solution of the radiolabelling precursor (200 µg) and Cs<sub>2</sub>CO<sub>3</sub> (1-3 mg) in anhydrous DMF (200 µL). The mixture was then heated for 3 min at 70 °C. After dilution with 1 mL water, the crude reaction mixture was purified by HPLC using an XBridge C<sub>18</sub> column (5µm, 4.6 mm x 150 mm; Waters, Milford, Connecticut) eluted with a mixture of 0.05 M sodium acetate buffer pH 5.5 and EtOH (43/57 v/v) at a flow rate of 1 mL/min. UV monitoring of the eluate was performed at 254 nm. The peak corresponding to [<sup>11</sup>C]MA-PB-1 was collected, diluted with saline to obtain a final ethanol concentration of <10% and sterile filtered through a 0.22-µm membrane filter (Millex GV 13 mm; Millipore, Billerica, MA). The chemical and radiochemical purity of the tracer was assessed using HPLC on an analytical XBridge C<sub>18</sub> column (3.5 µm, 3.0 mm x 100 mm, Waters) eluted with a mixture of a 0.05 M sodium acetate buffer pH 5.5 and acetonitrile (45/55 v/v) at a flow rate of 0.8 mL/min. UV detection was done at 210 nm. Identity of the tracer was confirmed by co-elution with authentic cold reference on the same HPLC.

### **4.4. Biological Evaluation**

#### **4.4.1. MAGL activity assay**

The assay is based on the principle of the degradation of the 2-AG to AA and glycerol by the endocannabinoid hydrolase MAGL. Glycerol is converted to glycerol-1-phosphate by glycerol kinase. Glycerol phosphate oxidase catalysed oxidation of glycerol-1-phosphate generates H<sub>2</sub>O<sub>2</sub> which in the presence of horseradish peroxidase converts Amplifu™ Red to the fluorescent product Resorufin. Fluorescence is monitored kinetically using excitation and emission wavelengths at 530 and 590 nm respectively. A sensitive fluorescence-based hydrolase assay detecting formation of glycerol was used to determine the rate of *h*MAGL-

catalyzed hydrolysis of the natural monoacylglycerol substrate 2-AG as well as to determine the potency of MAGL inhibitors ( $IC_{50}$  values) in a 96-well format, essentially as previously described [160,163]. The amount of *h*MAGL-lysate protein per well was 0.3  $\mu$ g. This methodology has been previously used allowing comparison of potencies between various MAGL inhibitors, such as JJKK-048, ML30, KML29 and IDFP, under identical experimental conditions [160].

#### 4.4.2. Biodistribution

Biodistribution studies were carried out in healthy adult female NMRI mice (body mass 29 – 50 g) at 2, 10, 30 and 60 min post injection (p.i.) (n = 4 per time point). Additional biodistribution studies (30 and 60 min post tracer injection, n = 4 per time point) were performed 60 min after pre-treatment with cold MA-PB-1 (10 mg/kg; subcutaneous (*s.c.*) administration) or 30 min after pre-treatment with MJN110 (10 mg/kg; *s.c.* administration). MA-PB-1 and MJN110 were dissolved in a vehicle containing 10% DMSO, 10% 2-hydroxypropyl  $\beta$ -cyclodextrin and 5% tween 80 in saline at a concentration of 2 mg/mL. During the procedure, mice were anesthetized with 2.5% isoflurane in O<sub>2</sub> at a flow rate of 1 L/min and injected with about 9 MBq of tracer *via* a tail vein. The animals were then sacrificed by decapitation at above specified time points post tracer injection. Blood and major organs were collected in tared tubes and weighed. The radioactivity in blood, organs and other body parts was counted using an automated gamma counter. For calculation of the total radioactivity in blood, blood mass was assumed to be 7% of the total body mass [168].

#### 4.4.3. Plasma radiometabolite quantification in rats

Healthy Wistar rats (n = 3) were anesthetised with isoflurane (2.5% in O<sub>2</sub> at 1 L/min) and injected intravenously (*i.v.*) with about 55 MBq of the tracer *via* a tail vein. At 30 min p.i., the rats were sacrificed by decapitation and blood was collected in tubes containing 7.2 mg

K<sub>2</sub>EDTA (BD Vacutainer, BD, Franklin Lakes, NJ) and stored on ice. The blood was centrifuged for 10 min (2330 x g) to separate plasma. To about 0.5 mL of plasma, an equal amount of acetonitrile was added, and the solution was vortexed and centrifuged for 5 min (2330 x g) to separate the precipitated proteins from the supernatant. Further, 0.5 mL of supernatant was taken and diluted with 0.1 mL of water. It was filtered through a syringe filter (0.22 µm nylon filter, Acrodisc 13, PALL Life Sciences) and spiked with 20 µg of authentic MA-PB-1. A volume of 0.5 mL of extract was injected onto an HPLC system consisting of an analytical XBridge column (C<sub>18</sub>, 5 µM, 3 mm × 100 mm, Waters) eluted with a mixture of 0.05 M sodium acetate (pH 5.5) and CH<sub>3</sub>CN (45:55 v/v) at a flow rate of 0.7 mL/min. The HPLC eluate was collected as 1-mL fractions after passing through a UV detector (210 nm), and radioactivity in the fractions was measured using an automated gamma counter.

#### *4.4.4. Perfused brain radiometabolite quantification in rats*

Healthy Wistar rats (n = 3) were anesthetized with isoflurane (2.5% in O<sub>2</sub> at 1 L/min) and *i.v.* injected with about 37 MBq of [<sup>11</sup>C]MA-PB-1. At 30 min p.i., they were sacrificed by an overdose of pentobarbital (Nembutal, CEVA Santé Animale, Libourne, France; 200 mg/kg intraperitoneal) followed by cardiac perfusion with saline. Brain was isolated and homogenized/denatured in 3 mL of CH<sub>3</sub>CN, for about 2 min. After centrifugation (1710 x g, 5 min), about 1 mL supernatant was collected, diluted with 1 mL H<sub>2</sub>O, and filtered through a 0.22-µm filter (Millipore, Bedford, MA). About 0.5 mL of the filtrate was diluted with 0.1 mL of water and spiked with 20 µg of authentic MA-PB-1. A volume of 0.5 mL of this brain homogenate extract was injected onto an HPLC system consisting of an analytical XBridge column (C<sub>18</sub>, 5 µM, 3 mm × 100 mm, Waters) eluted with a mixture of 0.05 M sodium acetate (pH 5.5) and CH<sub>3</sub>CN (45:55 v/v) at a flow rate of 0.7 mL/min. The HPLC eluate was collected

as 1-mL fractions after passing through a UV detector (210 nm), and radioactivity in the fractions was measured using an automated gamma counter.

#### 4.4.5. *In vivo microPET studies in rats*

MicroPET imaging experiments were performed on a Focus™ 220 microPET scanner (Concorde Microsystems, Knoxville, TN) using female Wistar rats. During the whole procedure, animals were kept under gas anaesthesia (2.5% isoflurane in O<sub>2</sub> at 1 L/min flow rate). The animal's head was fixed and positioned central in the field of view of the microPET scanner. Upon tracer injection, a dynamic microPET scan was started for 90 min. All scans were acquired in list mode. Acquisition data were Fourier rebinned in 24 time frames (4x15 s, 4x60 s, 5x180 s, 8x5 min, 3x10 min) and reconstructed using maximum a posteriori iterative reconstruction. A summed image of the reconstructed data was spatially normalised to an in-house created <sup>18</sup>F-FDG template of the rat brain in Paxinos coordinates [169] using an affine transformation. The latter was then used to normalize all time frames of the dynamic microPET data set to allow automated and bilateral volumes of interest (VOIs) analyses. Time activity curves (TACs) were generated for whole brains, using PMOD software (v 3.2, PMOD Technologies, Zürich, Switzerland).

In the blocking microPET studies, rats (n = 3) were anaesthetized with 2.5% isoflurane in O<sub>2</sub> at 1 L/min flow rate and *i.p.* injected with MJN110 (10 mg/kg) 30 min prior to tracer injection. For the chase study (n=3), MJN110 (10 mg/kg) was *i.v.* administered 20 min after tracer injection. MA-PB1 and MJN110 were dissolved in a vehicle containing 10% DMSO, 10% 2-hydroxypropyl  $\beta$ -cyclodextrin and 5% tween 80 in saline at a concentration of 2 mg/mL.

#### 4.4.6. Non-human primate Rhesus monkey microPET

Dynamic 90 min  $\mu$ PET scans with [ $^{11}\text{C}$ ]MA-PB-1 were acquired with a Focus 220  $\mu$ PET scanner on a female rhesus monkey (*Macaca mulatta*, 5.2 kg). Sedation was performed by *i.m.* injection of a combination of 0.3 mL Rompun (xylazine 2% solution) and 0.35 ml Nimatek (ketamine 100 mg/mL). About 60 min after the first injection, the monkey received an additional dose of 0.15 mL Rompun and 0.175 mL Nimatek via *i.v.* injection. During the last part of the scan, dosing was done less frequently, based on the heartbeat frequency. The  $\text{O}_2$  and  $\text{CO}_2$  saturation in the blood and the heartbeat were constantly monitored. Temperature was regulated via a heating pad. The breathing frequency and the eye response were checked visually. The head of the animal was placed central in the field of view of the  $\mu$ PET scanner. The monkey was injected with 163 MBq of [ $^{11}\text{C}$ ]MA-PB-1 via the vena saphena. Scans were acquired in list mode and Fourier rebinned in 24-time frames (4 x 15 s, 4 x 60 s, 5 x 180 s, 8 x 300 s, 3 x 600 s). Data were reconstructed using a 3D maximum a posteriori (3D-MAP) iterative reconstruction. TACs of the whole brain were generated using VOIs with PMOD software and radioactivity concentration in the brain is expressed as SUV as a function of time after tracer injection. For the pre-treatment study, MJN110 was dissolved in a vehicle containing 20% DMSO and 40% (2-hydroxypropyl)- $\beta$ -cyclodextrin. Pre-treatment was done by *i.v.* injection of MJN110 at a dose of 1 mg/kg 10 min before tracer injection.  $\mu$ PET images were compared to the baseline scan, acquired in the vehicle-treated monkey. Blood samples were collected during both baseline and pre-treatment scans at 10, 30 and 60 min p.i. *via* the other vena saphena and plasma was analysed for radiometabolites according to the same procedure as described for rats (see above).

### ***5. Data and Statistical analysis***

Quantitative data expressed as mean  $\pm$  SD. Means were compared using an unpaired two-tailed student t-test. Values were considered statistically significant for  $P \leq 0.05$ .

### ***6. Acknowledgements***

We thank Dr. Jacqueline Blankman (Abide Therapeutics, USA) for the useful discussions. We also thank Julie Cornelis (Laboratory for Radiopharmacy; KU Leuven) and Ann Van Santvoort (Department of Nuclear Medicine; KU leuven) for their help with the mice and rat animal studies, Professor Wim Vanduffel and Christophe Ulens from the Laboratory of Neuro-and Psychophysiology for providing the Macaque monkey and assisting in the monkey studies.

### ***7. Funding***

This work was supported by IMIR (In Vivo Molecular Imaging Research group) at KU Leuven, Belgium also funded by the European Union's Seventh Framework Programme (FP7/2007-2013) under grant agreement no. HEALTH-F2-2011-278850 (INMiND)

## CHAPTER-III

### **Preclinical evaluation of [<sup>18</sup>F]MA3, a CB<sub>2</sub> receptor agonist radiotracer for Positron Emission Tomography**

*Bala Attili<sup>1</sup>, Sofie Celen<sup>1</sup>, Muneer Ahamed<sup>1</sup>, Michel Koole<sup>2</sup>, Chris Van den Haute<sup>3,4</sup>, Wim Vanduffel<sup>5</sup>, Guy Bormans<sup>1\*</sup>*

1. Radiopharmaceutical Research, Department of Pharmaceutical and Pharmacological Sciences, KU Leuven, Leuven, Belgium.
2. Department of Nuclear Medicine & Molecular Imaging, UZ Gasthuisberg, Leuven, Belgium.
3. Laboratory for Neurobiology and Gene Therapy, Department of Neurosciences, KU Leuven, Leuven, Belgium.
4. Leuven Viral Vector Core, Molecular Medicine, KU Leuven, Leuven, Belgium
5. Laboratory for Neuro- and Psychophysiology, Department of Neurosciences, KU Leuven, Leuven, Belgium

#### **Corresponding author:**

\*Prof. Guy Bormans, Address: O&N2, Herestraat 49, box 821, BE-3000 Leuven, Belgium; Tel: +32 (0)16 330447; Fax: +32 (0)16 330449; E-mail: [guy.bormans@kuleuven.be](mailto:guy.bormans@kuleuven.be)

Manuscript under revision, British Journal of Pharmacology





## ABSTRACT

**Background and Purpose:** Non-invasive *in vivo* imaging of CB<sub>2</sub> receptors (CB<sub>2</sub>R) using positron emission tomography (PET) is pursued to study neuroinflammation. The purpose of this study is to evaluate the *in vivo* binding specificity of [<sup>18</sup>F]MA3, a CB<sub>2</sub>R agonist, in a rat model with local overexpression of *human* CB<sub>2</sub>R (*hCB<sub>2</sub>R*).

**Methods:** [<sup>18</sup>F]MA3 was produced with good radiochemical yield and radiochemical purity. The radiotracer was evaluated in rats with local overexpression of *hCB<sub>2</sub>R* and in a healthy non-human primate using PET.

**Key results:** *Ex vivo* autoradiography demonstrated CB<sub>2</sub> specific binding of [<sup>18</sup>F]MA3 in rat *hCB<sub>2</sub>R* vector injected striatum. In a PET study, increased tracer binding in the *hCB<sub>2</sub>R* vector injected striatum compared to the contralateral control vector injected striatum was observed. Binding in *hCB<sub>2</sub>R* vector injected striatum was blocked with a structurally non-related CB<sub>2</sub>R inverse agonist, and a displacement study confirmed the reversibility of tracer binding. [<sup>18</sup>F]MA3 PET scans in the non-human primate showed good uptake and fast wash out from the brain, but no CB<sub>2</sub> specific binding was observed.

**Conclusion and Implications:** Evaluation of [<sup>18</sup>F]MA3 in a rat model with local overexpression of *hCB<sub>2</sub>R* showed CB<sub>2</sub> specific and reversible tracer binding. [<sup>18</sup>F]MA3 showed good brain uptake and subsequent wash out in a healthy non-human primate, but no specific binding was observed. Further clinical evaluation of [<sup>18</sup>F]MA3 in patients with neuroinflammation is warranted.

**Key words:** CB<sub>2</sub>R, [<sup>18</sup>F]MA3, PET imaging, neuroinflammation, radiotracer.

### ***1. Introduction***

The endocannabinoid system comprises the type 1 cannabinoid receptor (CB<sub>1</sub>R) and the type 2 (CB<sub>2</sub>R), the endogenous ligands 2-arachidonoyl glycerol (2-AG) and *N*-arachidonoyl ethanolamine (AEA), and other proteins for their biosynthesis and degradation [148]. The CB<sub>1</sub>R and CB<sub>2</sub>R belong to the G-protein coupled receptor family, and they share 44% overall homology [170]. CB<sub>1</sub>R is mainly expressed in the central nervous system with a remarkable level of receptor expression observed in globus pallidus, entopeduncular nucleus, substantia nigra pars reticulata and cerebellum [171]. The expression of CB<sub>1</sub>R was imaged using [<sup>18</sup>F]MK-9470 positron emission tomography (PET) in monkey and humans brains [109]. CB<sub>2</sub>R, on the other hand, is principally expressed in organs with immune functions, and high expression is found in spleen, tonsils and leucocytes [172]. In the brain, the CB<sub>2</sub>R expression is very low under physiological conditions and is mainly detected in Purkinje cells of the cerebellum, hippocampal neurons and brain stem [110]. The expression of CB<sub>2</sub>R is up-regulated during pathological conditions such as (neuro)inflammation and is predominantly observed in the activated microglia of the brain [173]. The CB<sub>2</sub>R play both neuroprotective and immunomodulatory roles. Furthermore, CB<sub>2</sub>R agonists proved to be effective in neuropathic pain which makes CB<sub>2</sub>R a promising therapeutic target [114,115]. Finally, CB<sub>2</sub>R activation does not have psychoactive side effects which are common for CB<sub>1</sub>R agonists [95].

Non-invasive imaging of CB<sub>2</sub>R with PET has a promising role in identifying neuropathological changes. Hence, it might be beneficial for diagnosis and treatment follow up of neurodegenerative disorders such as Alzheimer's, Parkinson's, Huntington's disease, Multiple Sclerosis and Amyotrophic lateral sclerosis wherein overexpression of CB<sub>2</sub>R has been reported [174,175].

Several CB<sub>2</sub>R selective agents and PET tracers have been developed in the past but for some compounds it is not clear whether they are CB<sub>2</sub> agonist, antagonist or inverse agonist [116,119–121,173,176–179]. A detailed overview of previously developed PET tracers for CB<sub>2</sub>R imaging was recently discussed by Spinelli *et al.* [95]. Horti *et al.* developed and evaluated [<sup>11</sup>C]A-836339 (agonist, K<sub>i</sub> hCB<sub>2</sub>=0.64 nM) as a CB<sub>2</sub> specific tracer that was evaluated in an LPS induced neuroinflammation mouse model and in an Alzheimer's disease mouse model (APP<sup>swe</sup>/PS1dE9 mice) [116]. Similarly, Turkman *et al.* developed two [<sup>18</sup>F] labelled 2-oxoquinolines ([<sup>18</sup>F]-14, K<sub>i</sub> hCB<sub>2</sub>=2.8 nM) and examined these in *vitro* receptor binding and *ex vivo* autoradiography studies. However, no *in vivo* data were reported [179]. Moldovan *et al.* developed several CB<sub>2</sub>R PET tracers, and further evaluation was carried out with [<sup>18</sup>F]29, a derivative of A-836339 (agonist, K<sub>i</sub> hCB<sub>2</sub>=4 nM) which showed specific binding in the brain with LPS induced neuroinflammation in mouse models. However, rapid tracer metabolism limited further evaluation [173]. More recently, [<sup>11</sup>C]RS-016 (K<sub>i</sub> hCB<sub>2</sub>=0.7 nM) emerged as specific PET tracer for detection of atherosclerosis plaques. However it was unsuccessful in distinguishing stable from vulnerable plaques [118]. Our group has previously reported [<sup>11</sup>C]NE40 (inverse agonist, K<sub>i</sub> hCB<sub>2</sub>=9.6 nM) (Figure 1) as a specific CB<sub>2</sub>R PET tracer. Uptake of [<sup>11</sup>C]NE40 was observed in the spleen of rodents, organs with known CB<sub>2</sub> rich expression and in a rat model with local overexpression of hCB<sub>2</sub>R in the brain [120,121]. [<sup>11</sup>C]NE40 was further evaluated for its safety and tolerability in healthy human male subjects in biodistribution and dosimetry studies [122].

In 2016, we reported the synthesis, *in vivo* biodistribution and *in vitro* binding affinity data of two brain penetrant, high-affinity CB<sub>2</sub>R agonist PET tracers [<sup>11</sup>C]MA2 and [<sup>18</sup>F]MA3, Figure 1 [180]. MA3 has an almost 100-times higher affinity for hCB<sub>2</sub> (agonist, K<sub>i</sub> hCB<sub>2</sub>=0.8 nM) compared to MA2 (agonist, K<sub>i</sub> hCB<sub>2</sub>= 87 nM).

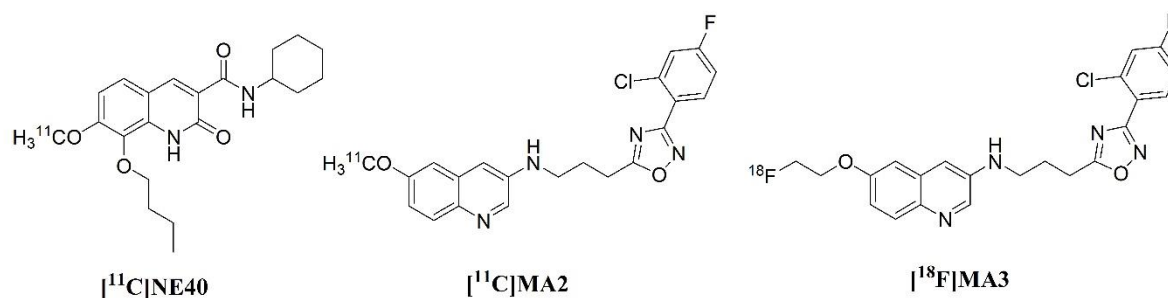


Figure 1. Chemical structures of  $[^{11}\text{C}]\text{NE40}$ ,  $[^{11}\text{C}]\text{MA2}$  and  $[^{18}\text{F}]\text{MA3}$ , PET radiotracers for *in vivo*  $\text{CB}_2\text{R}$  imaging.

Agonists only bind to the active state of  $\text{CB}_2\text{R}$  [181], whereas inverse agonists like NE40 bind to both active and inactive states. PET imaging with an agonist thus would provide quantification of the active state fraction of  $\text{CB}_2\text{R}$  which may be more relevant to study the role of  $\text{CB}_2\text{R}$  in various pathologies. MA3 is an agonist that has proven brain exposure and hence can be used in pharmacological experiments aiming for the activation of  $\text{CB}_2\text{R}$  *in vivo*. In this study, we further focused on  $[^{18}\text{F}]\text{MA3}$  and evaluated its potential as a specific  $\text{CB}_2\text{R}$  tracer. We conducted PET imaging in a rat model with local overexpression of *hCB}\_2\text{R}* combined with *ex vivo* autoradiography. In the same animal model, we compared the binding potential ( $\text{BP}_{\text{ND}}$ ) with that of  $[^{11}\text{C}]\text{NE40}$  and finally performed a PET study in a rhesus monkey.

## 2. Materials and Methods

### 2.1. General

All the chemicals employed in the (radio)synthesis were purchased from commercial suppliers (Aldrich, TCI Europe or Acros) and used without further purification unless stated. The  $\text{CB}_2$  selective inverse agonist NE40 (8-butoxy-N-cyclohexyl-1,2-dihydro-7-methoxy-2-oxoquinoline-3-carboxamide) was synthesised as per the previous report [120]. The synthesis of the precursor MA1 (3-(3-(3-(2-chloro-4-fluorophenyl)-1,2,4-oxadiazol-5-yl)propylamino)quinolin-6-ol) used for radiosynthesis of  $[^{18}\text{F}]\text{MA3}$ , and the synthesis of the

non-radioactive reference material MA3 (6-(2-fluoroethoxy)-N-(3-(3-(2-chloro-4-fluorophenyl)-1,2,4-oxadiazol-5-yl)propyl)quinolin-3-amine) were described in our previous publication [180].

High performance liquid chromatography (HPLC) was performed using a Shimadzu LC-2010A HT system connected to a UV spectrometer. Radioactivity in the column eluent was monitored using a 3-in NaI(Tl) scintillation detector connected to a single channel analyser (Gabi box, Raytest, Straubenhardt, Germany). Radioactivity in HPLC eluent fractions of samples for radiometabolite analysis was quantified with an automated gamma counter, equipped with a 3-in NaI(Tl) well crystal coupled to a multichannel analyser (Wallac 1480 Wizard, Wallac, Turku, Finland). The results were corrected for background radiation, dead detector time, and physical decay during counting.

All rats have housed in individually ventilated cages in a thermoregulated (22 °C) and humidity controlled environment under a 12h/12h day/night cycle with free access to food and water. The body mass of the rats ranged from 223 to 233 g. All animal experiments were approved by the local Animal Ethics Committee of the University of Leuven and were in accordance with European Ethics Committee guidelines (decree 86/609/EEC). All the animal studies were reported in compliance with the ARRIVE guidelines [182,183]. Here we would like to mention that our experiments are exploratory studies and/or proof-of-principle studies, where we checked the developed tracer meet certain requirements for its clinical suitability. No statistical analysis was performed on the results acquired from our animal experiments due to sample size should not reach minimum n=5 according to ARRIVE guidelines. *In vivo* microPET study performed in three conditions namely baseline, block and displacement study with rats n=3. *Ex vivo* autoradiography study performed in single rat which provided nine brain sections. The non-human primate study (n=1) was performed as a proof-of-concept study to evaluate the brain

kinetics of the developed radiotracer. The vehicle and NE40 used in the studies were blinded to the operator and prepared and numbered by the designer.

### **2.2. Rat model with local *hCB<sub>2</sub>R* overexpression**

The preparation and validation of the rat model with local overexpression of *hCB<sub>2</sub>R* in the brain was described by Vandeputte *et al.* Briefly, four female Wistar rats were stereotactically injected with an adeno-associated viral (AAV) vector serotype 2/7 encoding *hCB<sub>2</sub>* (D80N), in the right striatum (relative to Bregma: anteroposterior 0 mm, lateral -2.8 mm and dorsoventral -5.5 mm to -4.5 mm) under control of a CaMKII promoter. A control AAV2/7 vector expressing the enhanced green fluorescent protein (eGFP) under control of a CaMKII promoter was injected in the left striatum at the contralateral side (anteroposterior 0 mm, lateral 2.8 mm and dorsal -5.5 mm to -4.5 mm) [184]. Each animal was injected with 4  $\mu\text{L}$  vector with comparable vector titers ( $4.8 \text{ E}+12 \text{ GC mL}^{-1}$  and  $5.7 \text{ E}+12 \text{ GC mL}^{-1}$  respectively).

### **2.3. In vivo PET study in a rat model with local *hCB<sub>2</sub>R* overexpression**

PET imaging experiments were performed on a Focus<sup>TM</sup> 220 PET scanner (Concorde Microsystems, Knoxville, TN) using three rats with local overexpression of *hCB<sub>2</sub>R*. The first scan was performed with [<sup>18</sup>F]MA3, 11 weeks after the surgery, rat n°1 was scanned baseline, rat n°2 was scanned after pre-treatment (block) and rat n°3 was scanned in a displacement study. In the second scan 12 weeks after surgery, rat n°1 was scanned after blocking, rat n°2 in displacement, and rat n°3 for a baseline. Finally in the last scan 14 weeks after surgery, rat n°1 was scanned in a displacement, rat n°2 for baseline, and rat n°3 after blocking. Using this protocol, each rat served as its own control.

During PET imaging, animals were kept under gas anaesthesia (2.5% isoflurane in O<sub>2</sub> at 1 L min<sup>-1</sup> flow rate). Upon intravenous (*i.v.*) injection with about 30 MBq tracer, a 90-min

([<sup>11</sup>C]NE40) or 120-min ([<sup>18</sup>F]MA3) dynamic PET scan was started. All scans were acquired in list mode. Acquisition data were Fourier rebinned in 24 time frames (4 x 15 s, 4 x 60 s, 5 x 180 s, 8 x 300 s, 3 x 600 s) for 90-min acquisitions and 27 time frames (4 x 15 s, 4 x 60 s, 5 x 180 s, 8 x 300 s, 6 x 600 s) for 120-min acquisitions and reconstructed using maximum a posteriori iterative reconstruction. A summed image of the reconstructed data was spatially normalised to an in-house created <sup>18</sup>F-FDG template of the rat brain in Paxinos coordinates [169] using an affine transformation. The latter was then used to normalise all time frames of the dynamic PET data set to allow automated and bilateral volumes of interest (VOIs) analyses. Time-activity curves (TACs) were generated using PMOD software (v 3.2, PMOD Technologies, Zürich, Switzerland).

The rats in the baseline (only tracer injection) and pre-treatment study were anaesthetised with 2.5% isoflurane in O<sub>2</sub> at 1 L min<sup>-1</sup> flow rate and injected intraperitoneally (*i.p.*) with vehicle (see below) or NE40 (1 mg kg<sup>-1</sup>) 30 min before tracer injection, respectively. For the displacement study, NE40 (1 mg kg<sup>-1</sup>) was administered *i.v.* 20 min after tracer injection. NE40 was dissolved in a vehicle containing 20% dimethylsulfoxide (DMSO), 40% 2-hydroxypropyl  $\beta$ -cyclodextrin and 5% tween 80 in water for injection at a concentration of 1 mg mL<sup>-1</sup>. Binding potential (BP<sub>ND</sub>) was calculated using simplified reference tissue model (SRTM) and the left striatum as a reference region.

#### ***2.4. Ex vivo autoradiography in a rat model with local hCB<sub>2</sub>R overexpression***

A rat with local overexpression of hCB<sub>2</sub>R (n=1) was injected *via* the tail vein with about 48 MBq [<sup>18</sup>F]MA3 under anaesthesia (2.5% isoflurane in O<sub>2</sub> at 1 L min<sup>-1</sup> flow rate). The rat was sacrificed by decapitation 30 min after tracer administration. The brain was removed, rapidly frozen in 2-methylbutane cooled to -40 °C. Transversal sections (20  $\mu$ m) from the brain were obtained using a cryotome (n=9) and were exposed to a high-performance phosphor storage

screen for 1h (Super resolution screen; Perkin Elmer, Waltham, USA). The screens were read using a Cyclone Plus system (Perkin Elmer), and data were analysed using Optiquant software (Perkin Elmer).

### ***2.5. In vivo PET study in a non-human primate***

Dynamic 120 min [ $^{18}\text{F}$ ]MA3 PET brain scans were acquired with a Focus<sup>TM</sup> 220 PET scanner in a female rhesus monkey (*Macaca mulatta*, 5.2 kg). Sedation was performed by intramuscular (*i.m.*) injection of a combination of 0.3 mL Rompun (xylazine 2% solution) and 0.35 mL Nimatek (ketamine 100 mg mL<sup>-1</sup>). About 60 min after the first injection, the monkey received an additional dose of 0.15 mL Rompun and 0.175 mL Nimatek *via i.v.* injection. During the last part of the scan, dosing was done less frequently based on the heartbeat frequency. The O<sub>2</sub> and CO<sub>2</sub> saturation in the blood and the heartbeat were constantly monitored. The body temperature was regulated *via* a heating pad. The breathing frequency and the eye response were checked visually. The head of the animal was placed centrally in the field of view of the PET scanner. The monkey was injected with about 170 MBq of [ $^{18}\text{F}$ ]MA3 *via* the vena saphena. Scans were acquired in list mode and Fourier rebinned in 27-time frames (4 x 15 s, 4 x 60 s, 5 x 180 s, 8 x 300 s, 6 x 600 s). Data were reconstructed using a 3D maximum a posteriori (3D-MAP) iterative reconstruction. TACs of the whole brain and several brain regions were generated using VOIs with PMOD software, and radioactivity concentration in the brain was expressed as standardized uptake value (SUV) as a function of time after tracer injection. For the pre-treatment study, NE40 was dissolved in a vehicle containing 20% DMSO and 40% 2-hydroxypropyl  $\beta$ -cyclodextrin in water for injection. Pre-treatment was done by *i.v.* injection of NE40 at a dose of 1 mg kg<sup>-1</sup> 10 min before tracer injection.



### ***2.6. Non-human primate plasma radiometabolite analysis***

During the baseline and pre-treatment scan, blood samples were collected at 10, 30 and 60 min post tracer injection (p.i.) *via* the contralateral vena saphena in EDTA containing tubes (4 mL tubes; BD vacutainer, BD, Franklin Lakes, NJ, USA) and stored on ice. The blood samples were weighed, and activity was counted in the automated gamma-counter. Next, the blood was centrifuged for 10 min at 2330 x g to separate the plasma. About 0.5 mL of plasma was weighed and counted for radioactivity in an automated gamma counter. The plasma was then diluted with an equal volume of acetonitrile and centrifuged for 5 min at 2330 x g to precipitate the proteins. Next, a volume of 0.5 mL of the supernatant was filtered through a 0.22 µm filter (0.2 µm nylon filter, Acrodisc 13, PALL Life Sciences) spiked with 20 µL of authentic non-radioactive compound MA3 (1 mg mL<sup>-1</sup> solution in H<sub>2</sub>O/CH<sub>3</sub>CN 50:50 v/v) and counted for radioactivity in the automated gamma counter. The solution was then injected onto a HPLC system consisting of an analytical XBridge column (C<sub>18</sub>, 3.0 µm, 3 mm × 100 mm, Waters) eluted with a mixture of 0.05 M sodium acetate buffer (pH 5.5) and acetonitrile (55:45 v/v) at a flow rate of 0.6 mL min<sup>-1</sup>. After passing through the UV detector (254 nm) and the 3-inch NaI(Tl) scintillation detector, the HPLC eluate was collected as 1-mL fractions using an automatic fraction collector and the radioactivity in these fractions was measured using an automated gamma-counter.

### ***2.7. Data and Statistical analysis***

The data and statistical analysis comply with the recommendations on experimental design and analysis in pharmacology [185]. Quantitative data are expressed as the mean ± standard deviation (SD). Error bars correspond to SD. Time-activity curve data were generated using PMOD software and data were plotted using GraphPad Prism version 5.00 for Windows,

(GraphPad Software, La Jolla California USA). Chemical structures were drawn using ChemDraw Ultra 8.0.

### **2.8. Nomenclature of targets and ligands**

Key protein targets and ligands in this article are hyperlinked to corresponding entries in the <http://www.guidetopharmacology.org>, the common portal for data from the IUPHAR/BPS Guide to PHARMACOLOGY [186], and are permanently archived in the Concise Guide to PHARMACOLOGY 2017/18 [187].

## **3. Results**

### **3.1. Radiosynthesis of [<sup>11</sup>C]NE40 and [<sup>18</sup>F]MA3**

[<sup>11</sup>C]NE40 synthesis was carried out according to the protocol described in the publication of Evens *et al.* [120]. The radiochemical yield for [<sup>11</sup>C]NE40 was 45% (based on HPLC area under the curve (AUC)) with a radiochemical purity of more than 99% and a molar activity of 30 GBq  $\mu\text{mol}^{-1}$  (n=1) at the end of synthesis (EOS). [<sup>18</sup>F]MA3 was synthesised by alkylation of the phenol precursor using the secondary labelling agent 1-bromo-2-[<sup>18</sup>F]fluoroethane (<sup>18</sup>FEtBr) as described previously [180]. [<sup>18</sup>F]MA3 was produced with a radiochemical yield of 19% (relative to starting activity of <sup>18</sup>FEtBr based on HPLC AUC), a radiochemical purity in the range of 96-99% and a molar activity in the range of 50-240 GBq  $\mu\text{mol}^{-1}$  (n=7) at EOS.

### **3.2. Validation of the developed rat model using [<sup>11</sup>C]NE40**

To validate the *hCB<sub>2</sub>R* local overexpressed rat model, a 90 min baseline dynamic PET scan (n=3) with the previously reported specific CB<sub>2</sub>R PET tracer [<sup>11</sup>C]NE40 was performed. Figure 2 shows a high-intensity signal in the *hCB<sub>2</sub>R* vector-injected right striatum. This was also reflected in the baseline time-activity curves in which accumulation of radioactivity was

observed in the right striatum with faster washout from the left striatum. Uptake in the right striatum (*hCB<sub>2</sub>R* vector) was two-fold higher compared to the left striatum (eGFP control). SRTM  $BP_{ND}$  using the left striatum as a reference region was  $2.1 \pm 0.2$ .

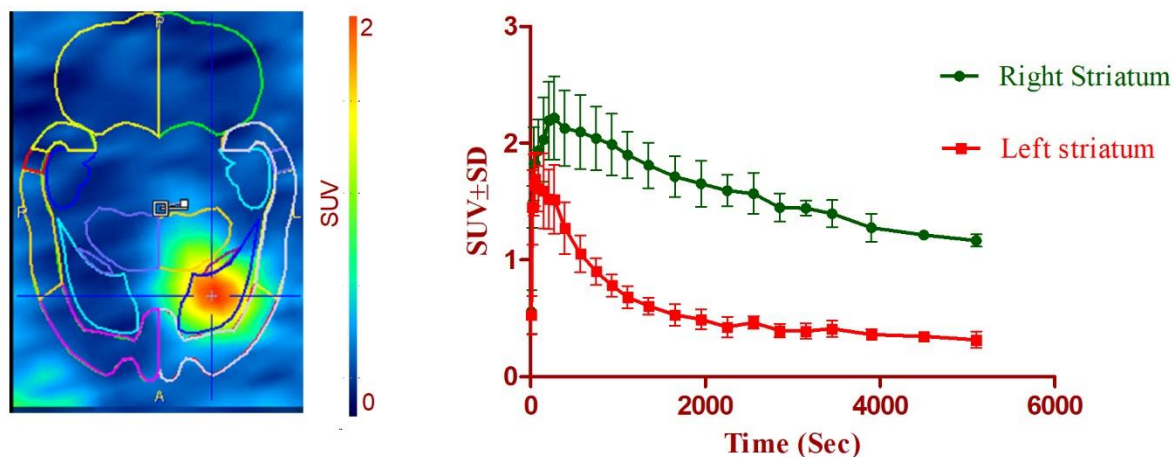


Figure 2. PET study with [ $^{11}\text{C}$ ]NE40 in rat model with local overexpression of *hCB<sub>2</sub>R*. Left: summed images of 0-90 min post tracer injection, Right: corresponding time activity-curves of right and left striatum. Data are expressed as standardized uptake value (SUV). Error bars correspond to SD.

### 3.3. *In vivo* PET study of [ $^{18}\text{F}$ ]MA3 in a rat model with local *hCB<sub>2</sub>R* overexpression

In baseline conditions (Figure 3A;  $n=3$ ) a high-intensity signal was observed in the *hCB<sub>2</sub>R* vector injected right striatum with only background radioactivity in the eGFP control vector injected left striatum. This was also reflected in the baseline time-activity curves in which accumulation of radioactivity was observed in the right striatum with washout from the left striatum. Uptake in the right striatum (*hCB<sub>2</sub>R* vector) was higher compared to the left striatum (control).

Pre-treatment with *i.p.* injection of NE40 ( $1 \text{ mg kg}^{-1}$ ) 30 min before tracer injection resulted in a decrease of the radioactivity concentration in the *hCB<sub>2</sub>R* expressing right striatum Figure 3B ( $n=3$ ). After blocking, no significant difference in tracer binding was observed between right and left striatum. SRTM  $BP_{ND}$  using the left striatum as a reference region was  $2.0 \pm 0.2$ .

Figure 4A (n=3) represents the summed image of 0-20 min of the PET scan before NE40 displacement injection, demonstrating higher tracer binding in the right striatum, with average SUV values (0-20-min) of  $0.7 \pm 0.2$ , comparable with the baseline scans. After *i.v.* injection of NE40 ( $1 \text{ mg kg}^{-1}$ ), 20 min post tracer injection, the time activity curve of the right striatum dropped to the level of the left striatum (average SUV values (20-120-min)  $0.2 \pm 0.0$ ) (Figure 4B).

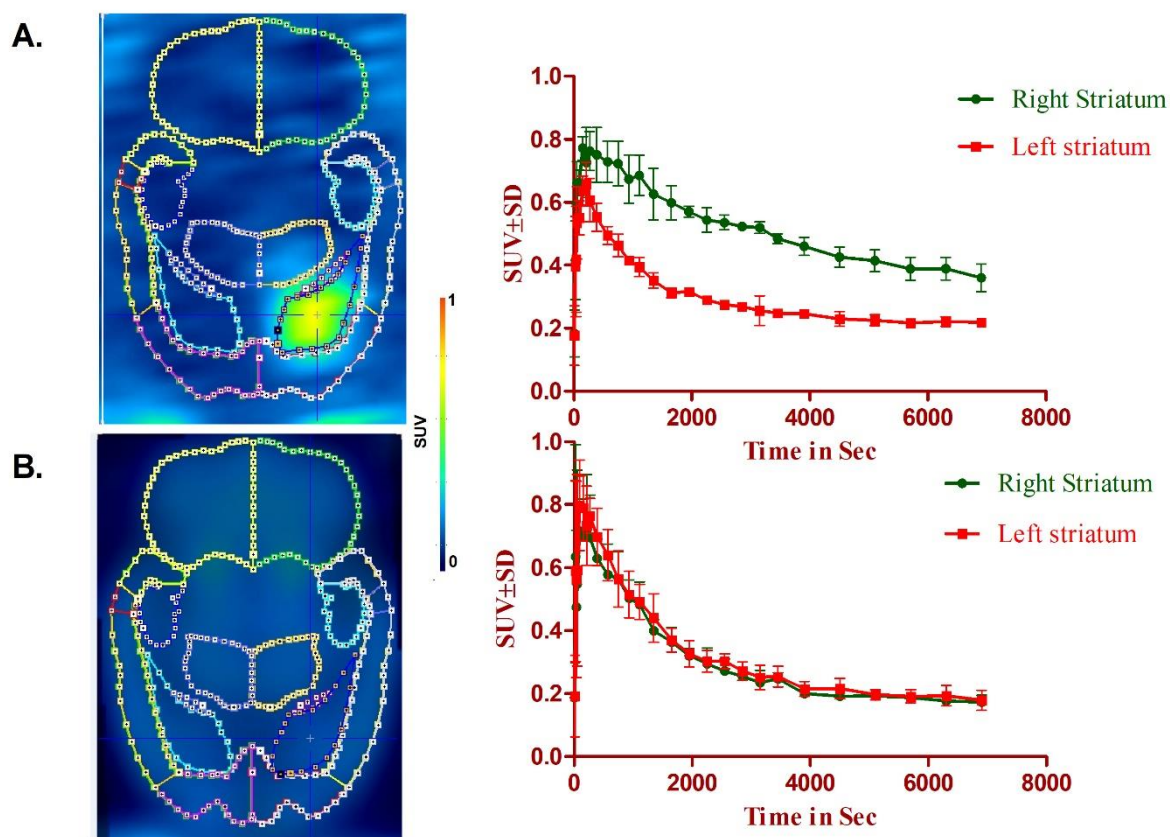


Figure 3. PET data of  $[^{18}\text{F}]\text{MA3}$  in a  $\text{hCB}_2\text{R}$  rat model: right striatum was stereotactically injected with AAV- $\text{hCB}_2\text{R}$ , left striatum was injected with control vector AAV-eGFP. A: Baseline study (n=3): Summed image of 0-120 min post-injection of  $[^{18}\text{F}]\text{MA3}$  with corresponding time-activity curves of right and left striatum. B: Pre-treatment study with NE40 (n=3): Summed image of 0-120 min post-injection of  $[^{18}\text{F}]\text{MA3}$  with corresponding time-activity curves of right and left striatum. NE40 (in the vehicle) was injected *i.p.* at a dose of  $1 \text{ mg kg}^{-1}$  30 min before tracer injection. In the baseline scan, the only vehicle was administered *i.p.* 30 min before tracer injection. Data are expressed as SUV. Error bars correspond to SD.

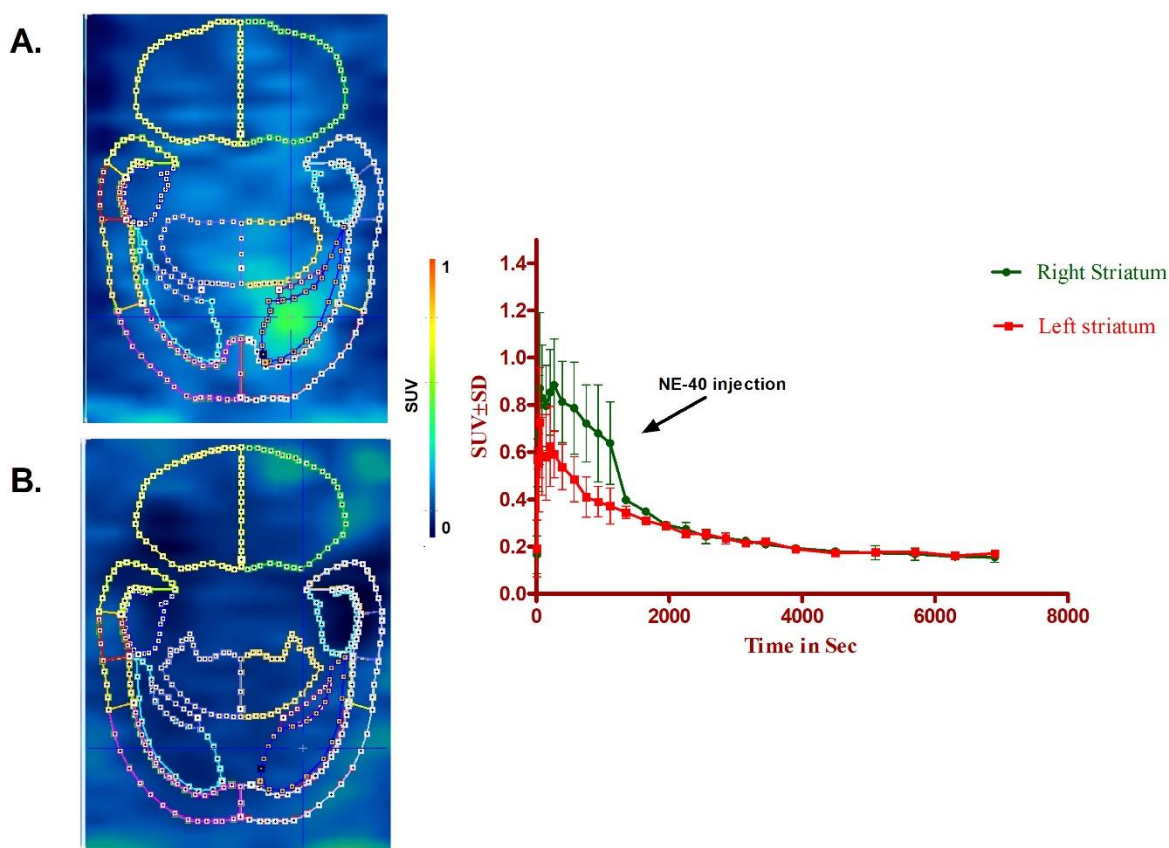


Figure 4: PET data of  $[^{18}\text{F}]\text{MA3}$  displacement study in a  $h\text{CB}_2\text{R}$  rat model: right striatum was stereotactically injected with AAV- $h\text{CB}_2\text{R}$ , left striatum was injected with control vector AAV-eGFP. NE40 at dose  $1 \text{ mg kg}^{-1}$  was injected i.v. (arrow) 20 min after tracer injection. Transversal images corresponding to the chase experiment: summed image (0–20 min after tracer injection) before chase injection (A) and summed image (20–120 min after tracer injection) after chase injection (B), with corresponding time-activity curves of right and left striatum. Data are expressed as SUV. Error bars correspond to SD.

### 3.4. Ex vivo autoradiography of $[^{18}\text{F}]\text{MA3}$ in rat model with local $h\text{CB}_2\text{R}$ overexpression

Figure 5 shows the autoradiogram developed from cryosections of rat brain obtained 30 min after i.v. injection of  $[^{18}\text{F}]\text{MA3}$ . This study confirmed that the radiotracer binds to the  $h\text{CB}_2\text{R}$  viral vector injected site, whereas the binding to the rest of the brain was low. Tracer binding was quantified and expressed as digital light units per square millimetre ( $\text{DLU mm}^{-2}$ ). The ratio of right to left striatum was 2.7.

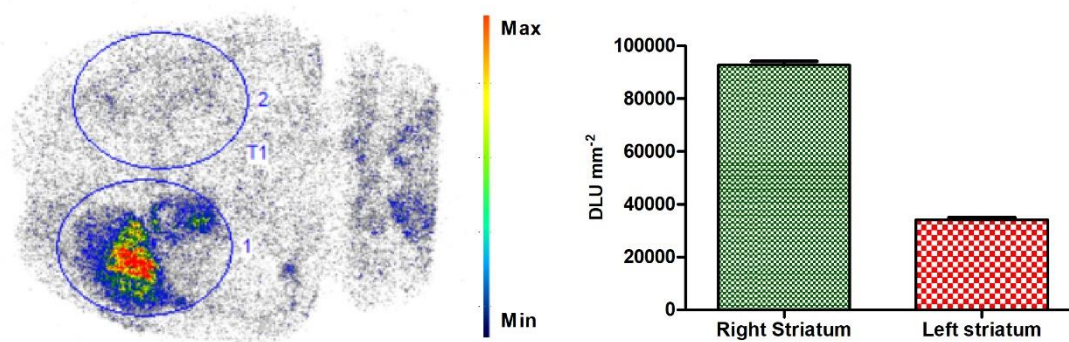


Figure 5. Transversal section of an ex vivo autoradiography study performed in a rat model with local overexpression of hCB<sub>2</sub>R in right striatum (n=1). [<sup>18</sup>F]MA3 was injected i.v. via the tail vein and the rat was sacrificed at 30 min post tracer injection. The autoradiogram shows specific binding of [<sup>18</sup>F]MA3 in the right striatum. Binding is expressed as digital light units per square millimetre (DLU per mm<sup>-2</sup>) of the right and left striatum. Max=maximum; min=minimum.

### 3.5. In vivo PET study of [<sup>18</sup>F]MA3 in a non-human primate

The results of the 120 min baseline and pre-treatment PET scans of [<sup>18</sup>F]MA3 in monkey brain are shown in Figure 6. The TAC of the baseline scan showed a fast initial brain uptake (SUV 1.4 total brain). The uptake was homogeneous throughout the monkey brain (Figure 6A). Regional brain concentration were highest in caudate (average SUV<sub>20-120 min</sub>=0.7±0.1), followed by thalamus (average SUV<sub>20-120 min</sub>=0.6±0.1), hippocampus (average SUV<sub>20-120 min</sub>=0.6±0.1), frontal cortex (average SUV<sub>20-120 min</sub>=0.6±0.1), cerebellum (average SUV<sub>20-120 min</sub>=0.6±0.1) (TACs of different brain regions not shown). After 40 min, the radioactivity concentration in brain reached a steady state (average SUV<sub>20-120 min</sub> 0.6±0.1 total brain). Higher brain uptake (peak SUV 1.8 total brain) was observed after pre-treatment with NE40 (1 mg kg<sup>-1</sup>) for the total duration (0-120 min) of the scan (average SUV<sub>20-120 min</sub> 0.8±0.2 total brain).



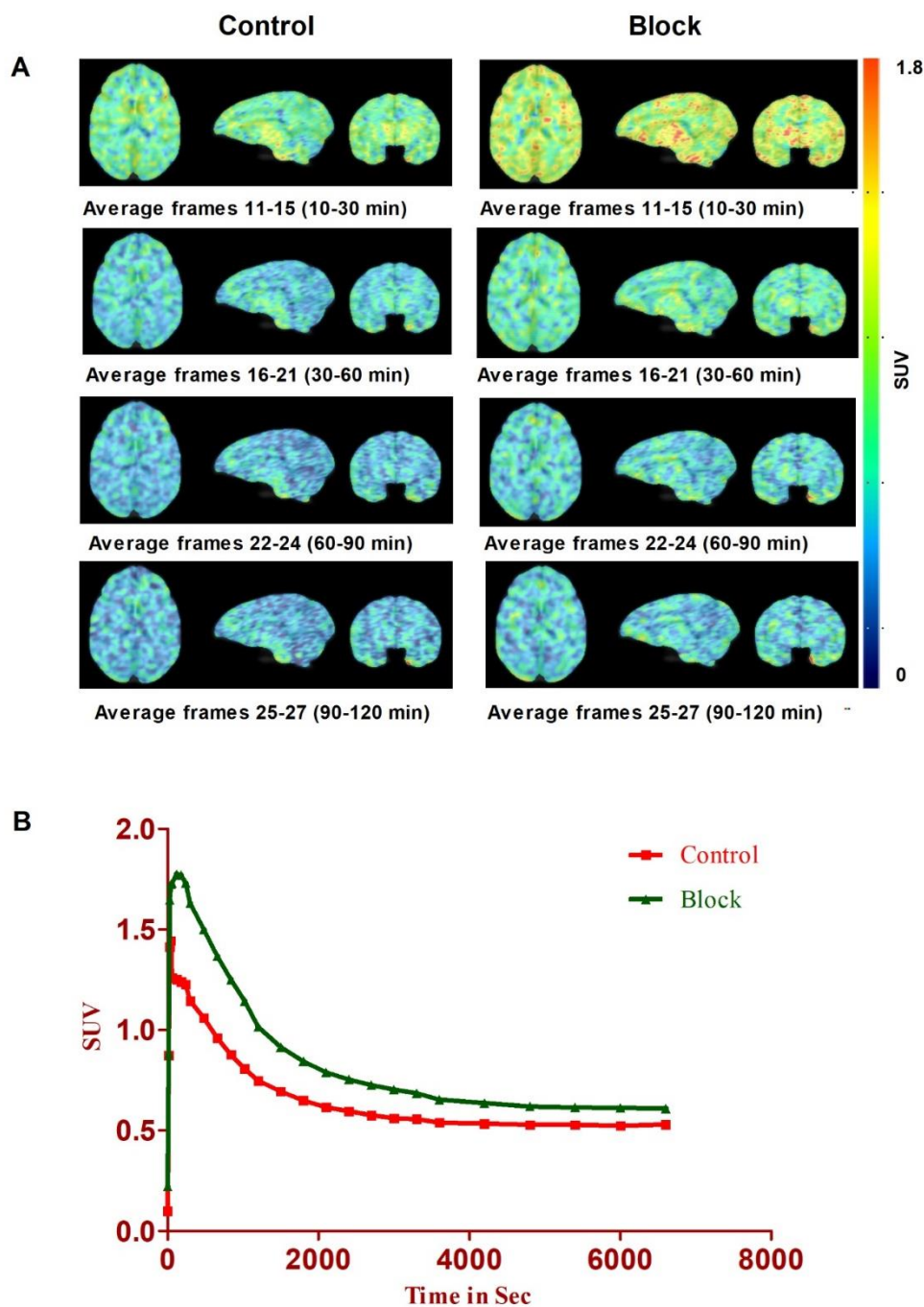


Figure 6. PET data of [ $^{18}\text{F}$ ]MA3 in Rhesus monkey. A: Transversal, sagittal and frontal PET sections of monkey brain. Summed images of 10-30 min, 30-60 min, 60-90 min and 90-120 min after tracer injection for the baseline study (left images) and the pre-treatment study with NE40, 1 mg kg $^{-1}$  i.v. 10 min before tracer injection (right images). B: Corresponding time-activity curves of total monkey brain at baseline (control) and after pre-treatment (block).

### 3.6. Plasma radiometabolite analysis in non-human primate

The reconstructed radiochromatograms of monkey plasma analysis at 10 min, 30 min and 60 min after [ $^{18}\text{F}$ ]MA3 injection showed two peaks (graphs not shown) with the most apolar peak corresponding to the parent tracer. At 10 min post injection of the radiotracer, 16% of the recovered radioactivity in plasma corresponded to intact tracer and this percentage decreased to 12% at 30 min and 7% at 60 min post tracer injection. The percentage of intact tracer in plasma was slightly higher in blocking conditions with 21% at 10 min, 13% at 30 min and 9% at 60 min post tracer injection. The recovery of the HPLC injected radioactivity was in the range of 86-99%. The plasma SUV values of parent [ $^{18}\text{F}$ ]MA3 in baseline and blocking conditions are shown in Figure 7. Brain-to-plasma SUV ratios in baseline conditions were 1.2, 1.2 and 1.9 and after pre-treatment, with NE40 they were 1.4, 1.4 and 1.7 at 10, 30 and 60 min post tracer injection, respectively.

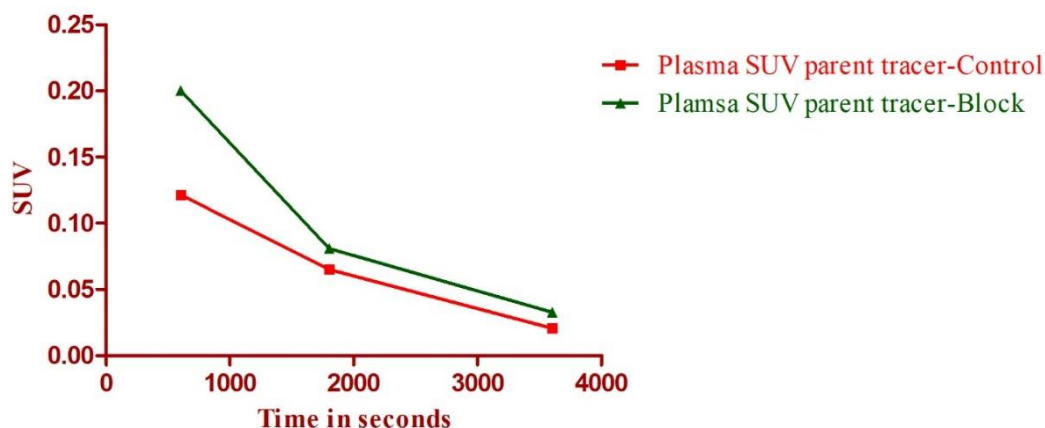


Figure 7. Monkey plasma radiometabolite analysis and quantification of intact tracer in control and block conditions at 10, 30 and 60 min post tracer injection.

## 4. Discussion

In the past, our group reported the synthesis and preclinical evaluation of the inverse agonist tracer [ $^{11}\text{C}$ ]NE40 in a rat model with local overexpression of  $h\text{CB}_2\text{R}$  in the brain. Further,



[<sup>11</sup>C]NE40 was studied in healthy volunteers and currently studies were ongoing in patients with neuroinflammatory conditions. On the other hand [<sup>11</sup>C]NE40 is an inverse agonist which binds to both active and inactive of CB<sub>2</sub>R receptors. Due to its short half-life of carbon-11 isotope 20.3 min, on-site cyclotron is necessary. In the present research report, we developed an CB<sub>2</sub>R agonist PET tracer [<sup>18</sup>F]MA3 that is expected to bind only to the (functionally) active fraction of the CB<sub>2</sub> receptor pool. Due to its longer half-life of (109.7 min) fluorine-18 provides the opportunity to transport the developed radiotracer to nearby PET centres that do not have a cyclotron. We reported earlier on the synthesis and preliminary biological evaluation in mice of two agonist tracers [<sup>11</sup>C]MA2 and [<sup>18</sup>F]MA3 [180]. In the present study, [<sup>18</sup>F]MA3 the CB<sub>2</sub>R agonist tracer with the highest affinity (0.8 nM) for the *h*CB<sub>2</sub>R, was further evaluated *in vivo*.

Validation of the developed rat model using [<sup>11</sup>C]NE40 showed specific binding of the tracer in the right striatum indicating local overexpression of *h*CB<sub>2</sub>R. The results were in line with the previously reported data [121]. [<sup>18</sup>F]MA3 was further extensively studied in the validated rat model. Time–activity curves obtained from the baseline scan showed [<sup>18</sup>F]MA3 binding in the *h*CB<sub>2</sub> vector injected striatum and a fast washout from the contralateral eGFP vector–injected striatum. A two-fold higher radioactivity concentration (SUV) in the right striatum compared to the left striatum was observed ~15 min after injection of the tracer. This was confirmed by *ex vivo* autoradiography where a three-fold higher binding was observed in the right vs left striatum. When comparing the binding potential (BP<sub>ND</sub>) calculated using a simplified reference region model and the left striatum as a reference region, we observed a comparable BP<sub>ND</sub> for both the studied tracers.

The specificity of binding to *h*CB<sub>2</sub>R was proven by blocking experiments with a structurally non-related CB<sub>2</sub>R specific inverse agonist NE40. After pre-treatment, the time-activity curve of [<sup>18</sup>F]MA3 in the right striatum aligned with the TAC of the left striatum. A displacement study with NE40 demonstrated that binding of [<sup>18</sup>F]MA3 to *h*CB<sub>2</sub>R is reversible. Initially,

baseline conditions were observed with higher tracer concentration in the right compared to the left striatum. However, after *i.v.* injection of NE40, the TAC of the right striatum (overexpression of *hCB<sub>2</sub>R*) aligned to the TAC of the left (control) striatum demonstrating fast *in vivo* binding reversibility of [<sup>18</sup>F]MA3.

The CB<sub>2</sub> vs CB<sub>1</sub> selectivity factor is 127 for MA3 and 241 for NE40. The control and blocking studies performed in rats with locally *hCB<sub>2</sub>R* overexpression confirmed binding of [<sup>18</sup>F]MA3 to the viral vector injected striatum, but no specific binding of [<sup>18</sup>F]MA3 was observed in rat cerebellum, hippocampus and globus pallidus that have high CB<sub>1</sub>R expression suggesting that *in vivo* CB<sub>1</sub> specific binding of the tracer in brain is negligible.

Preliminary evaluation of [<sup>18</sup>F]MA3 in a healthy non-human primate showed moderate brain uptake with homogenous distribution and fast washout. Only one polar radiometabolite was detected in monkey plasma which is not expected to enter the brain. No skull uptake was observed in the PET scans in rats and monkey suggesting absence of *in vivo* defluorination of [<sup>18</sup>F]MA3. In contrast to what we expected, pre-treatment with the inverse agonist NE40 (1 mg kg<sup>-1</sup>, *i.v.*) resulted in an increase of radioactivity concentration in monkey brain. This could be explained by the combination of low CB<sub>2</sub>R expression in healthy conditions and a peripheral blocking effect of NE40. NE40 pre-treatment will thus result in a higher tracer concentration in blood and thus more tracer available to enter the brain.

We thus were not able to observe any blocking effect of NE40 pre-treatment in monkey brain. CB<sub>2</sub>R expression levels may be too low in healthy conditions so that additional experiments (e.g. by autoradiography) in human brain tissues, in both healthy and disease conditions, is required to evaluate the potential of [<sup>18</sup>F]MA3 as a CB<sub>2</sub>R specific agonist PET tracer. This study also confirms that MA3 is a specific CB<sub>2</sub>R agonist with good brain exposure in rats and

monkeys and is thus suitable for pharmacological experiments where *in vivo* activation of CB<sub>2</sub>R is required.

### **5. Conclusion**

Evaluation of [<sup>18</sup>F]MA3 in a rat model with local striatal overexpression of *h*CB<sub>2</sub>R showed specific and reversible tracer binding in the *h*CB<sub>2</sub> vector injected striatum, indicating that this tracer has potential for *in vivo* imaging of the active state fraction of CB<sub>2</sub> receptors with PET. Lower brain uptake but identical binding potentials were observed for agonist [<sup>18</sup>F]MA3 vs. inverse agonist [<sup>11</sup>C]NE40 in rats. Further evaluation of [<sup>18</sup>F]MA3 in tissue of patients with neuroinflammation is warranted.

### **6. Author Contributions**

B.A., S.C., conducted the radiochemical synthesis and animal experiments. M.A., performed non-radiochemical synthesis. B.A. S.C. and M.K., performed data analysis. C.V.H., prepared and provided the animal model. B.A., S.C., W.V., and G.B., designed the research, made data interpretation and prepared the manuscript. All the authors reviewed the results and approved the final version of the manuscript.

### **7. Acknowledgements**

We thank Julie Cornelis, Ivan Sannen and Pieter Haspeslagh (Laboratory for Radiopharmaceutical Research, KU Leuven) for their help with the animal studies and Christophe Ulens from the Laboratory of Neuro- and Psychophysiology for assisting in the PET monkey studies. This work was supported by IMIR (In Vivo Molecular Imaging Research group) at KU Leuven, and SBO project MIRIAD (Molecular Imaging Research Initiative for Acceleration of Drug Development-130065) funded by IWT Flanders and by the European Union's Seventh Framework Programme (FP7/2007-2013) under grant agreement no.

HEALTH-F2-2011-278850 (INMiND) and Research Foundation Flanders (FWO-Flanders)  
G0007.12; KU Leuven Programme Financing.

**8. *Conflict of interest***

The authors declare no conflicts of interest.

## CHAPTER-IV

### **Synthesis and preclinical evaluation of [<sup>11</sup>C]BA-1 a PET tracer for *in vivo* imaging of CSF-1 receptors**

*Bala Attili<sup>1</sup>, Sofie Celen<sup>1</sup>, Muneer Ahamed<sup>1</sup>, Emilie Billaud<sup>1</sup>, Wim Vanduffel<sup>2</sup>, Michel Koole<sup>3</sup> and Guy Bormans<sup>1\*</sup>*

1. Radiopharmaceutical Research, Department of Pharmaceutical and Pharmacological Sciences, KU Leuven, Leuven, Belgium.

2. Laboratory for Neuro- and Psychophysiology, Department of Neurosciences, KU Leuven, Leuven, Belgium

3. Department of Nuclear Medicine & Molecular Imaging, UZ Gasthuisberg, Leuven, Belgium.

Manuscript under preparation



## ABSTRACT

Proliferation and activation of microglia is a hallmark of several neurodegenerative disorders. This mechanism is controlled by the activation of colony stimulating factor-1 receptors (CSF-1R). CSF-1R and its ligands were found to have several roles in neuroinflammation, various types of cancers and rheumatoid arthritis. Currently, clinical trials are ongoing with several CSF-1R inhibitors. We selected a high affinity ( $IC_{50}$  1 nM) molecule with favourable brain penetration, to be radiolabelled with carbon-11. Radiosynthesis was performed by methylation of an amine precursor to yield [ $^{11}C$ ]BA-1. Preliminary rodent biodistribution and PET studies confirmed high brain penetration of [ $^{11}C$ ]BA-1 with 3% of ID at 2 min post injection and homogenous tracer distribution throughout the mouse brain. In order to examine CSF-1R binding specificity, blocking studies were performed in rodents. An increased brain uptake was observed after blocking indicating peripheral blocking and low CSF-1R expression in healthy conditions. The high non-specific binding and slow washout from brain observed in PET studies could be due to lysosomal trapping of [ $^{11}C$ ]BA-1. This limits the use of [ $^{11}C$ ]BA-1 for brain CSF-1R imaging. This tracer may further evaluated in animal models for rheumatoid arthritis and various cancers.

**Key words:** CSF-1R, biodistribution, microPET, neuroinflammation

### ***1. Introduction***

Colony stimulating factor-1 receptor (CSF-1R), otherwise known as macrophage colony stimulating factor-1 receptor [123] belongs to class III receptor tyrosine kinase sub-family and is encoded by *c-fms* proto-oncogene. CSF-1R cognate endogenous ligands are colony stimulating factor-1 (CSF-1) and interleukin-34 (IL-34) [124,125]. The competitive binding of these ligands to CSF-1R triggers an intrinsic tyrosine specific protein kinase activation, which is vital for diverse biochemical effects [126].

CSF-1R plays an important role in a broad spectrum of pathological conditions including (neuro)inflammation, cancer, and bone diseases [127–130]. High surface expression of CSF-1R was observed on microglia, macrophages, monocytes, dendritic cells and osteoclasts while low levels were found in hematopoietic stem cells (HSC) [128]. Consistent with their expression on microglia and neural lineage, studies performed with CSF1R reporter mice with genetic deletion of CSF-1R in neurons evidenced that this receptor facilitates the critical protection and survival of injured neurons [188]. In resting condition, microglia exert protective, anti-inflammatory and tissue reparative functions in the CNS [14]. However, upon injury or infection, their activation occurs predominantly through the CSF-1-CSF-1R autocrine loop, which results in reactive microgliosis and release of inflammatory cytokines [123,189].

Positron emission tomography (PET) provides a sensitive non-invasive imaging technique to study receptors, enzymes, ion channels and misfolded proteins expressed in healthy and pathological conditions. CSF-1R is involved in various pathologies like neuro(inflammation), glioblastoma and other cancer types, and rheumatoid arthritis [126,128,190]. It would be interesting to visualize the expression of these receptors non-invasively in various pathologies for diagnosis, disease progression and therapy follow-up. Currently, TSPO PET tracers are used in clinical practice for imaging of neuroinflammation but due to polymorphism of the TSPO



gene, its general use for quantification of neuroinflammation is hampered [24]. Several other promising targets like monoamine oxidase-B (MAO-B), cannabinoid type 2 receptor (CB<sub>2</sub>R), cyclooxygenases (COX), histamine-4 receptors (H<sub>4</sub>), adenosine-A<sub>2</sub> receptors (A<sub>2A</sub>R), and the purinoceptor 7 (P2X<sub>7</sub>R) were pursued for imaging of neuroinflammation with PET, but most of them are still at the (pre)clinical stage [14] of development.

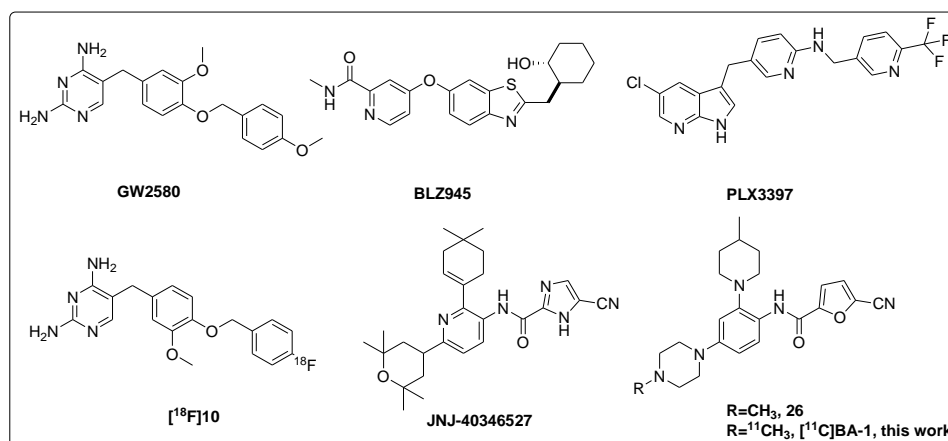


Figure 1: Structures of small molecule CSF-1R antagonists

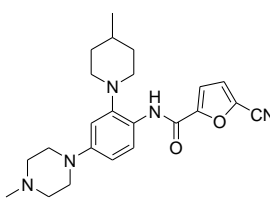
Several classes of small molecule CSF-1R inhibitors have been developed and their characteristics and application have been discussed in a comprehensive review by El Gamal *et al.* [128]. JNJ-40346527 is a cyanoimidazolecarboxamide oral kinase inhibitor with IC<sub>50</sub> value of 3.2 nM and is under phase II clinical trials in patients with rheumatoid arthritis (RA). We choose a cyanofurancarboxamide derivative of JNJ-40346527 (compound **26**, Figure 1) that has a CSF-1R IC<sub>50</sub> value of 1 nM. Compound **26** has a clogD of 2.5 and polar surface area (PSA) of 72 Å<sup>2</sup> which indicates favourable characteristics for passive brain penetration. From radiochemical perspective this molecules can be radiolabelled with carbon-11 on the piperazine methyl group. Bernard-Gauthier *et al.* developed the fluorine-18 labelled derivative of GW2580 (Figure 1) [<sup>18</sup>F]10 as a dual Trk/CSF-1R inhibitor, but its biological evaluation was not (yet) reported [137]. Pyonteck *et al.* described the evaluation of the CSF-1R inhibitor BLZ945 (Figure 1) for inhibition in glioma progression [190]. Pexidartinib (PLX3397) is another widely

studied CSF-1R inhibitor for treatment of glioma [191]. Although several small-molecule antagonists with nanomolar affinity for CSF-1R have been reported [136], there is no specific radiotracer available for visualising CSF-1R with PET. A CSF-1R specific PET probe can be an interesting diagnostic tool as CSF-1R is involved in various pathologies mentioned above and may also be useful in dose-occupancy studies. This report describes the radiosynthesis and preclinical evaluation of a novel PET probe with the aim to visualise CSF-1R *in vivo*.

## 2. Results and Discussion

Compound 26 was assayed using FMS kinase assay and reported to have 1 nM affinity [136]. To passively cross the BBB PET tracers should have a logD value between 1 and 3, and a PSA value of less than  $90 \text{ \AA}^2$  [16]. The selected molecule has a clogD value of 2.5 and a PSA value of  $72 \text{ \AA}^2$  (Table 1).

Table 1: Structure of reference molecule with clogD, polar surface area values and  $IC_{50}$  (\*calculated using Marvin Sketch).

<b>Structure</b>	
<b>Molecular weight</b>	407.2
<b>clogD</b>	2.5*
<b>cPSA</b>	$72.0 \text{ \AA}^2$ *
<b><math>IC_{50}</math> (FMS kinase assay)</b>	1 nM [136]

## 2.1. Chemical and Radiochemical synthesis

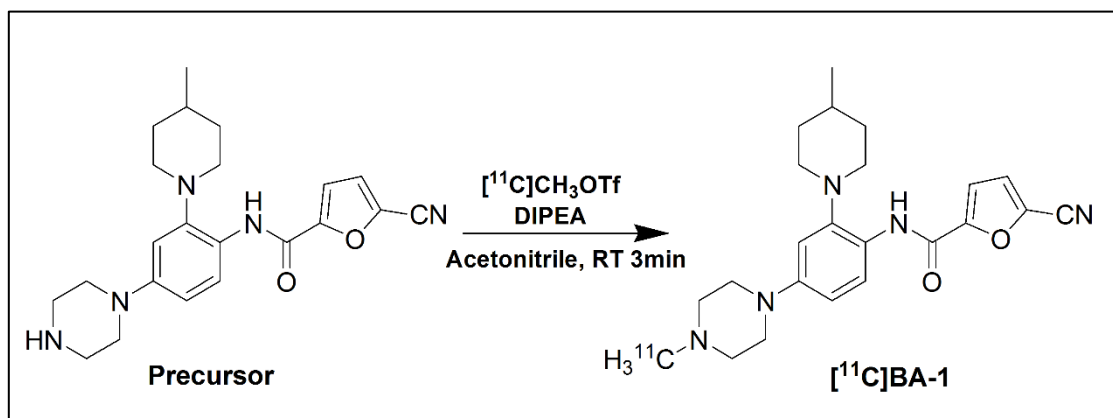


Figure 2: Radiochemical Synthesis of  $[^{11}\text{C}]$ BA-1. Radiolabelling with carbon-11 was achieved by one-step N-alkylation of the amine precursor in anhydrous acetonitrile with  $[^{11}\text{C}]$ methyl trifluoromethanesulfonate ( $[^{11}\text{C}]\text{CH}_3\text{OTf}$ ) in the presence of base (DIPEA) at room temperature (RT) for 3 min.

$[^{11}\text{C}]$ BA-1 was synthesised via methylation of the amine precursor with  $[^{11}\text{C}]$ methyl triflate ( $[^{11}\text{C}]\text{MeOTf}$ ), in the presence of diisopropylethylamine (DIPEA) as a base in acetonitrile (ACN) at room temperature (Figure 2). The crude radiolabelling reaction mixture was purified by preparative RP-HPLC. The methylation yield was 60% (based on the AUC of the radiometric channel of the preparative HPLC) and  $[^{11}\text{C}]$ BA-1 was obtained with a radiochemical purity of more than 98% and average molar activity of 130-240 GBq/ $\mu\text{mol}$  (at the time of evaluation in animals, n=7).

## 2.2. Pre-clinical evaluation of $[^{11}\text{C}]$ BA-1

### 2.2.1. Biodistribution study in mice

Figure 3 represents the % of injected dose (% ID) of  $[^{11}\text{C}]$ BA-1 for various organs and blood at 2, 10, 30 and 60 minutes post tracer injection (n=3/time point). The initial brain uptake (2 min p.i.) amounted 3% of ID in line with the tracer's optimal clogD and PSA values. Brain activity slowly decreased as a function of time to 1.2% at 60 min post injection. 48% of the injected dose was found in liver + intestines at 60 min p.i., which is a typical characteristic of lipophilic

tracer with hepatobiliary excretion. A high initial lung uptake was observed (14% of ID at 2 min p.i.) which gradually decreased to 3% at 60 min p.i.. Urinary excretion of the radiotracer was minimal (2% ID in urine + bladder at 60 min p.i.).

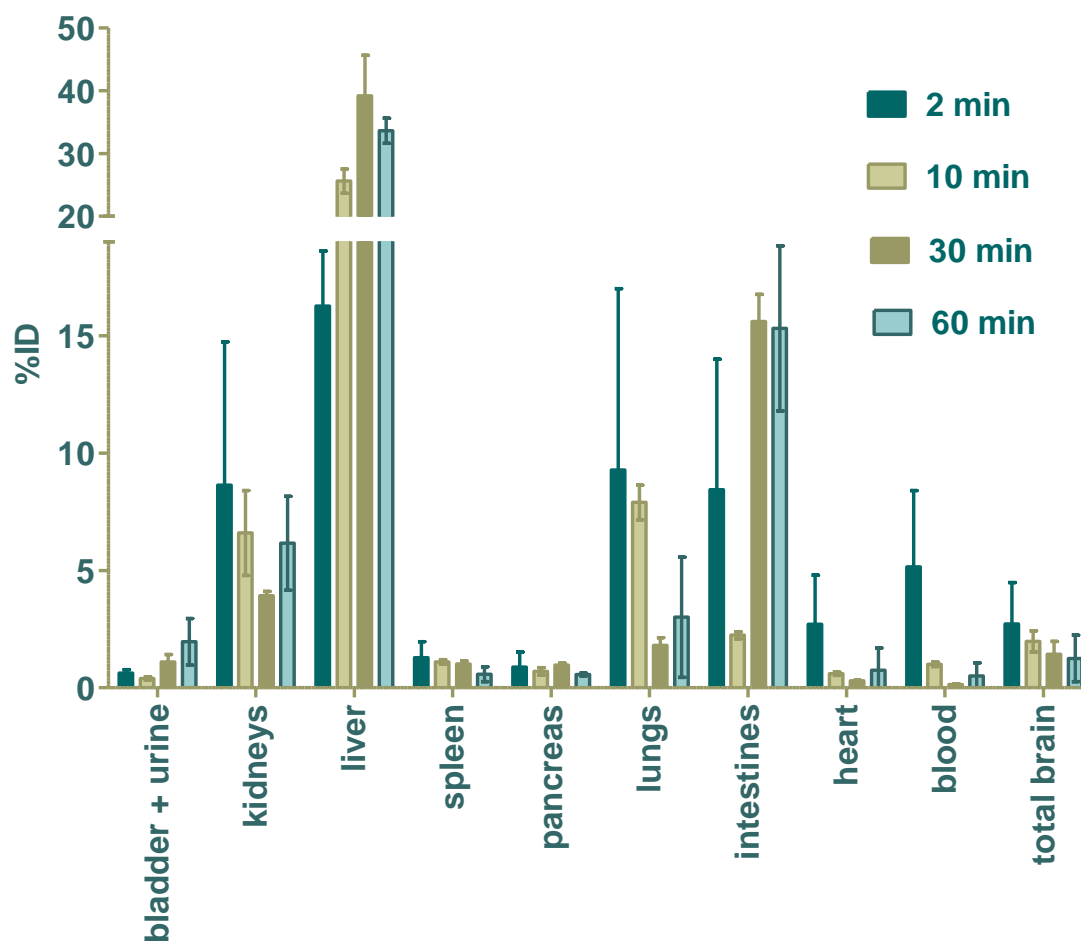


Figure 3: Biodistribution (% ID) of  $[^{11}\text{C}]\text{BA-1}$  in adult NMRI mice at 2, 10, 30 and 60 min post tracer injection. ( $n=3$  / time point).

In order to verify the binding specificity, biodistribution studies were performed at 30 min post tracer injection in mice that were pre-treated with non-radioactive reference ( $n=3$ , 10 mg/kg, *i.p.*) 30 min before injection of the tracer and vehicle treated group ( $n=3$ ) (Figure 4). We observed 41% blocking in the liver, 40% blocking in spleen, 15% blocking in the pancreas and 8% blocking in kidneys. The high blocking in the liver may be due to the abundant expression

of CSF-1R on Kupffer cells [192,193]. This effect could also be explained by saturation of liver transporters and/ or catabolizing enzymes. To validate this result a blocking study with structurally non-related CSF-1R inhibitor is required. No blocking was observed in brain, in contrast we observed an increase in brain uptake upon blocking. This indicates low (if any) CSF-1R specific binding in brain and increase of brain exposure due to peripheral (mainly liver) blocking reducing the rate of tracer's plasma clearance. In line with this hypothesis, the brain-to-blood ratio was comparable (control  $11.7 \pm 3.5$  vs. blocking condition  $11.8 \pm 3.4$ ).

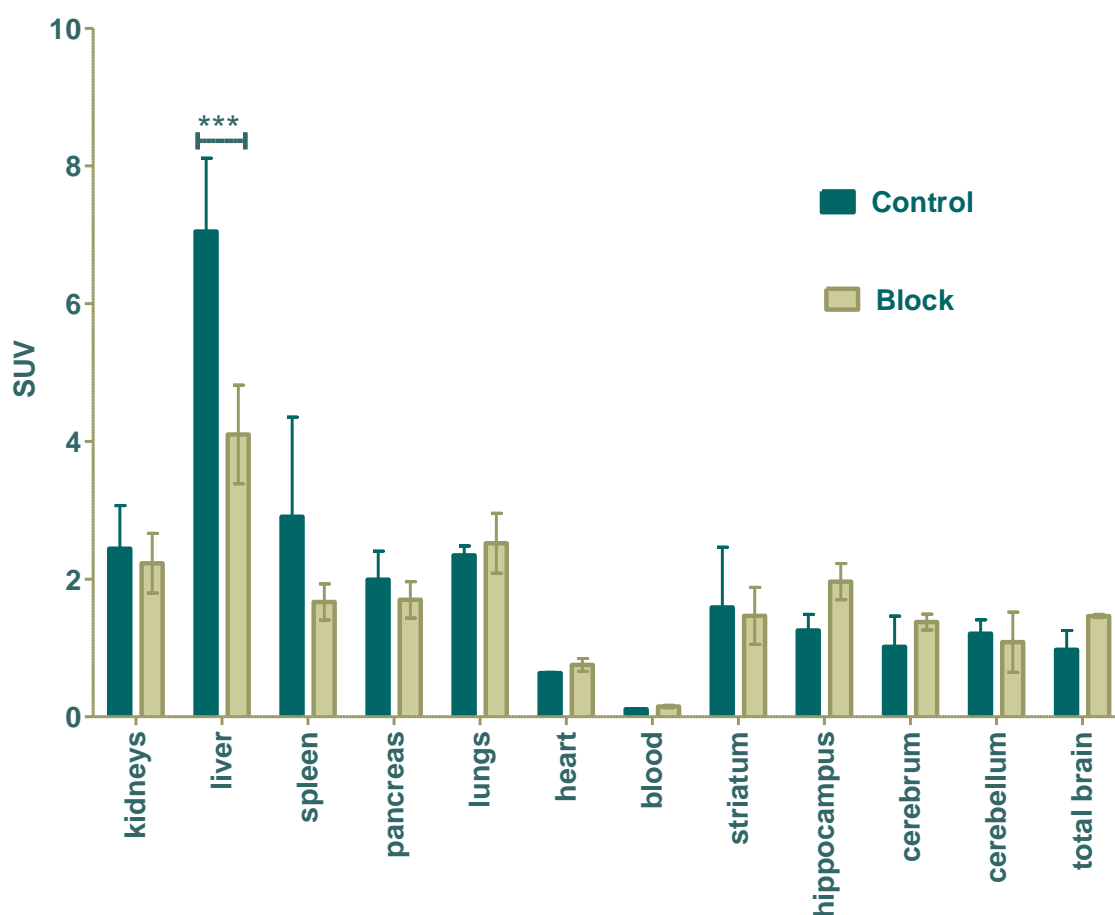


Figure 4: Biodistribution and regional brain distribution of  $[^{11}\text{C}]\text{BA-1}$  in mice at 30 min p.i. in baseline conditions and 30 min, after pre-treatment with non-radioactive reference (10 mg/kg). The concentration in the different organs, brain regions and blood is expressed as SUV values.

2.2.2. *microPET study in rats and non-human primates*

A microPET study performed in rats showed high brain uptake and homogenous distribution throughout the brain with a slow washout similar to what was observed in mice (Figure 3). Self-blocking (5 mg/kg *s.c.*, 30 min prior to tracer injection) did not have a strong impact on the brain time-activity curve (TAC) (Figure 5).

A microPET study in rhesus monkeys (n=2) confirmed high brain uptake (SUVmax 3.4) and slow washout. Blocking with the non-structurally related CSF-1R inhibitor BLZ945 (2 mg/kg *i.v.*, 10 min before tracer injection) had a limited but inconsistent impact on the brain TAC with increase for monkey-1 and decrease for monkey-2 (Figure 5).

Given the high lung uptake observed in mice and the pKa of [<sup>11</sup>C]BA-1 (N-methyl piperazine pKa=7.9) we hypothesise that this tracer undergoes lysosomal trapping which is responsible for the high non-specific binding in brain.

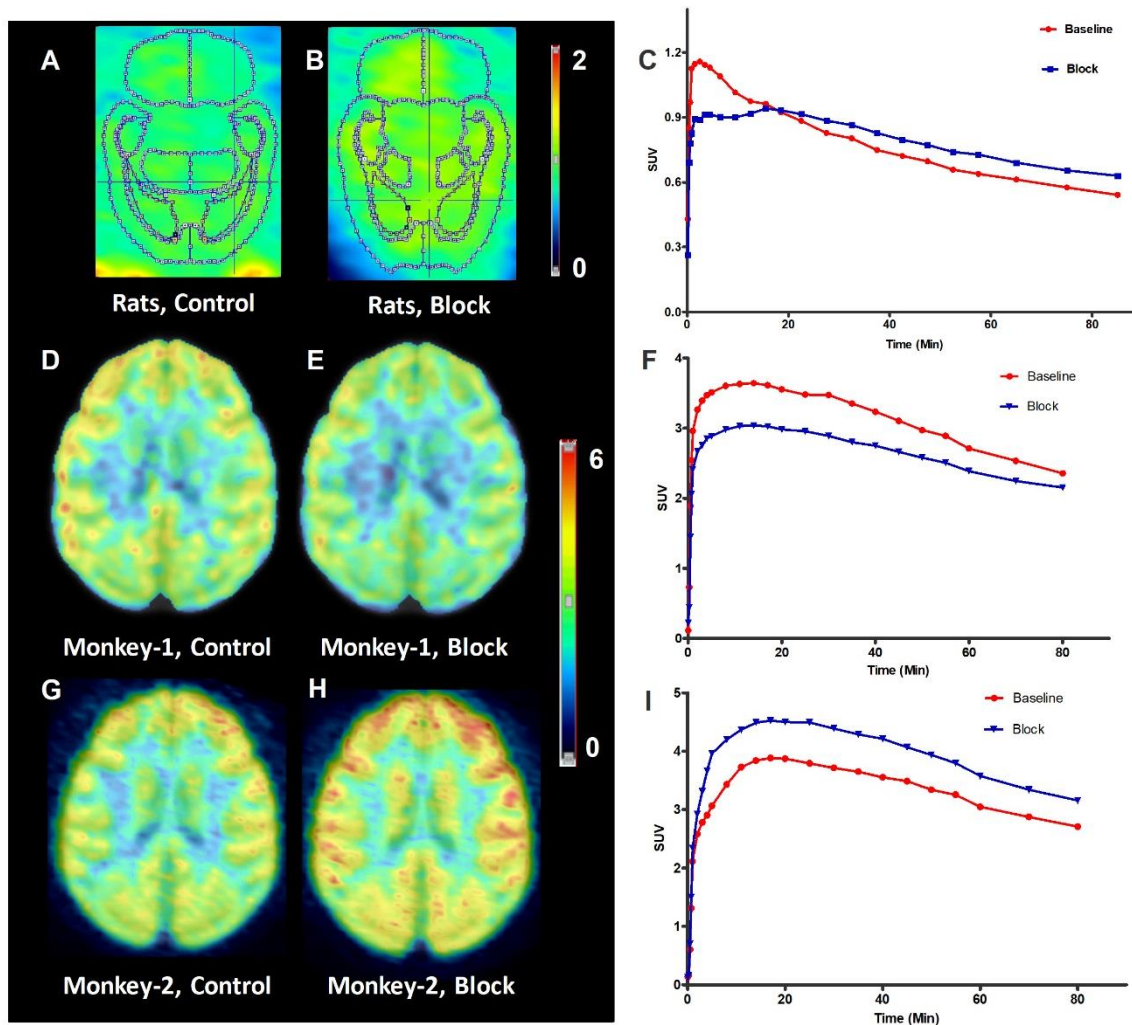


Figure 5:  $\mu$ PET TACs for  $[^{11}\text{C}]\text{BA-1}$  of the rat and monkey brain, A. Average rat brain images (0-90 min), B. Average rat brain images (0-90 min) after blocking with non-radioactive reference (5mg/kg, 30 min before tracer, s.c.), C. Corresponding whole rat brain time activity curves (TACs) during baseline and pre-treatment conditions. D. and G. Average baseline monkey brain images (0-90 min), E. and H. Average monkey brain images (0-90 min) after blocking with BLZ945 (2 mg/kg, 10 min before tracer, i.v.), F. and I. Corresponding monkey brain time activity curves (TACs) during baseline after blocking.

### 2.2.3. Plasma and brain radiometabolite analysis

Plasma samples (10, 30 and 60 min post tracer injection) obtained during the rhesus monkey PET scans in control and blocking conditions. They were analysed using RP-HPLC for radiometabolite quantification. Our data suggest that  $[^{11}\text{C}]\text{BA-1}$  is slowly metabolised *in vivo* with about 50% of parent tracer at 60 min p.i. in baseline conditions. After blocking the fraction of parent dropped to about 37% at 60 min whereas the plasma SUV was comparable between

baseline and blocking. This indicates a similar rate of tracer metabolism but slower clearance of the radiometabolites. The monkey brain-to-blood ratio was quite diverging between both monkeys so that it is difficult to interpret these results based on the small number (n=2) of monkey studies. In addition, the fraction of the apolar metabolite(s) is consistently higher at all studied time points for monkey 2. A perfused brain radiometabolite analysis was performed in rats. Results from this study showed a low amount (< 3%) of polar radiometabolites in brain, 97% parent tracer and no apolar metabolites were observed, indicating that the radiometabolites found in plasma show limited brain uptake. Overall the data show high non-specific binding with limited (if any) CSF-1R specific binding invalidating [<sup>11</sup>C]BA-1 as a PET tracer for quantification of CSF-1R in brain.

*Table 1: Metabolic stability of [<sup>11</sup>C]BA-1 in monkey plasma*

	Monkey-1 plasma (Control)			Monkey-1 plasma (Block)		
	10 min	30 min	60 min	10 min	30 min	60 min
<b>Intact tracer</b>	78.5	62.4	51.9	67.6	45.8	34.2
<b>Polar metabolites</b>	20.6	40.0	43.3	31.7	51.9	65.3
<b>Apolar metabolites</b>	0.9	0.5	4.8	0.6	2.3	0.5
	Monkey-2 plasma (Control)			Monkey-2 plasma (Block)		
	10 min	30 min	60 min	10 min	30 min	60 min
<b>Intact tracer</b>	76.5	65.7	52.2	73.9	60.4	39.4
<b>Polar metabolites</b>	22.8	34.3	44.5	26.0	38.4	53.3
<b>Apolar metabolites</b>	2.1	5.1	7.1	0.8	6.2	10.9



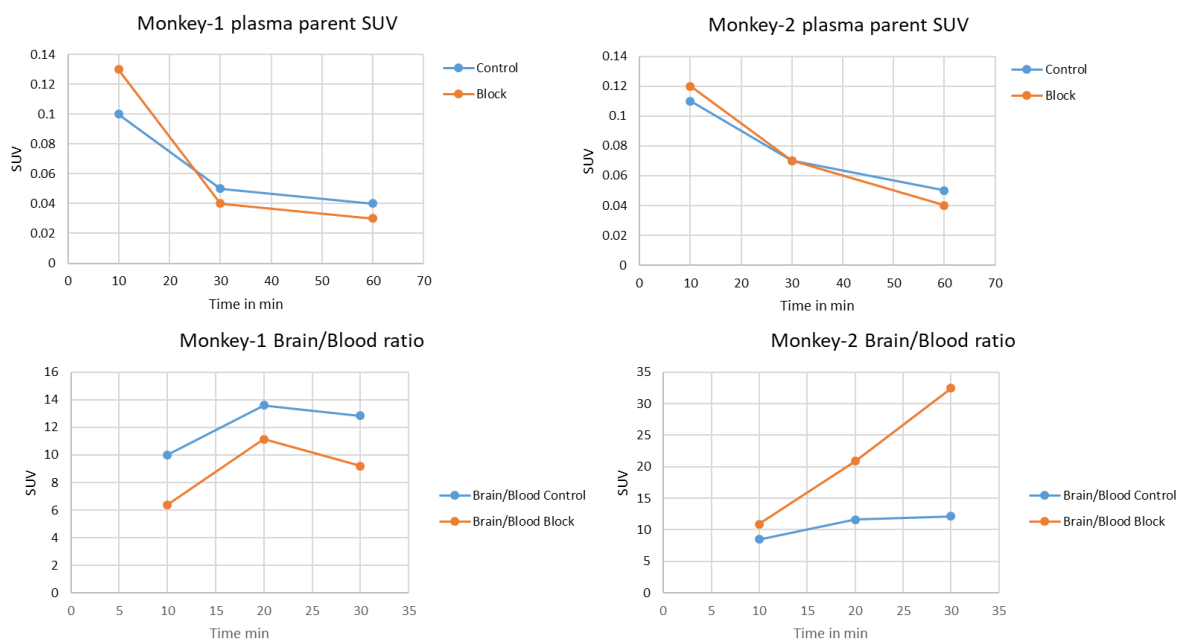


Figure 6: Monkey plasma radiometabolite analysis and quantification of intact tracer in control and block conditions at 10, 30 and 60 min post tracer injection and brain to blood ratio in control and blocking conditions

### 3. Materials and Methods

#### 3.1. General materials and methods

All the chemicals employed in the synthesis were purchased from commercial suppliers (Aldrich, TCI Europe or ACROS) and used without further purification unless otherwise stated.  $^1\text{H}$  and  $^{13}\text{C}$ -Nuclear magnetic resonance (NMR) spectra were obtained on a 300 MHz Bruker NMR spectrometer in deuterated solvents as indicated and with tetramethylsilane, TMS ( $\delta = 0$ ) as an internal standard. Chemical shifts ( $\delta$ ) are reported in ppm, and coupling constants are reported in Hertz. Multiplicity is defined by s (singlet), d (doublet), t (triplet), and m (multiplet). The mass spectra were recorded on a Bruker maXis impact UHR-TOF mass spectrometer coupled to a Dionex 3000RS UHPLC system (Bruker-Daltonik, Bremen, Germany).

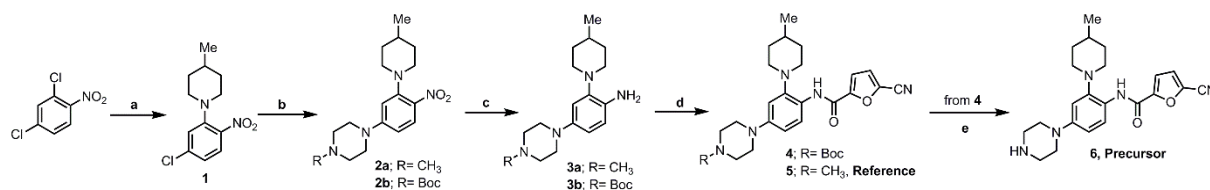
High-performance liquid chromatography (HPLC) was performed using a Shimadzu LC-2010A HT system connected to a UV spectrometer. Radioactivity in the column eluent was

monitored using a 3-in NaI(Tl) scintillation detector connected to a single channel analyser (Gabi box, Raytest, Straubenhardt, Germany). Radioactivity in samples of biodistribution studies and radiometabolite analysis was quantified with an automated gamma counter, equipped with a 3-in NaI(Tl) well crystal coupled to a multichannel analyser (Wallac 1480 Wizard, Wallac, Turku, Finland). The results were corrected for background radiation, detector dead-time and physical decay during counting.

All animals were housed in individually ventilated cages in a thermoregulated (22 °C) and humidity-controlled environment under a 12h/12h day/night cycle with free access to food and water. All animal experiments were approved by the Animal Ethics Committee of the University of Leuven (P104/2016) and are in line with European Ethics Committee guidelines (decree 86/609/EEC)

### 3.2. Synthesis of precursor and reference

Synthesis of reference compound and precursor were based on previously published reports [136].



Scheme 1. Synthesis of compound reference (5) and precursor (6)

Reagents and conditions: a) 4-methyl piperidine, THF, RT, overnight, 83%; b) 1-methylpiperazine or boc-piperazine, DMF, reflux, 120 °C, **2a**, 51%, **2b**, 13%; c) Pd/C (10%), ammonium formate, Ethanol, 2h, 40 °C, **3a**, 90%, **3b**, 90%; d) Cyanofuran carboxylic acid, dry THF, DIPEA, HATU, **4**, 90%, **5**, 89%; e) DCM, TFA, **6**, 64% overnight.

**Reference, 5**

<sup>1</sup>H NMR (CDCl<sub>3</sub>, 300 MHz): δ 1.08 (s, 3H, Me), 1.42-1.82 (m, 3H, CH<sub>2</sub>), 1.87-2.01 (m, 2H, CH<sub>2</sub>), δ 2.43 (s, 3H, Me), 2.61-2.69 (m, 4H, CH<sub>2</sub>), 2.73-2.80 (m, 2H, CH<sub>2</sub>), 2.96-3.00 (m, 2H, CH<sub>2</sub>), 3.18-3.21 (m, 4H, CH<sub>2</sub>), 6.80 (d, 1H, *J* 8.0, Ar), 6.71-6.79 (d, 2H, *J* 15.2, Ar), 6.78 (s, 1H, Ar), 7.20-7.27 (m, 2H, Ar), 8.30 (d, 1H, *J* 11.8, Ar) 9.60 (s, 1H, NH). <sup>13</sup>C NMR (CDCl<sub>3</sub>, 75 MHz): δ 22.1, 30.7, 35.5, 46.2, 49.6, 53.3, 55.2, 109.4, 110.6, 112.4, 114.5, 120.1, 123.5, 125.4, 126.7, 144.0, 148.8, 152.6, 153.3. HRMS (ESI) Calcd. for C<sub>23</sub>H<sub>30</sub>N<sub>5</sub>O<sub>2</sub> (M+H)<sup>+</sup>: 408.2394. Found: 408.2310. HPLC purity: >98%.

**Precursor, 6**

<sup>1</sup>H NMR (CDCl<sub>3</sub>, 300 MHz): δ 1.06 (s, 3H, Me), 1.42-1.82 (m, 3H, CH<sub>2</sub>), 1.87-2.01 (m, 2H, CH<sub>2</sub>), 2.69-2.76 (m, 2H, CH<sub>2</sub>), 2.96-3.05 (m, 2H, CH<sub>2</sub>), 3.27-3.49 (m, 8H, CH<sub>2</sub>), 6.72 (d, 2H, *J* 11.7, Ar), 6.78 (s, 1H, Ar), 7.20-7.28 (m, 2H, Ar), 8.32 (d, 1H, *J* 11.8, Ar) 9.60 (s, 1H, NH). <sup>13</sup>C NMR (CDCl<sub>3</sub>, 75 MHz): δ 22.1, 30.7, 35.5, 44.9, 49.0, 53.3, 110.2, 110.6, 113.5, 114.8, 120.2, 123.5, 126.5, 126.8, 144.1, 148.2, 152.4, 153.5. HRMS (ESI) Calcd. for C<sub>24</sub>H<sub>32</sub>N<sub>5</sub>O<sub>2</sub> (M+H)<sup>+</sup>: 394.2238. Found: 394.2405. HPLC purity: >98%.

**3.3. Radiochemical synthesis**

Radiolabelling was performed by N-alkylation of the precursor in DMF with [<sup>11</sup>C]methyl trifluoromethanesulfonate ([<sup>11</sup>C]CH<sub>3</sub>OTf) in the presence of DIPEA at room temperature for 3 min. After dilution with mobile phase, the reaction mixture was purified by preparative HPLC using an XBridge C<sub>18</sub> column, 5µm, 4.6 mm x 150 mm (Waters, Milford, Connecticut) eluted with a mixture of ACN / Na<sub>2</sub>HPO<sub>4</sub> 10 mM pH 9.3 50/50 v/v with a flow rate of 1.2 ml/min. UV monitoring of the eluate was performed at 254 nm. The peak corresponding to [<sup>11</sup>C]BA-1 was collected, diluted with water and passed through a Sep-Pak C18 Plus light cartridge (Waters,

product number WAT02350, preconditioned with 5 ml of ethanol and 2x5 ml of water). The Sep-Pak was rinsed with 10 ml of water and eluted with 750  $\mu$ l of ethanol into a separate vial and further diluted with saline to obtain a final ethanol concentration of <10% and sterile filtered through a 0.22- $\mu$ m membrane filter (Millex GV 13 mm; Millipore, Billerica, MA). The chemical and radiochemical purity of the tracer was assessed using RP-HPLC on an analytical XBridge C<sub>18</sub> column (3.5  $\mu$ m, 3.0 mm x 100 mm, Waters); eluted with a mixture of ACN / Na<sub>2</sub>HPO<sub>4</sub> 10 mM pH 9.3 50/50 v/v with a flow rate of 0.8 ml/min, and UV detection at 240 nm. The identity of the tracer was confirmed by co-elution with authentic co-injected cold reference compound on the same HPLC system.

### **3.4. Biological Evaluation**

#### **3.4.1. Biodistribution**

Biodistribution studies were carried out in healthy adult NMRI mice (body mass 29 – 50 g) at 2, 10, 30 and 60 min post injection (p.i.) (n = 3 per time point). During the procedure, mice were anaesthetised with 2.5% isoflurane in O<sub>2</sub> at a flow rate of 1 L/min and injected with about 9 MBq of tracer *via* a tail vein. The animals were then sacrificed by decapitation at 2, 10, 30 or 60 min p.i. Blood and major organs were collected in tared tubes and weighed. The radioactivity in blood, organs and other body parts was counted using an automated gamma counter. For calculation of the radioactivity in whole blood, blood mass was assumed to be 7% of the total body mass [168]. Data were expressed as a percentage of injected dose (%ID) and standardised uptake value (SUV). %ID was calculated as (counts per minute (cpm) in organ / total cpm recovered) x 100%. SUV was calculated as (radioactivity in cpm in organ/weight of the organ in gram) / (total cpm recovered/total body weight in gram).

An additional biodistribution study (30 min p.i., n = 3 per time point) was performed 30 min after pre-treatment with non-radioactive reference compound (10 mg/kg) dissolved in a mixture of 10% DMSO, and 20% 2-hydroxypropyl  $\beta$ -cyclodextrin in saline.

#### *3.4.2. Plasma radiometabolite quantification*

During the baseline and pre-treatment scan of non-human primate, blood samples were collected at 10, 30 and 60 min post tracer injection (p.i.) *via* the vena saphena (contralateral to the injection site) in EDTA containing tubes (2 mL tubes; BD vacutainer, BD, Franklin Lakes, NJ, USA) and stored on ice. The blood samples were weighed and activity was counted in the automated gamma-counter. Next, the blood was centrifuged for 5 min at 2330 x g to separate the plasma. About 0.5 mL of plasma was weighed and counted for radioactivity in an automated gamma counter. The plasma was then diluted with an equal volume of acetonitrile to precipitate the proteins and centrifuged for 5 min at 2330 x g. Next, a volume of 0.5 mL of the supernatant was spiked with 20  $\mu$ g of authentic non-radioactive compound (1 mg/mL solution in water / acetonitrile 50:50 v/v) and was filtered through a 0.22  $\mu$ m filter (0.2  $\mu$ m nylon filter, Acrodisc 13, PALL Life Sciences). The filtrate was weighed and counted for radioactivity in the automated gamma counter. The counted plasma extract was then injected onto a HPLC system consisting of an analytical XBridge column (C<sub>18</sub>, 5  $\mu$ M, 3 mm  $\times$  100 mm, Waters) eluted with a mixture of 0.01 M sodium phosphate buffer (pH 9.3) and acetonitrile (50:50 v/v) at a flow rate of 0.5 mL/min and the eluate was monitored with a UV detector (240 nm). The HPLC eluate was collected as 0.5-mL fractions, and radioactivity in the fractions was measured using an automated gamma counter. The recovery of the HPLC injected radioactivity was in the range of 97-104%

### 3.4.3. Rat brain radiometabolite analysis

After *i.v.* administration of about 74 MBq of the radioligand via tail vein under anaesthesia (2.5 % isoflurane in O<sub>2</sub> at 1 L/min flow rate), the rats (n=3) were sacrificed by administering an overdose of Nembutal (CEVA Santé Animale, 200 mg/kg) intraperitoneally at about 5 min prior to the studied time point. When breathing stopped, the rats were perfused by intraventricular injection of saline (Mini Plasco<sup>®</sup>, Braun, Melsungen, Germany) until the liver turned pale. Brain was isolated, and homogenised with a homogenization mixture with 3 mL of CH<sub>3</sub>CN for about 2 min. During mixing the glass tube containing the brain sample is submersed in ice. The brain homogenate was centrifuged (5 min, 2330 x g) and the 1 mL of the supernatant is diluted with an equal volume of water and filtered through a 0.22 µm filter (0.2 µm nylon filter, Acrodisc 13, PALL Life Sciences). About 0.5 mL of the filtrate is spiked with 20 µg of authentic non-radioactive compound (1 mg/mL solution in water / acetonitrile 50:50 v/v) and counted in the gamma counter. The counted brain extract is then injected onto an HPLC system consisting of an analytical XBridge column (C<sub>18</sub>, 5 µM, 3 mm × 100 mm, Waters) eluted with a mixture of 0.01 M sodium phosphate buffer (pH 9.3) and acetonitrile (50:50 v/v) at a flow rate of 0.5 mL/min. The HPLC eluate was collected as 0.5-mL fractions after passing through a UV detector (240 nm), and radioactivity in the fractions was measured using an automated gamma counter. The recovery of the HPLC injected radioactivity was in the range of 84-104%.

### 3.4.4. microPET study in rats and non-human primate rhesus monkey

Dynamic 90-min µPET scans with [<sup>11</sup>C]BA-1 were acquired with a Focus 220 µPET scanner of rats (same protocol used in Chapter III) and a rhesus monkey (n=2) (*Macaca mulatta*, 5.2 kg and 4.5 kg), that was sedated with ketamine (Ketalar<sup>®</sup>) and xylazine (Rompun<sup>®</sup>) *via* intramuscular (*i.m.*) injection. During scanning, the monkeys received repeatedly an additional dose of ketamine/xylazine *via i.v.* injection. O<sub>2</sub> saturation in blood, breathing frequency and

heartbeat frequency were monitored during the entire experiment. The head of the animal was placed central in the field of view of the  $\mu$ PET scanner. Scans were acquired in list mode and Fourier rebinned in 24 time frames (4 x 15 s, 4 x 60 s, 5 x 180 s, 8 x 300 s, 3 x 600 s). Data were reconstructed using a 3D maximum a posteriori (3D-MAP) iterative reconstruction. TACs of the whole brain were generated with PMOD software. Radioactivity concentration in the brain is expressed as SUV as a function of time after tracer injection. Scans were started immediately after *i.v.* injection of about 150 MBq of [ $^{11}\text{C}$ ]BA-1 *via* the vena saphena of the right leg. For the pre-treatment study, BLZ945 (non-structurally related CSF-1R inhibitor) was dissolved in a mixture of 10% DMSO and 40% (2-hydroxypropyl)- $\beta$ -cyclodextrin and filtered through a 0.22- $\mu\text{m}$  membrane filter (Millex-GV, Millipore) prior to injection. Pre-treatment was done by *i.v.* injection of 2 mg/kg of BLZ945 10 min before radiotracer injection and an equal volume of vehicle injection for baseline scans. Blood samples were collected during both baseline and pre-treatment scans at 10, 30 and 60 min p.i. *via* a catheter in the vena saphena of the left leg and plasma was analysed for radiometabolites.

### **3.5. Statistics**

Quantitative data expressed as mean  $\pm$  SD. Means were compared using an unpaired two-tailed student t-test. Values were considered statistically significant for  $P \leq 0.05$ .

### **4. Conclusion**

We successfully synthesised and evaluated a carbon-11 labelled radiotracer for CSF-1R visualisation. Preliminary evaluation in mice, rats and monkeys confirmed high brain uptake but high non-specific binding was observed probably due to lysosomal trapping whereas no CSF-1R specific binding was observed. This invalidates [ $^{11}\text{C}$ ]BA-1 for visualization of brain CSF-1R. Thus, other derivatives with high affinity and better suited pKa values to prevent

lysosomal trapping need to be developed. Further experiments are required to evaluate [<sup>11</sup>C]BA-1 for visualisation of CSF-1R in tumours and RA.

### ***5. Acknowledgements***

This project was funded by the European Union's Seventh Framework Programme under grant agreement no. HEALTH-F2-2011-278850 (INMiND). We would like to thank Julie Cornelis (Radiopharmaceutical Research) to help with the mice and rat animal studies. Christophe Ulens (Laboratory of Neuro-and Psychophysiology) for providing the Macaque monkey and assisting in the monkey studies.



## CHAPTER-V

### **Synthesis and preclinical evaluation of [<sup>11</sup>C]G1055611 a novel GPR84 PET ligand for visualisation of neuroinflammation**

*Bala Attili<sup>1</sup>, Bryan Holvoet<sup>2</sup>, Frederic Labeguere<sup>2</sup>, Pieter Claes<sup>3</sup>, Kenji Shoji<sup>2</sup>, Xavier Bock<sup>2</sup>, Johan Beetens<sup>3</sup>, Romain Gosmini<sup>2</sup>, Steve De Vos<sup>3</sup>, Guy Bormans<sup>1</sup>*

1. Radiopharmaceutical Research, Department of Pharmaceutical and Pharmacological Sciences, KU Leuven, Belgium.
2. Galapagos SASU, 102 Avenue Gaston Roussel, 93230 Romainville, France
3. Galapagos NV, Generaal De Wittelaan L11 A3, 2800, Mechelen, Belgium

Manuscript under preparation



## ABSTRACT

The G-protein coupled receptor (GPR84) which is activated by medium chain fatty acids and is expressed on immune cells suggesting a role of GPR84 in immunological functions. GPR84 upregulation upon lipopolysaccharide stimulation confirmed that it has a role in proinflammatory functions in the central nervous system. We synthesised a high affinity antagonist radiotracer [ $^{11}\text{C}$ ]G1055611 with good radiochemical yields and high radiochemical purity for *in vivo* imaging of GPR84. *In vitro* evaluation of [ $^{11}\text{C}$ ]G1055611 in GPR84 transduced cells confirmed high tracer binding and blocking after incubation with the GPR84 antagonist GLPG1205. LPS treatment of the cells increased tracer binding. An *in vitro* autoradiography study on mouse brain sections showed homogenous tracer binding that was blocked by 45 % in the presence of GLPG1205. *In vivo* evaluation in mice confirmed good brain uptake of the tracer. *In vivo* blocking studies showed blocking in kidney and increase in brain uptake. Upon LPS pre-treatment, an increase in tracer binding in mice brains was observed.

Key words: PET, GPR84, [ $^{11}\text{C}$ ]G611, biodistribution, cell binding

### ***1. Introduction***

GPR84 belongs to the orphan receptor of the rhodopsin superfamily and is a member of the free fatty acid (FFA) sensing G-protein coupled receptors (GPCRs) [138–140]. It has been reported that medium chain fatty acids (MCFAs) with carbon chain length of 9-12 can activate GPR84 [141,142]. However no specific endogenous ligand for GPR84 was identified so far, and the physiological functions of GPR84 are largely unknown [194].

GPR84 is predominantly expressed on myeloid cells (e.g., monocytes, macrophages, microglia, and neutrophils), suggesting a role of GPR84 in immunological functions [142,143]. In the central nervous system several transcriptome analyses confirmed GPR84 expression on microglia [144,145]. mRNA expression analysis has revealed the abundant expression of GPR84 in bone marrow, lung, spleen and leucocytes [195]. Furthermore, Venkataraman and Kuo have identified a role of GPR84 in T-cell mediated IL-4 production [196].

The primary immune cells of the central nervous system are microglia and they are of myeloid-monocytic origin [197]. These cells are known to play both detrimental and beneficial roles in many neurodegenerative disorder such as multiple sclerosis, Alzheimer's disease, Parkinson's disease [198]. Unfortunately, at this time there is no way to orchestrate these cells for therapeutic purposes [139].

GPR84 is highly upregulated under various inflammatory conditions such as endotoxemia and experimental autoimmune encephalomyelitis (EAE) indicating a direct correlation of GPR84 upregulation with neuroinflammatory conditions [139,146]. Importantly, GPR84 was also found to play a crucial role in experimentally induced neuropathic pain [147].

Non-invasive imaging of GPR84 receptors with PET potentially allows to study microglial activation, a key step in the neuroinflammatory cascade. Currently, there are no specific

antibodies available to study GPR84 expression, therefore it might be interesting to have a radiotracer for *in vivo* visualisation of the GPR84 expression in healthy and various pathological conditions. Herein, we describe the development, *in vitro* and *in vivo* evaluation of a novel radiotracer [ $^{11}\text{C}$ ]G611 for targeting GPR84.

## 2. Results and Discussion

### 2.1. *In vitro* evaluation

The [ $^{35}\text{S}$ ]GTP $\gamma$ S assay performed, an  $\text{IC}_{50}$  of 41 nM for G611 was found. In the similar assay conditions, GLPG1205 (GPR84 antagonist, under clinical trials) showed an  $\text{IC}_{50}$  of 67 nM.

### 2.2. Radiochemistry

The radiolabelled [ $^{11}\text{C}$ ]G611 was obtained by alkylation of the phenol precursor with [ $^{11}\text{C}$ ]methyl iodide at 70 °C in DMF in the presence of base ( $\text{K}_2\text{CO}_3$ ) for 3 min (Figure 1). The crude radiolabelling reaction mixture was purified by preparative RP-HPLC. The methylation yield was 80% (based on the AUC of radiometric channel of the preparative HPLC). [ $^{11}\text{C}$ ]G611 was obtained with a radiochemical purity of  $\geq 99\%$  in a total synthesis time of 50 min. Molar activity is in the range of 40-366 GBq/ $\mu\text{mol}$  at the time of *in vitro* and *in vivo* experiments.

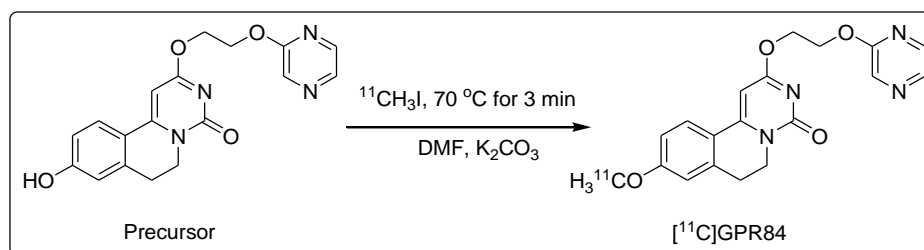


Figure 1: Radiosynthesis of [ $^{11}\text{C}$ ]G611 by reaction of the phenol precursor with [ $^{11}\text{C}$ ] methyl iodide at 70 °C for 3 min in DMF

### 2.3. Cell binding assays

#### 2.3.1. Cell binding experiment with GPR84 transduced cells

The cell binding experiments were performed with GPR84 transduced and control human embryonic kidney cells (HEK-293). The results from the cell binding assay are shown in Figure 2. The study was performed by incubating cells with the tracer in absence or presence of a blocking compound (GLPG1205 50  $\mu$ M) for 10 min and 30 minutes. No difference in tracer binding to GPR84 transduced cells (32% of activity, n=3) between 10 min and 30 min incubation time was observed.

Further, less than 1% uptake was found in control cells for both studied time points. A blocking study with GLPG1205 (a GPR84 antagonist) demonstrated less than 1% of tracer binding on GPR84 transduced cells. Thus, we confirmed that the binding of tracer G611 to GPR84 transduced cells is GPR84-specific.

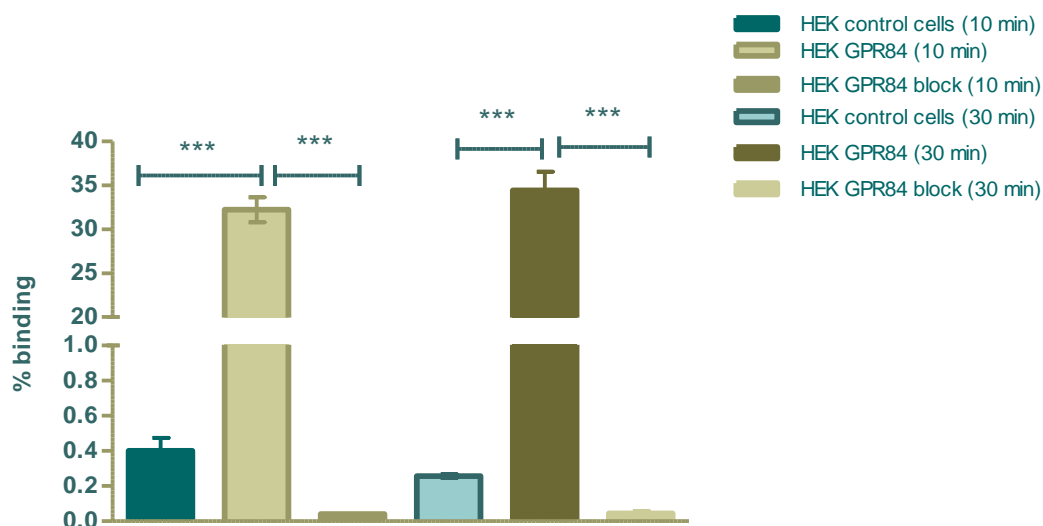


Figure 2: Cell binding experiment with GPR84 transduced HEK-293 cells and control HEK-293 cells, these cells were incubated with tracer or tracer+block (GLPG1205 50  $\mu$ M) incubation for 10 min and incubation for 30 min.

### 2.4.2. Cell binding assay with THP-1 monocytes

Cell binding assays with THP-1 monocytes were performed similar to the cell assay with transduced cells. GPR84 upregulation was achieved by LPS pre-treatment in THP-1 cells. In a radioligand binding assay, a significant difference in tracer uptake was observed between control and LPS treated THP-1 cell lines ( $p=0.00919$ ). We observed 50 % increase in GPR-84 specific binding to LPS treated THP-1 cells (Figure 3).

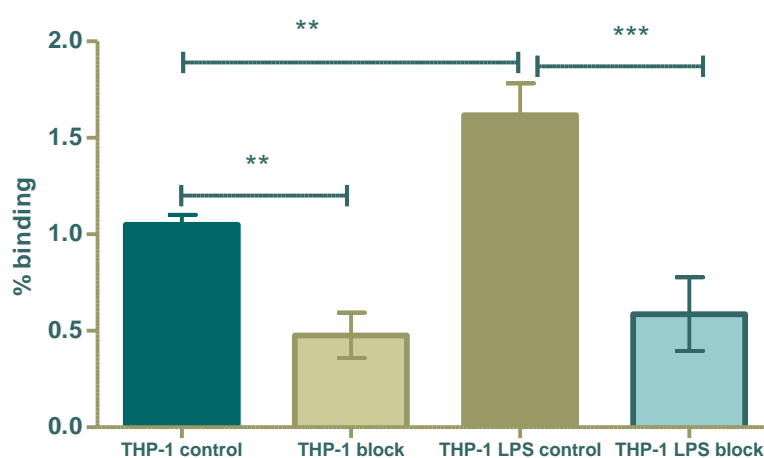


Figure 3: Cell binding experiment with THP-1 cells with or without LPS pre-treatment, cells were incubated with tracer or tracer+block ( $n=3$ ) (GLPG1205 50  $\mu$ M) incubation for 30 min.

### 2.5. In vitro autoradiography

*In vitro* autoradiography experiments were performed on mouse brain sections. The autoradiographs demonstrated a homogenous binding of the tracer in whole mouse brain sections. The binding was blocked (45%) by the presence of GLPG1205 ( $n=3$ ).

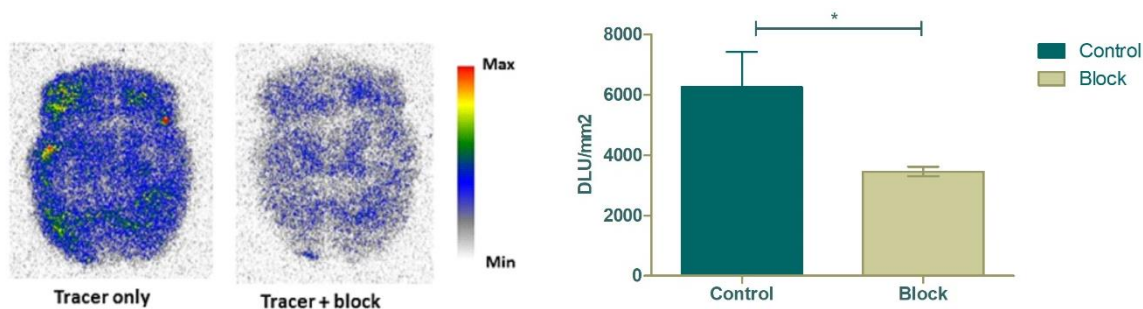
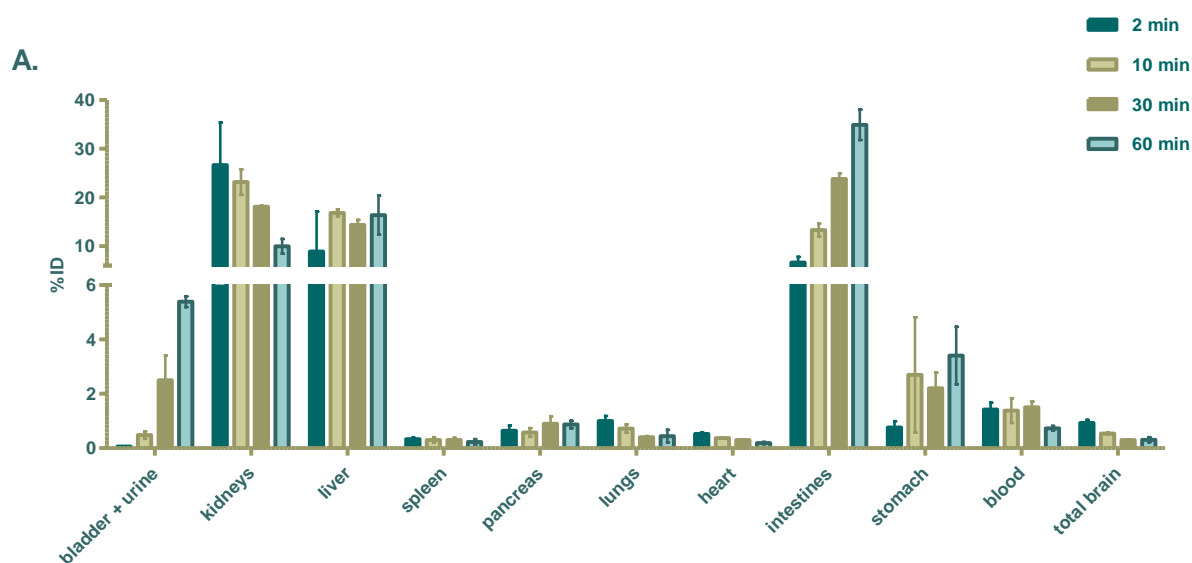


Figure 4: *In vitro* autoradiography experiment with [ $^{11}\text{C}$ ]G611 on mouse brain sections, control and blocking (20  $\mu\text{M}$  GLPG 1205) conditions.

## 2.6. Biodistribution studies

### 2.6.1. Baseline biodistribution study

The results from the biodistribution study shows good brain uptake of [ $^{11}\text{C}$ ]G611 (1% ID at 2 min p.i.) followed by washout as a function of time. The brain distribution was uniform over hippocampus, striatum, cerebrum and cerebellum. Figure 5A shows that the tracer is majorly cleared from plasma via hepatobiliary route with also an important uptake in the kidneys but limited excretion to urine. Blood concentration at 2 min p.i. is low (1.4% ID in total blood) but remains at this level up to 30 min p.i..





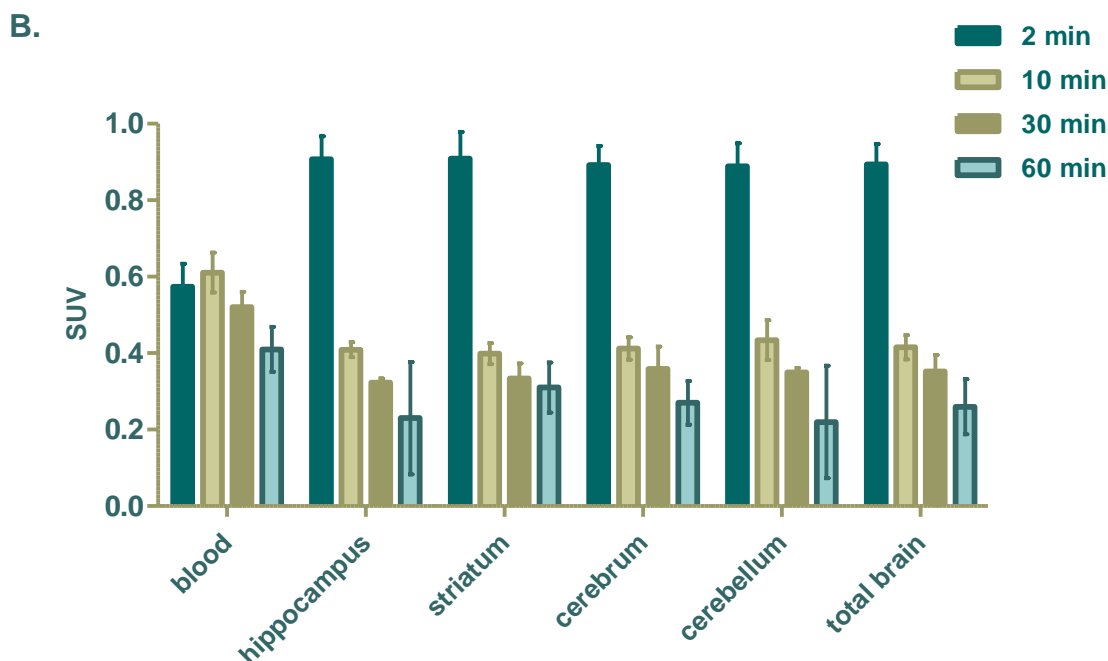


Figure 5: Biodistribution and regional brain distribution of  $[^{11}\text{C}]\text{G611}$  in mice at 2, 10, 30 and 60 min post tracer in baseline conditions. A. Top figure shows the general distribution (% ID) of the tracer in adult NMRI mice at different time points ( $n=3/\text{time point}$ ). B. Bottom figure shows the relative regional brain and blood concentrations (SUV).

### 2.6.2. Blocking biodistribution study

Based on the results of the baseline biodistribution study we decided to perform a blocking study 30 min post tracer injection. This biodistribution study was performed on mice ( $n=3$ ) after blocking with G611 or GLPG1205 (10 mg/kg, *i.p.*). Figure 6 showed the radioactivity concentration in major organs and blood. We observed strong blocking in kidney with self-block and to a lesser degree with GLPG1205. This suggests that  $[^{11}\text{C}]\text{G611}$  is substrate of a saturatable kidney transporter, however further *in vitro* autoradiography experiments or biodistribution studies in GPR84 knock-out mice need to be performed to further elucidate this observation. We did not observe any blocking in other organs. We observed an increase in tracer concentration in all the studied brain regions. Probably due to increased systemic availability of the tracer by renal blocking combined with low specific binding in brain due to low brain expression of GPR84 in healthy conditions.

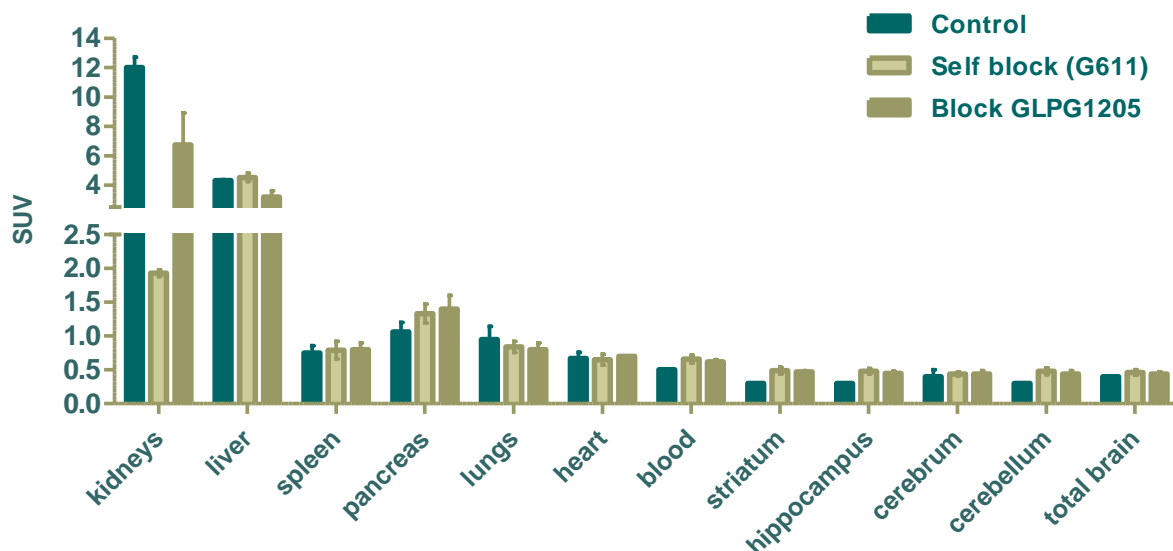


Figure 6: Biodistribution of [ $^{11}\text{C}$ ]G611 in mice. Blocking study (GLPG1205, self-block (G611 (10 mg/kg i.p. 30 min prior to tracer injection) and vehicle control. The graph shows the biodistribution (expressed as SUV) in all the major organs and different brain regions.

### 2.6.3. LPS pre-treatment and biodistribution study in mice

A biodistribution study was performed after LPS pre-treatment with 24h and 3h. We observe significant ( $p=0.03$ ) increased uptake of the [ $^{11}\text{C}$ ]G611 in the various brain regions 24h after pre-treatment but similar brain uptake values at 3h post pre-treatment with LPS compared to control animals. We did not observe any increase in signal in the other studied organs including blood. This is in line with previously reports that found an increase in GPR-84 expression after LPS treatment [139].

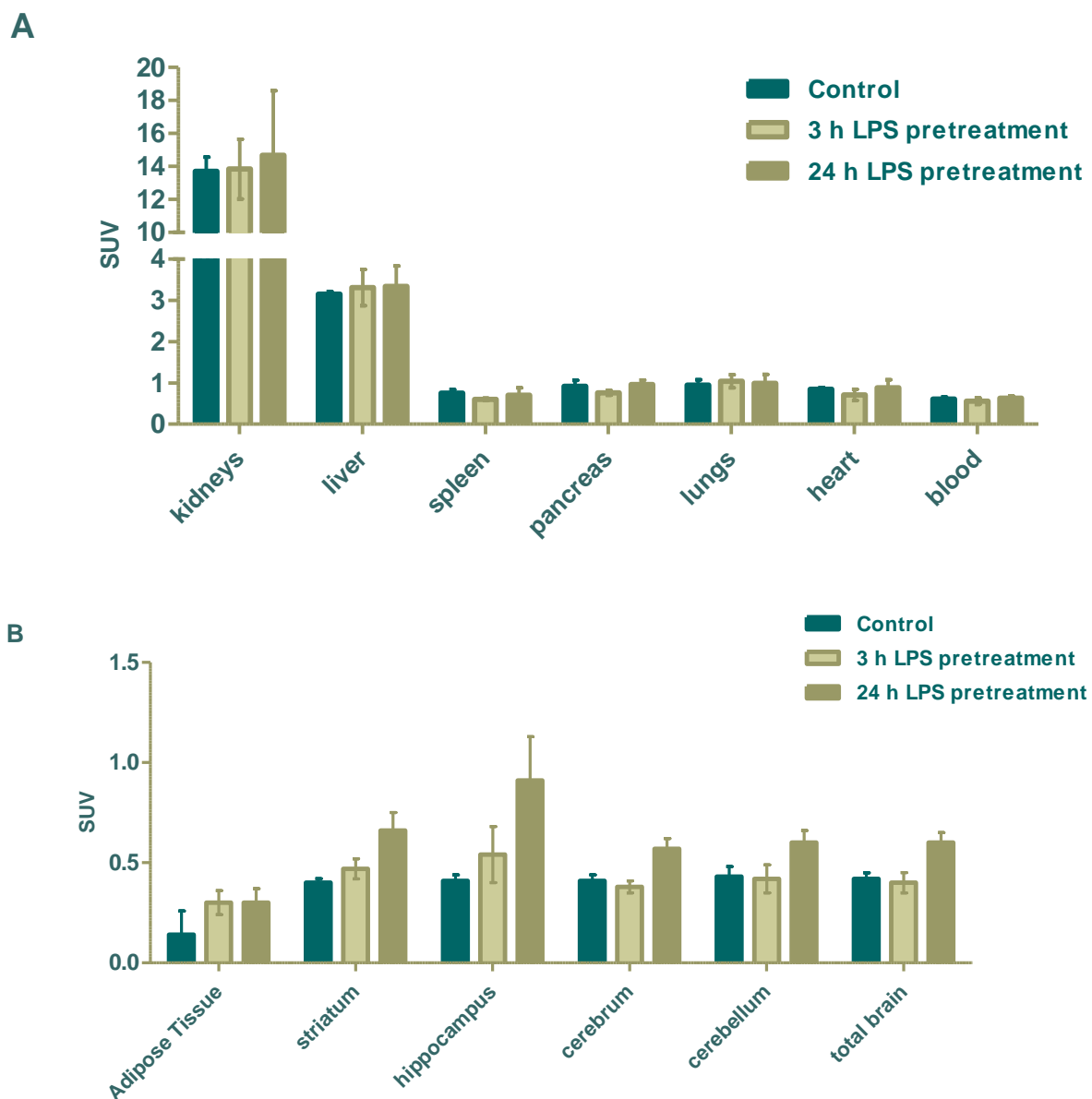


Figure 7: Biodistribution and regional brain distribution of [ $^{11}\text{C}$ ]G611 (10 min post tracer injection) in control mice and after 3 or 24 h pre-treatment with LPS (1 mg/kg, i.p.). A. Top figure shows the tracer concentration in major organs (SUV). B. Bottom figure shows the relative regional brain and adipose tissue concentrations (SUV).

## 2.7. RNA analysis

RNA analysis was performed on samples from brain, kidney and white adipose tissue 6h and 24h after LPS treatment. We observed that GPR84 is expressed in both fat and brain tissue but has a low expression in kidney (Figure 8). GPR84 and TNF $\alpha$  expression increases in THP-1

cells treated for 24h with LPS, and its expression is not affected after treatment with 50 mM GLPG1205.

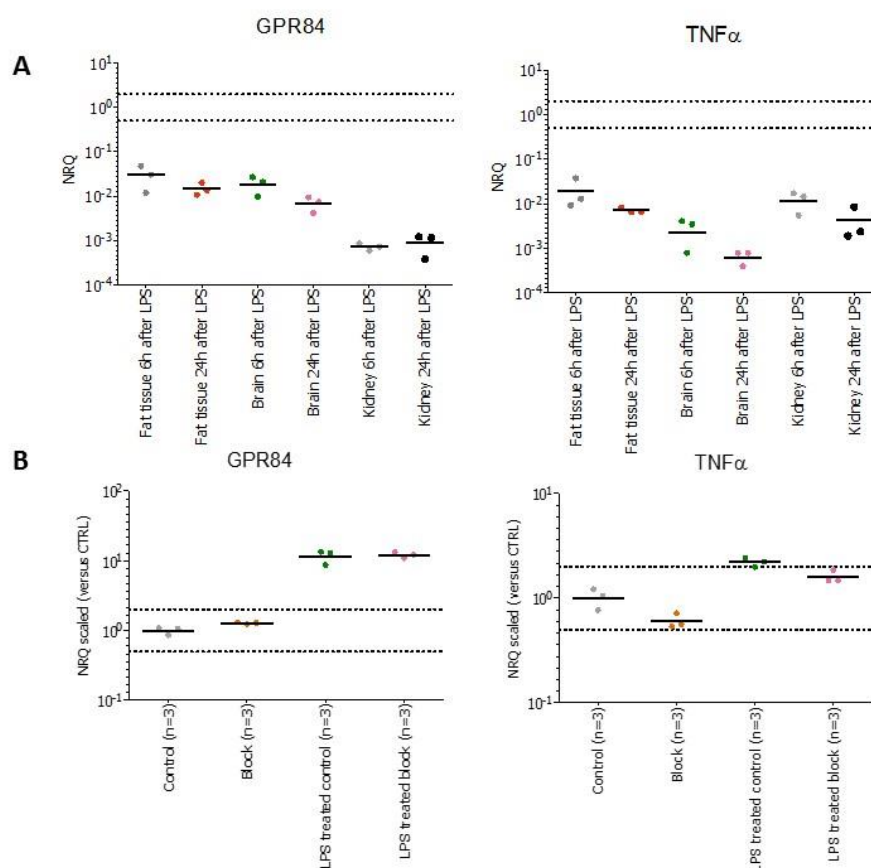


Figure 8: GPR-84 and TNF $\alpha$  gene expression study A. in mice tissues, 6 or 24h after treatment with LPS (1 mg/kg, i.p.) B. THP-1 cells, 24h after LPS treatment (10 ng/ml).

### 3. Materials and Methods

#### 3.1. General materials and methods

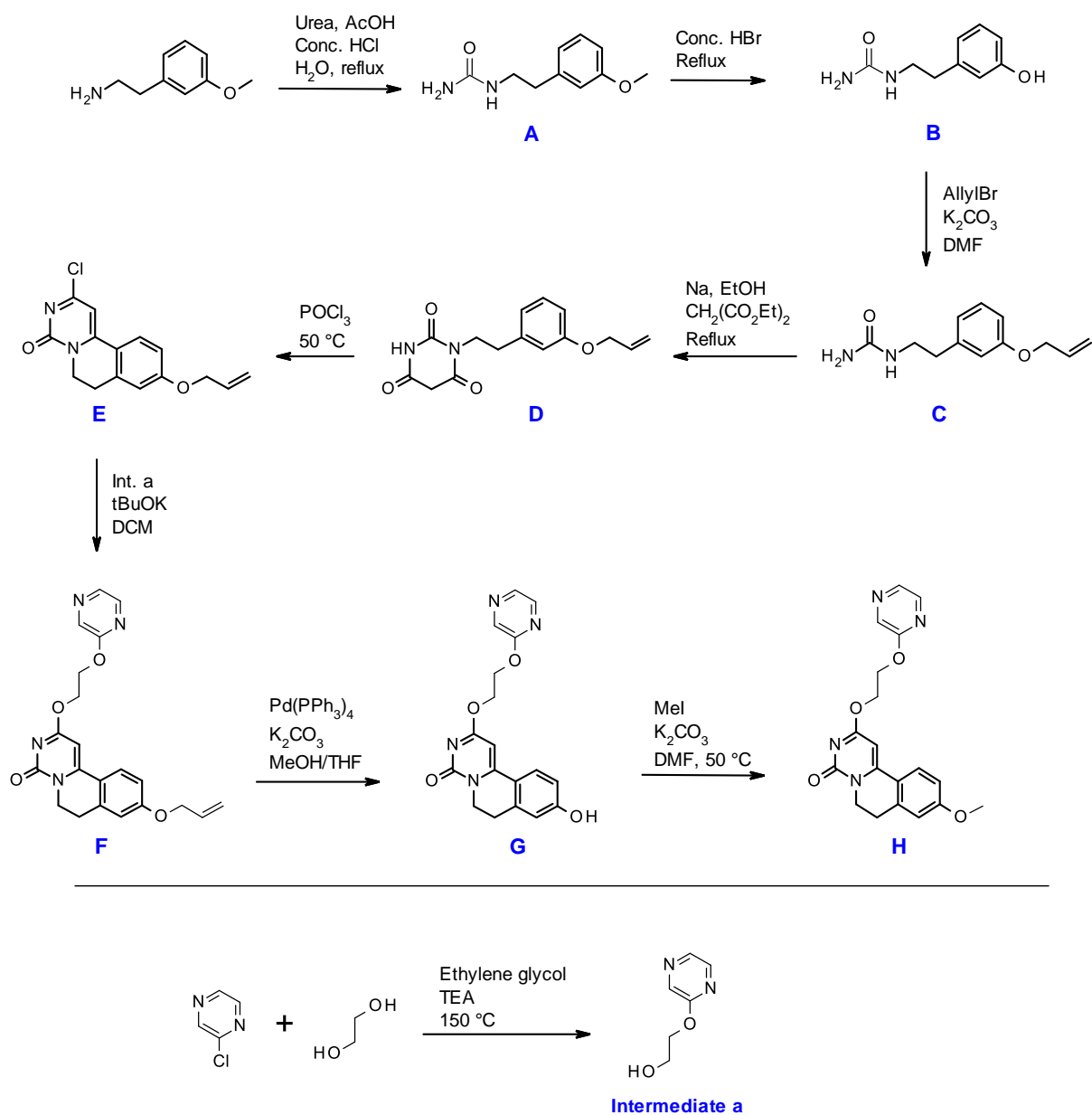
All the chemicals employed in the synthesis were purchased from reliable commercial suppliers (Aldrich, TCI Europe or ACROS) and used without further purification unless otherwise stated.  $^1\text{H}$  and  $^{13}\text{C}$ -nuclear magnetic resonance (NMR) spectra were obtained on a 400 MHz Bruker NMR spectrometer in the deuterated solvents as indicated and with tetramethylsilane, TMS ( $\delta = 0$ ) as an internal standard. Chemical shifts ( $\delta$ ) are reported in ppm and coupling constants are

reported in Hertz. Multiplicity is defined by s (singlet), d (doublet), t (triplet), and m (multiplet). The mass spectra were recorded on a Bruker maXis impact UHR-TOF mass spectrometer coupled to a Dionex 3000RS UHPLC system (Bruker-Daltonik, Bremen, Germany).

High performance liquid chromatography (HPLC) was performed using a Shimadzu LC-2010A HT system connected to a UV spectrometer. Radioactivity in the column eluent was monitored using a 3-in NaI(Tl) scintillation detector connected to a single channel analyser (Gabi box, Raytest, Straubenhardt, Germany). Radioactivity in samples of biodistribution studies and radiometabolite analysis was quantified with an automated gamma counter, equipped with a 3-in NaI(Tl) well crystal coupled to a multichannel analyser (Wallac 1480 Wizard, Wallac, Turku, Finland). The results were corrected for background radiation, detector dead time and physical decay during counting.

All animals were housed in individually ventilated cages in a thermoregulated (22 °C) and humidity-controlled environment under a 12h/12h day/night cycle with free access to food and water. All animal experiments were approved by the local Animal Ethics Committee of the University of Leuven (P104/2016) and were in accordance with European Ethics Committee guidelines (decree 86/609/EEC).

## 3.2. Synthesis of reference and precursor



Scheme 1: Synthesis of precursor (G) and reference (H).

## 2-Pyrazin-2-yloxyethanol (intermediate a)

A mixture of 2-chloropyrazine (1 mL, 0.011 mmol), ethylene glycol (10 mL, 0.18 mmol) and TEA (1.63 mL, 0.01 mmol) was heated to  $150\text{ }^\circ\text{C}$  for 2.5 days. The reaction was diluted in

EtOAc, washed with brine and a saturated solution of  $K_2CO_3$ , then the organic layer was dried over  $MgSO_4$ , filtered and evaporated to dryness to get crude intermediate a as an orange oil (1 g) which was used as such without further purification.

$^1H$  NMR (400 MHz,  $DMSO-d_6$ )  $\delta$  8.33 – 8.26 (m, 1H), 8.19 (d,  $J = 0.5$  Hz, 2H), 4.35 – 4.28 (m, 2H), 3.73 (q,  $J = 4.5$  Hz, 2H).

#### *2-(3-Methoxyphenyl)ethylurea (A)*

A solution of 3-methoxyphenethylamine (100 g, 661.3 mmol), urea (157.3 g, 2619.0 mmol), glacial AcOH (36 mL) and conc. HCl (12 mL) in  $H_2O$  (800 mL) was heated under reflux for 5 days. The reaction mixture was cooled to RT, the precipitate obtained was filtered off, washed with water and dried under vacuum to give A as a white solid (92 g, 72% yield).

$^1H$  NMR (400 MHz, Methanol- $d_4$ )  $\delta$  7.18 (t,  $J = 8.1$  Hz, 1H), 6.83 – 6.71 (m, 3H), 3.77 (s, 3H), 3.37 – 3.31 (m, 2H), 2.74 (t,  $J = 7.2$  Hz, 2H).

#### *2-(3-Hydroxyphenyl)ethylurea (B)*

A solution of A (92 g, 473.6 mmol) in conc. HBr (600 mL) was heated under reflux overnight. The reaction was cooled to RT, and basified by addition of  $NaHCO_3$  and extracted with EtOAc. The organic layer was dried over  $MgSO_4$ , filtered and concentrated under reduced pressure to give crude B as a light brown solid (67 g) which was used in the next step without further purification.

$^1H$  NMR (400 MHz,  $DMSO-d_6$ )  $\delta$  9.25 (s, 1H), 7.07 (td,  $J = 7.2, 1.8$  Hz, 1H), 6.65 – 6.55 (m, 3H), 5.89 (t,  $J = 5.8$  Hz, 1H), 3.16 (dt,  $J = 7.7, 6.3$  Hz, 2H), 2.57 (t,  $J = 7.3$  Hz, 2H). LCMS:  $m/z$  181  $[M + H]^+$

*2-(3-Allyloxyphenyl)ethylurea (C)*

To a solution of crude B (67 g, 371.0 mmol) and K<sub>2</sub>CO<sub>3</sub> (154 g, 1115.0 mmol) in DMF (400 mL) was added allylbromide (75 mL, 743.6 mmol) and the reaction was stirred for 2.5 days. DMF was concentrated under reduced pressure then the residue was dissolved in EtOAc, washed with a saturated aqueous solution of Na<sub>2</sub>CO<sub>3</sub> followed by brine, then dried over MgSO<sub>4</sub>. Concentration under reduced pressure gave crude C as a colourless solid (79 g) which was used in the next step without further purification.

<sup>1</sup>H NMR (400 MHz, methanol-*d*<sub>4</sub>)  $\delta$  7.97 (s, 1H), 7.22 – 7.13 (m, 1H), 6.84 – 6.71 (m, 3H), 6.13 – 5.97 (m, 1H), 5.39 (dq, *J* = 17.3, 1.7 Hz, 1H), 5.23 (dq, *J* = 10.6, 1.6 Hz, 1H), 4.52 (ddt, *J* = 5.1, 3.5, 1.6 Hz, 2H), 3.34 (d, *J* = 7.0 Hz, 2H), 2.98 (d, *J* = 0.6 Hz, 2H), 2.74 (t, *J* = 7.3 Hz, 2H). LCMS: *m/z* 221 [M + H]<sup>+</sup>

*1-[2-(3-Allyloxyphenyl)ethyl]hexahydropyrimidine-2,4,6-trione (D)*

To a stirred solution of sodium (16 g, 718.0 mmol) in EtOH (1.0 L), diethyl malonate (109.1 mL, 718.0 mmol) was added and the reaction mixture was heated under reflux for 1h. Crude C (72 g, 359.0 mmol) in EtOH (200 mL) was added and the reaction mixture was heated under reflux for 12 h. The reaction was cooled to RT, 1N aq. HCl was added and the precipitate obtained was filtered off, washed with water and dried under vacuum to give D as a yellow solid (82 g, 79% yield).

<sup>1</sup>H NMR (400 MHz, CDCl<sub>3</sub>)  $\delta$  8.36 (s, 1H), 7.25 – 7.16 (m, 1H), 6.87 – 6.72 (m, 3H), 6.05 (ddt, *J* = 17.3, 10.5, 5.3 Hz, 1H), 5.41 (dq, *J* = 17.3, 1.6 Hz, 1H), 5.28 (dq, *J* = 10.5, 1.4 Hz, 1H), 4.53 (dt, *J* = 5.3, 1.5 Hz, 2H), 4.15 – 4.04 (m, 2H), 3.61 (s, 2H), 2.92 – 2.82 (m, 2H). LCMS: *m/z* 289 [M + H]<sup>+</sup>



*9-Allyloxy-2-chloro-6,7-dihydropyrimido[6,1-a]isoquinolin-4-one (E)*

A solution of **D** (50 g, 173.4 mmol) in POCl<sub>3</sub> (100 mL) was stirred at 50°C for 3 days. POCl<sub>3</sub> was concentrated under pressure, the residue was dissolved in DCM and quenched with a saturated aqueous solution of NaHCO<sub>3</sub>. The organic layer was washed with water, dried over MgSO<sub>4</sub>, filtered and concentrated under reduced pressure to give crude **E** as a yellow solid (46 g, 92% yield).

<sup>1</sup>H NMR (400 MHz, CDCl<sub>3</sub>) δ 7.67 (d, *J* = 8.8 Hz, 1H), 6.94 (dd, *J* = 8.8, 2.6 Hz, 1H), 6.85 – 6.80 (m, 1H), 6.67 (s, 1H), 6.04 (ddt, *J* = 17.2, 10.5, 5.2 Hz, 1H), 5.43 (dq, *J* = 17.3, 1.6 Hz, 1H), 5.34 (dq, *J* = 10.5, 1.4 Hz, 1H), 4.62 (dt, *J* = 5.3, 1.5 Hz, 2H), 4.26 – 4.19 (m, 2H), 3.01 (t, *J* = 6.7 Hz, 2H). LCMS: *m/z* 289 [M + H]<sup>+</sup>

*9-Allyloxy-2-(2-pyrazin-2-yloxyethoxy)-6,7-dihydropyrimido[6,1-a]isoquinolin-4-one (F)*

Intermediate a (1.12 g, 7.98 mmol) was added to a stirred solution of tBuOK (1.05 g, 9.37 mmol) in DCM (20 mL) cooled at 0 °C. After 15 min, **E** (2 g, 6.94 mmol) was added to the mixture at 0 °C, then the reaction was allowed to warm to RT overnight. The organic layer was washed with H<sub>2</sub>O, dried over MgSO<sub>4</sub> then evaporated to dryness. The residue was purified by flash chromatography on silica gel eluting with 2% MeOH/DCM to afford **F** as a pale yellow powder (2.4g, 88% yield).

<sup>1</sup>H NMR (400 MHz, CDCl<sub>3</sub>) δ 8.25 (d, *J* = 1.4 Hz, 1H), 8.11 (dd, *J* = 2.8, 1.3 Hz, 1H), 8.05 (dd, *J* = 2.8, 1.4 Hz, 1H), 7.61 (d, *J* = 8.8 Hz, 1H), 6.88 (dd, *J* = 8.8, 2.6 Hz, 1H), 6.77 (d, *J* = 2.6 Hz, 1H), 6.23 (s, 1H), 6.02 (ddt, *J* = 17.2, 10.5, 5.3 Hz, 1H), 5.40 (dq, *J* = 17.2, 1.6 Hz, 1H), 5.30 (dq, *J* = 10.5, 1.4 Hz, 1H), 4.79 – 4.72 (m, 2H), 4.69 – 4.62 (m, 2H), 4.58 (dt, *J* = 5.2, 1.5 Hz, 2H), 4.22 – 4.10 (m, 2H), 2.95 (t, *J* = 6.5 Hz, 2H). LCMS: *m/z* 393 [M + H]<sup>+</sup>

*9-Hydroxy-2-(2-pyrazin-2-yloxyethoxy)-6,7-dihydropyrimido[6,1-a]isoquinolin-4-one (G)*

K<sub>2</sub>CO<sub>3</sub> (1.69 g, 12.23 mmol) was added to a stirred solution of **F** (2.4 g, 6.11 mmol) in a mixture of THF (70 mL) / MeOH (50 mL). The solution was degassed under a stream of N<sub>2</sub>, Pd(PPh<sub>3</sub>)<sub>4</sub> (212 mg, 0.31 mmol) was added, and the reaction was stirred at RT overnight. The mixture was evaporated to dryness, the residue was dissolved in DCM and washed with H<sub>2</sub>O. The layers were separated and the aqueous layer was cooled to 0 °C and adjusted to pH 6 by addition of 2N HCl, then it was extracted with 10% MeOH in DCM. The organic layers were combined and dried over MgSO<sub>4</sub> and evaporated to dryness to give crude **G** as a pale yellow powder (1.82 g), which was used in the next step without further purification.

<sup>1</sup>H NMR (400 MHz, methanol-*d*<sub>4</sub>) δ 8.20 (d, *J* = 1.4 Hz, 1H), 8.16 – 8.05 (m, 2H), 7.67 – 7.59 (m, 1H), 6.80 (dd, *J* = 8.7, 2.5 Hz, 1H), 6.72 (d, *J* = 2.5 Hz, 1H), 6.34 (s, 1H), 4.73 – 4.63 (m, 4H), 4.16 – 4.08 (m, 2H), 2.95 (t, *J* = 6.5 Hz, 2H). LCMS: *m/z* 353 [M + H]<sup>+</sup>

*9-Methoxy-2-(2-pyrazin-2-yloxyethoxy)-6,7-dihydropyrimido[6,1-a]isoquinolin-4-one (H)*

Methyl iodide (37 μL, 0.60 mmol) was added to a stirred solution of **G** (100 mg, 0.28 mmol) and K<sub>2</sub>CO<sub>3</sub> (116 mg, 0.84 mmol) in DMF (0.7 mL) and the reaction was stirred at 50 °C for 1h. The mixture was worked up with DCM and H<sub>2</sub>O, the organic layer was dried over MgSO<sub>4</sub> and evaporated to dryness. Crude product was purified by semi-preparative HPLC (0.1% TFA in water/MeCN).

<sup>1</sup>H NMR (400 MHz, DMSO-*d*<sub>6</sub>) δ 8.37 (d, *J* = 1.2 Hz, 1H), 8.27 – 8.20 (m, 2H), 7.95 (d, *J* = 8.8 Hz, 1H), 7.01 – 6.91 (m, 2H), 6.55 (s, 1H), 4.64 (s, 4H), 4.06 – 3.98 (m, 2H), 3.84 (s, 3H), 2.98 (t, *J* = 6.5 Hz, 2H). LCMS: *m/z* 367 [M + H]<sup>+</sup>

### 3.3. *In vitro* evaluation

Binding of GTP to the alpha subunit of heterotrimeric GTP binding proteins is an early event in agonist-induced activation of G-protein coupled receptors. Usually GTP $\gamma$ S binding assays are carried out using membrane preparations in the same way as radioligand binding assays. These assays are carried out using [<sup>35</sup>S]GTP $\gamma$ S a radioactive ligand with high affinity for G-protein  $\alpha$  subunits that is highly resistant to the inherent GTPase activity of  $\alpha$  subunits such that it remains bound for sufficient period of time to allow counting of radioactivity [199].

Assay protocol as follows, G611 was diluted (compound is prepared as serial dilutions: 20 $\mu$ M highest concentration, 1/3 dilution steps starting from 10mM stocks; 10 point dose response) and transferred to a white 96 well LIA plate. The assay reaction was carried out by adding 50  $\mu$ l of G611 to 30 $\mu$ l GPR84 membrane preincubated with PVT-WGA SPA beads + 20 $\mu$ l DIM at EC80 for 90 min at room temperature. After addition of 20 $\mu$ l of 4.8M CsCl, each well was centrifuged for 20 min, at 2000 rpm and readout on TopCount-liquid scintillation counter ([<sup>35</sup>S]GTP $\gamma$ S, 1min readout time/well).

### 3.4. *Radiosynthesis*

[<sup>11</sup>C]MeI was produced according to the procedure described by Andrés *et. al.* [167] and bubbled with a stream of helium through a solution of the radiolabelling precursor (200  $\mu$ g) and K<sub>2</sub>CO<sub>3</sub> (1-3 mg) in anhydrous DMF (200  $\mu$ L). The mixture was then heated for 3 min at 70 °C. After dilution with 1 mL water, the crude reaction mixture was purified by HPLC using an XBridge C<sub>18</sub> column (5 $\mu$ m, 4.6 mm x 150 mm; Waters, Milford, Connecticut) eluted with a mixture of 0.05 M sodium acetate buffer pH 5.5 and EtOH (65/35 v/v) at a flow rate of 1 mL/min. UV monitoring of the eluate was performed at 254 nm. The peak corresponding to [<sup>11</sup>C]G611 was collected, diluted with saline to obtain a final ethanol concentration of <10% and sterile filtered through a 0.22- $\mu$ m membrane filter (Millex GV 13 mm; Millipore, Billerica,

MA). The chemical and radiochemical purity of the tracer was assessed using HPLC on an analytical XBridge C<sub>18</sub> column (3.5 µm, 3.0 mm x 100 mm, Waters) eluted with a mixture of a 0.05 M sodium acetate buffer pH 5.5 and acetonitrile (70/30 v/v) at a flow rate of 0.6 mL/min. UV detection was done at 230 nm. Identity of the tracer was confirmed by co-elution with authentic cold reference on the same HPLC system.

### ***3.5. Cell uptake experiments***

A day before the cell binding study, GPR84 transduced HEK-293 cells and control HEK-293 cells were plated in triplicate in a 24-well plate with 200,000 cells/well. The cells were checked for confluency (90-100%), the incubation medium was removed and 250 µl medium containing tracer (2 MBq) or tracer (2 MBq)+block (50 µM) solutions. Cells were incubated for 10 or 30 min at 37°C with 5% CO<sub>2</sub> in air. After the incubation the media was removed and cells were washed three times with 250 µl of ice cold PBS. Then cells were washed 2 times with 500 µl of Glycine-HCl 50 mM pH 2.8. Again the cells were washed three times with 250 µl of ice cold PBS. Finally, the cells were lysed with 250 µl of lysate buffer followed by 250 µl of neutralization buffer. All the wash fractions were collected separately and counted using a gamma counter. The tracer uptake was normalised to 10<sup>6</sup> cells.

A similar protocol was used for THP-1 cells, these cells were floating cells hence after each washing step the cells were centrifuged for 5 min at 1200 rpm. For LPS pre-treatment LPS 055:B5 (Sigma Aldrich) at a concentration of 100 ng/ml in media was used.

### **3.6. *In vitro* autoradiography**

Transverse sections of mouse brains were obtained using a cryotome (Shandon cryotome FSE, Thermo Fisher, Waltham, USA), mounted on microscopic slides and stored at -20 °C until used. Before the autoradiography experiment, the brain slices were air-dried followed by pre-incubation in PBS pH 7.4 for 10 min and excess liquid is removed from the slides. A control tracer solution (9 mL PBS of 0.4 MBq/mL [<sup>11</sup>C]G611 solution+ 1 mL of DMSO) and blocking-tracer solution (9 mL PBS of 0.4 MBq/mL solution + 1 mL of 200 µM of GLPG1205 in DMSO) were prepared. 500 µL of the control and block solutions were added on mouse brain sections (n=3) incubated for 15 min at room temperature. The slides were washed twice for 5 min with PBS buffer on ice. Subsequently, the slides were washed with ice cold water and the slides were dried with a heat gun. Autoradiograms were obtained by exposing the slides to phosphor storage screen overnight. The screen was read using a Cyclone Plus system and analysed using OptiQuant software.

### **3.7. *Biodistribution study***

Biodistribution studies were carried out in healthy adult NMRI mice at 2, 10, 30 or 60 min post injection (p.i.) (n = 3 per time point). Additional biodistribution studies (30 min p.i., n = 3 per time point) were performed 30 min after pre-treatment with G611 (10 mg/kg) or GLPG1205. Blocking compounds were formulated in a mixture of 5% DMSO, 20% 2-hydroxypropyl  $\beta$ -cyclodextrin in saline and administered via intraperitoneal (*i.p.*) route. During the procedure, mice were anesthetized with 2.5% isoflurane in O<sub>2</sub> at a flow rate of 1 L/min and injected with about 9 MBq of tracer *via* a tail vein. The animals were then sacrificed by decapitation at 2, 10, 30 or 60 min p.i.. Blood and major organs were collected in tared tubes and weighed. The radioactivity in blood, organs and other body parts was counted using an automated gamma

counter. For calculation of the total radioactivity in blood, blood mass was assumed to be 7% of the total body mass [168].

Biodistribution was performed on mice pre-treated with LPS 055:B5 (Sigma Aldrich), with *i.p.* injection of 1 mg/kg body weight 3h or 24h before tracer injection. The mice were sacrificed at 10 minutes post injection and various organs isolated, the radioactivity was counted as described higher. Data were expressed as percentage of injected dose (%ID) and standardized uptake value (SUV). %ID was calculated as (counts per minute (cpm) in organ / total cpm recovered) x 100%. SUV was calculated as (radioactivity in cpm in organ / weight of organ in gram) / (total cpm recovered/total body weight in gram).

### **3.8. RNA analysis**

Total RNA was extracted from tissues or cells using Qiagen RNA extraction kits following manufacturer's instructions. Fat tissues were processed according to TRIzol Reagent User Guide. Total RNA was treated with DNase I (Ambion Inc., Austin, Texas, USA) at 37°C for 30 min, followed by inactivation at 75°C for 5 min. RNA (1 µg) was reverse transcribed with random hexamers using High Capacity cDNA Reverse Transcription kits (Applied Biosystems) following the manufacturer's protocol. Real time quantitative PCR (RT-qPCR) assays were performed using an Applied Biosystems ViiA7 sequence detector. Gene expression levels were determined by Sybr green assays. ACTB, GAPDH and HTRF-1 gene transcripts were used as an internal control to normalise the variations for RNA amounts. Gene expression levels are expressed relative to house-keeping gene mRNA levels. All the results presented are expressed as mean ± S.E.M. All the primers used in this study and Ct values are available upon request.

### **3.9. Statistics**

Quantitative data are expressed as mean  $\pm$  SD. Means were compared using an unpaired two-tailed student t-test. Values were considered statistically significant for  $P \leq 0.05$ .

### **4. Conclusions**

We successfully synthesised a novel PET ligand for GPR84. The GPR84 specificity of developed tracer was confirmed by cell binding experiments with GPR84 transduced cells. The biodistribution study confirmed a good entry of [ $^{11}\text{C}$ ]G611 into mouse brain. Further studies performed with LPS pre-treatment showed increased tracer retention in mouse brains *in vivo* and THP-1 cells *in vitro*. Biodistribution studies after blocking with G611 or GLPG1205 demonstrated absence of GPR84 specific binding in control mouse brain. Further studies with [ $^{11}\text{C}$ ]G611 in other models of neuroinflammation will be required to investigate its potential as a neuroinflammation tracer.

### **5. Acknowledgements**

We would like to thank Julie Cornelis (Radiopharmaceutical Research) for her expert help with the mice and rat studies.





## **CHAPTER-VI**

### **GENERAL DISCUSSION AND FUTURE PERSPECTIVES**



## 1. Overview and comparison of developed radioligands

This thesis describes the development of four radiotracers shown in Figure 1. Their main characteristics are summarised in Table 1.

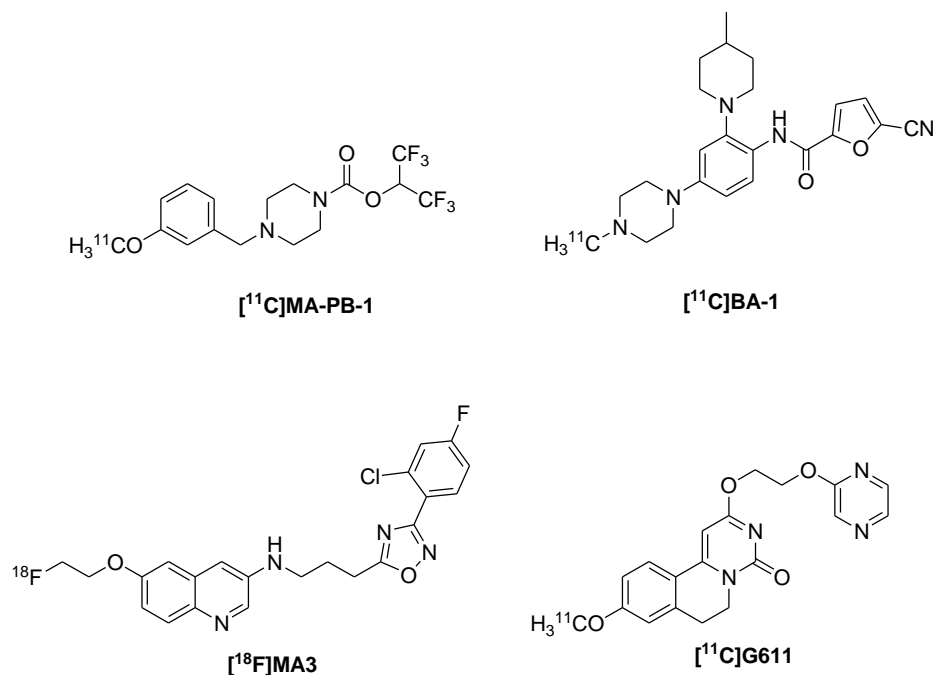


Figure 1: Structures of developed radioligands

As discussed in the introduction (Chapter I), desirable molecular characteristics for entering the brain by passive diffusion are low molecular weight (<500 Da), a polar surface area (PSA) of <90 Å<sup>2</sup>, a lack of formal charge at physiological pH and a logD between 1 and 3. All the four studied tracers were able to cross the BBB. [<sup>11</sup>C]MA-PB-1 displayed the highest brain penetration (3.5 % of ID at 2 min p.i.) and showed slow washout from the brain (Table 1). [<sup>18</sup>F]MA3 has a clogD value of 4.7, out of the ideal range but still showed good brain uptake and rapid washout. [<sup>11</sup>C]BA-1 is in the ideal clogD range with (2.5) and displayed good brain uptake and slow washout. [<sup>11</sup>C]G611 is rather hydrophilic (clogD of 0.8) and nevertheless demonstrated good brain uptake and reasonable washout. All the studied tracers have low cPSA values although [<sup>11</sup>C]G611 approaches the upper limit.

Table 1: Properties of developed radioligands

Radiotracer	[ <sup>11</sup> C]MA-PB-1	[ <sup>18</sup> F]MA3	[ <sup>11</sup> C]BA-1	[ <sup>11</sup> C]G611
<b>Target</b>	MAGL (membrane enzyme)	CB <sub>2</sub> receptors	CSF-1 receptors	GPR84
<b>clogD<sup>I</sup></b>	3.4	4.8	2.5	0.8
<b>cPSA<sup>I</sup> (Å<sup>2</sup>)</b>	42	73	72	86
<b>IC<sub>50</sub></b>	26 nM	0.8 nM	1 nM	41 nM
<b>Brain uptake in mice %ID<sub>2min p.i.</sub></b>	3.5	1.2	3	0.9
<b>Brain washout %ID<sub>2 min/60 min p.i.</sub></b>	1.3	12	2.1	3
<b>Radiochemical synthesis</b>	Alkylation reaction with [ <sup>11</sup> C]methyl iodide	Alkylation reaction with 1-bromo-2-[ <sup>18</sup> F]fluoroethane	Alkylation reaction with [ <sup>11</sup> C]methyltriflate	Alkylation reaction with [ <sup>11</sup> C]methyl iodide
<b>Radiochemical yield<sup>II</sup></b>	40 %	19%	60 %	80 %
<b>Preclinical evaluation</b>	<i>h</i> MAGL affinity assay, mice, rats and monkey microPET	Local overexpressed <i>h</i> CB <sub>2</sub> R AAV rat model, monkey	Mice, rats and monkeys microPET	GTPγS affinity assay, cell binding study in GPR84 transduced HEK-293 cells and THP-1 monocytes, mice
<b>TAC<sup>III</sup> analysis</b>	Specific irreversible binding	Specific reversible binding	High nonspecific binding	N/A
<b>Antibodies (Abs)</b>	Available	No validated Abs	Available	No specific Abs
<b>Animal model of interest</b>	MAGL KO[200], APP Tg models of AD[201,202], PC[203]	AD[204], ALS[205], Glioma[206],	AD[207,208], SIV/HIV <sup>IV</sup> [209], Glioma[190,210], RA[129,135]	GPR84 KO and neuropathic pain[147]

<sup>I</sup> clogD and cPSA values calculated using Marvin sketch 18.10

<sup>II</sup> alkylation reaction yields (based on the AUC of radiometric channel of the prep HPLC)

<sup>III</sup> time activity curve

<sup>IV</sup> Simian immunodeficiency virus (SIV)/Human immune deficiency virus (HIV)

[<sup>18</sup>F]MA3 especially [<sup>11</sup>C]MA-PB-1 PET ligands showed further translational potential to humans in healthy volunteers and patients. However, [<sup>11</sup>C]BA-1 due to its high non-specific binding may not be ideal for brain CSF-1R imaging. [<sup>11</sup>C]G611 further validation is required in neuropathic pain and GPR84 KO mouse models before translating to human imaging.

### ***1.1. MAGL imaging with [<sup>11</sup>C]MA-PB-1***

Non-invasive imaging of MAGL using PET can assist in the translational evaluation of promising drug candidates that aim to inhibit MAGL. Furthermore, PET imaging of MAGL also enables quantifying MAGL expression *in vivo*, thus allowing to identify modulation of MAGL in relevant pathologies such as neuro(inflammation), cancer, anxiety, and addiction. Chapter II in this thesis focused on the synthesis and preclinical evaluation of [<sup>11</sup>C]MA-PB-1 for *in vivo* imaging of brain MAGL.

Substitution of the phenoxy group of JW642 with a methoxy group (MA-PB-1) while not affecting inhibitor potency has decreased the clogD value to 3.4 and cPSA 42 Å<sup>2</sup> when compared to JW642 clogD of 5 and PSA of 42 Å<sup>2</sup> and is within the valid range for efficient BBB passage.

*In vitro* autoradiography studies were performed on rat brain sections, co-incubation with non-radioactive MA-PB-1 or MJN110 were carried out. However, we are unable to saturate [<sup>11</sup>C]MA-PB-1 binding. We hypothesise that being a soluble cytosolic enzyme, MAGL might have washed off during the autoradiography washing protocols. Several studies have confirmed high expression of MAGL in prostate cancer [103,203] and AD [201,202]. It would be rational to perform *in vitro* tests with post-mortem brain or tumor tissues using autoradiography, but unfortunately, this is not possible due to above mentioned reasons.

[<sup>11</sup>C]MA-PB-1 clinical evaluation is thus the logical next step. Compartmental modelling using plasma radiometabolite quantification are necessary to quantify MAGL expression in healthy human volunteers. Further, an examination of test/retest variability in healthy volunteers, determination of biodistribution and radiation absorbed dose of [<sup>11</sup>C]MA-PB-1 should be investigated.

In a next step, [<sup>11</sup>C]MA-PB-1 can be used to quantify MAGL expression levels in different pathologies such as AD, PD and prostate cancer. A recent study from Navarrete *et al.* found an increase in MAGL gene expression in putamen of PD patients [211].

A clinical study with BIA 10-2474, a FAAH inhibitor developed by the Portuguese company Bial, led to fatal outcomes whereby one volunteer died, and five others faced severe neurological problems. Subsequent investigations revealed that at higher concentrations the Bial drug intervened with the activity of lipases, particularly PNPLA6, which might have led to the neurological disorders [212,213]. Hence, it is important to test drug molecules with PET to determine the dose-occupancy relation to avoid overdosing. Our group recently reported a multiple ascending dose occupancy study of JNJ-42165279 (FAAH inhibitor) from Janssen Research and Development with a FAAH specific PET radiotracer [<sup>11</sup>C]MK3168 from Merck to determine dose occupancy.

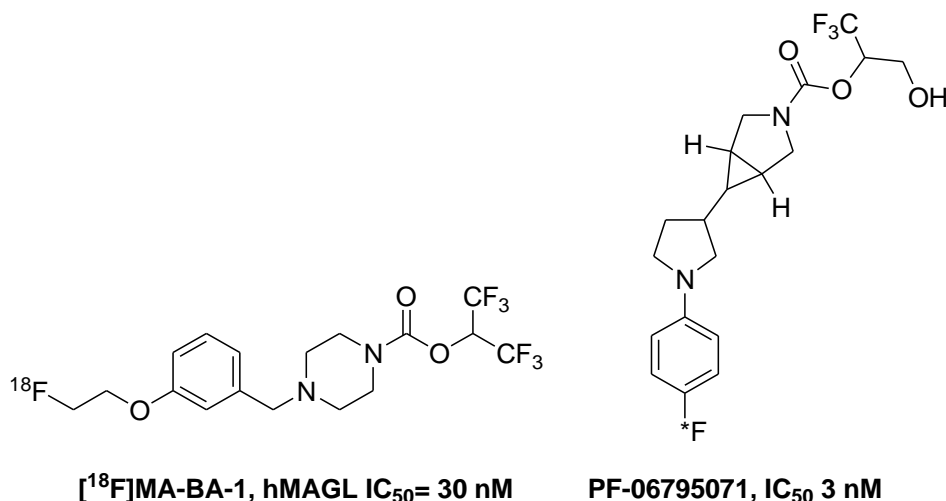


Figure 1: Structures of [<sup>18</sup>F]MA-BA-1 and PF-06795071 MAGL inhibitor

The future investigators are encouraged to evaluate [<sup>18</sup>F]MA-BA-1 (Figure 1), a potential fluorine-18 labelled MAGL PET tracer to circumvent the limitations caused by the shorter half-life of ([<sup>11</sup>C]MA-PB-1) and the necessity of on-site cyclotron for studies. Recently reported MAGL inhibitor (PF-06795071, Figure 1) with a trifluoromethylglycol leaving group was designed based on the MAGL natural substrate 2-AG [214]. PF-06795071 displayed high-affinity (IC<sub>50</sub> 3 nM) and a logD of 3.8 with good brain penetration [214]. Radiolabelling of PF-06795071 without causing structural change is possible with fluorine-18 (\*F shown in Figure 1), using spirocyclic iodonium (III) ylides radiofluorination methodology, as the fluorine is in a non-activated position for aromatic nucleophilic substitution. Therefore, future investigation in this direction should consider exploring these novel series of MAGL inhibitors. So far, all the developed PET tracers for MAGL are irreversible it would also be interesting to develop a reversible MAGL PET tracer, which would simplify quantification of MAGL expression using kinetic modelling. However, the affinities of the reported reversible MAGL inhibitors are in μM range far too low for PET imaging [157,215,216].

### 1.2. CB<sub>2</sub>R imaging with [<sup>18</sup>F]MA3

Another captivating and typically studied endocannabinoid target is cannabinoid type 2 receptor, as it is highly expressed on activated microglia under neuroinflammatory conditions. Several CB<sub>2</sub> receptors PET tracers have been and are being developed [95]. [<sup>11</sup>C]NE40 is the only tracer that reached human studies. Chapter III in the current thesis is focused on recently developed agonist PET tracer [<sup>18</sup>F]MA3, that is expected to only bind to the active fraction of CB<sub>2</sub>R. Importantly, the radiolabelling with fluorine-18 (half-life of 109.7 min) has increased the opportunity to transport the developed radiotracer to nearby PET centres that do not have a cyclotron on site. [<sup>18</sup>F]MA3, the CB<sub>2</sub>R agonist tracer with high affinity (0.8 nM) for the hCB<sub>2</sub>R, was extensively evaluated *in vivo*.

[<sup>18</sup>F]MA3 is an agonist, and thus expected to have more affinity towards the (functionally) active receptor fraction, whereas [<sup>11</sup>C]NE40 being an inverse agonist likely does not discriminate between (functionally) active and inactive fraction of CB<sub>2</sub>R [181]. The inactive hCB<sub>2</sub> mutated vector model used to evaluate [<sup>18</sup>F]MA3 in this thesis. However, it has been reported that mutation of the highly conserved aspartate residue in the second transmembrane domain deters the signal transduction in CB<sub>2</sub>R, but retains their ligand recognition properties as observed in wild-type [217]. Indeed, we observed similar binding potentials for inverse agonist [<sup>11</sup>C]NE40 and agonist [<sup>18</sup>F]MA3 confirming that the ligand recognition properties of the mutant CB<sub>2</sub>R are unaffected. This developed AAV vector model can also be used as a system for tracking cells and gene therapy monitoring.

Future investigators are strongly encouraged to prove distinct binding affinities of PET tracers that bind different functional states of CB<sub>2</sub>R. Due to the difference in the homology of CB<sub>2</sub> receptors between rodents and humans (82 % amino acid homology) [218] *in vitro* evaluation of CB<sub>2</sub>R upregulation (e.g. using autoradiography experiments) should be done on post-mortem



brains from AD, ALS and glioma patients, where increased CB<sub>2</sub>R expression was reported [205,206,219] rather than on brains from animal models of these diseases.

One of the challenges that we encountered during autoradiography experiments with [<sup>18</sup>F]MA3 were difficulties to wash off non-specific binding due to its high clogD of 4.7. A PET tracer with high lipophilicity, might extensively bound to plasma proteins thereby reducing the freely available fraction of the radiotracer to enter the brain. Therefore, less lipophilic agonists PET tracer for CB<sub>2</sub>R need to be developed with high affinity and increased brain uptake.

### ***1.3. CSF-1R imaging with [<sup>11</sup>C]BA-1***

Proliferation and activation of microglia is a hallmark of several neurodegenerative disorders. This mechanism is controlled by the activation of colony stimulating factor-1 receptors (CSF-1R). Hence CSF-1R is an ideal target to visualise microglia during neuroinflammation [208]. CSF-1R also found to have many roles in several tumours (e.g. glioma) and rheumatoid arthritis (RA) [128]. Chapter IV in the present dissertation describes the synthesis and preliminary evaluation of [<sup>11</sup>C]BA-1.

Clinical trials are ongoing with several CSF-1R inhibitors, to best of our knowledge there are no specific CSF-1R PET tracers available to date. Based on the literature survey, we adopted a high-affinity molecule 26 with IC<sub>50</sub> of 1 nM for CSF-1R synthesised by Johnson and Johnson, which is easy to radiolabel with carbon-11. The selected molecule also displayed favourable clogD (2.5) and PSA (72Å<sup>2</sup>) values for passive brain penetration. [<sup>11</sup>C]BA-1 was synthesised with good radiochemical yields, purities and high molar activities.

[<sup>11</sup>C]BA-1 showed high brain uptake in rodents and monkey, but this uptake was not blockable with non-radioactive reference BA-1 and BLZ945. The high brain uptake and slow washout could be due to the ionisable amines with pKa values more than six that can mediate

accumulation in lysosomes, known as lysosomal trapping [220,221]. Based on the structure of [<sup>11</sup>C]BA-1 and its calculated pKa values (N-methyl piperazine pKa=7.9), we hypothesize that this tracer undergoes nonspecific lysosomal trapping. This observation was also supported by high lung retention of [<sup>11</sup>C]BA-1 in the mouse biodistribution study.

However, further investigations with [<sup>11</sup>C]BA-1 are required in animal models of RA and in animal tumour models [135,222]. Future researchers are encouraged to explore other molecules with more favourable pKa values as specific PET tracers for *in vivo* imaging of brain CSF-1R to avoid lysosomal trapping.

#### ***1.4. GPR84 imaging with [<sup>11</sup>C]G611***

GPR84 is highly upregulated under various inflammatory conditions such as endotoxemia and experimental autoimmune encephalomyelitis (EAE) indicating a direct correlation of GPR84 upregulation with neuroinflammatory conditions [139,146]. To the best of our knowledge, no PET tracers were developed for GPR84. Additionally, no antibodies are currently available for GPR84. Therefore, it might be interesting to develop radiotracers for GPR84. Chapter V in the current thesis described synthesis, radiolabelling, *in vitro* and *in vivo* evaluation of [<sup>11</sup>C]G611.

G1055611 is a structural analogue of GLPG1205, a GPR84 antagonist developed by Galapagos that is currently in clinical trials. [<sup>11</sup>C]G611 was radiolabelled in good radiochemical yield, high purities, and molar activities. Biodistribution studies confirmed good brain uptake and uniform distribution. LPS pre-treatment studies confirmed increased uptake in [<sup>11</sup>C]G611 but we were not able to demonstrate GPR84 specific binding in brain using *in vivo* blocking studies. Future investigations should explore GPR84 expression during neuroinflammation. Previously it was reported that GPR84 overexpression in neuropathic pain and AD mouse models, thus [<sup>11</sup>C]G611 could be further evaluated in those animal models [146,147].

## SUMMARY

Neuroinflammation is a complex well-orchestrated response to various stimuli aiming to restore tissue homeostasis but under pathological conditions, it can unexpectedly increase tissue damage. NI is observed in several CNS pathologies like AD, PD, stroke, MS, ALS, HD, neoplasia and brain trauma. Microglia are resident CNS cells having similar functions to macrophages. The activation of microglia is a primary adaptation reaction of the brain innate immune system, found in physiological and pathological conditions [2]. During brain damage, microglia rapidly migrate to the site of injury relying on the directional guidance provided by the expressed chemotactic mediators. During activation, microglia undergo functional and morphological changes which are linked to the modulation of expression of several receptors, enzymes, and ion channels [7]. Hence, it is highly relevant to quantify these as biomarkers for diagnosis and the evaluation of progression of neuroinflammation in disease and after therapy. A non-invasive accurate and reliable detection of NI is of fundamental clinical interest. Quantification of microglial activation *in vivo* is possible with positron emission tomography (PET) provided that there is a combination of a relevant molecular target and a suitable radiotracer for this target.

The present study aimed to develop a carbon-11 labelled radioligand to visualise the endocannabinoid degradation enzyme MAGL *in vivo* using PET. A PET ligand can be useful to measure the expression of MAGL in various pathologies like (neuro)inflammation and various cancer types. MA-PB-1 is a structural analogue of JW642 where substitution of a phenoxy group with methoxy group provides (1) better affinity towards *h*MAGL, (2) lower clog D values and (3) enhanced brain penetration of MA-PB-1. [<sup>11</sup>C]MA-PB-1 was successfully synthesised with good radiochemical yields, high radiochemical purity, and molar activities. Significant brain uptake of [<sup>11</sup>C]MA-PB-1 was observed in biodistribution and microPET imaging experiments in mice, rats, and monkey. Self-blocking experiments confirmed the

specificity of binding. Blocking and chasing studies with the structurally non-related MAGL inhibitor MJN110 in mice, rats and monkey established [<sup>11</sup>C]MA-PB-1 as a MAGL specific irreversible tracer.

Another exciting target we studied is an endocannabinoid receptor CB<sub>2</sub>R. Low expression of CB<sub>2</sub>R is found in the healthy brain, whereas this expression is upregulated in microglia under neuroinflammatory conditions. Our group has previously reported two brain penetrable high-affinity agonist PET tracers [<sup>11</sup>C]MA2 and [<sup>18</sup>F]MA3 for CB<sub>2</sub>R. [<sup>18</sup>F]MA3 has 100-fold higher affinity for hCB<sub>2</sub>R compared to [<sup>11</sup>C]MA2. We further decided to study [<sup>18</sup>F]MA3 extensively in an animal model with local overexpression of hCB<sub>2</sub>R variant. To validate the developed hCB<sub>2</sub>R overexpressed animal model, we performed a microPET study with [<sup>11</sup>C]NE40 as a reference tracer and confirmed a high-intensity signal in the hCB<sub>2</sub>R injected striatum compared to control. Evaluation of [<sup>18</sup>F]MA3 in a rat model with local striatal overexpression of hCB<sub>2</sub>R showed specific and reversible tracer binding in the hCB<sub>2</sub> vector injected striatum, indicating that this tracer has the potential for *in vivo* imaging of the active state fraction of CB<sub>2</sub> receptors with PET.

Next potential target for visualization of neuro(inflammation), cancers and rheumatoid arthritis is CSF-1R. It is expressed on various cell types including macrophages, microglia, and osteoclasts. The activation and differentiation of microglia and macrophages depend on CSF-1R. From literature, we found a high affinity, favourable brain penetrable CSF-1R small molecule synthesised by Johnson and Johnson. [<sup>11</sup>C]BA-1 was synthesised with good radiochemical yields, high purities, and high molar activity. The preliminary biological evaluation confirmed high brain uptake in mouse, rat and monkey brains. Blocking experiments performed with non-radioactive reference did not result in tracer blocking in the rodent brain. We hypothesize that the high brain uptake is thus due to lysosomal trapping. Monkey brain PET studies confirmed high brain penetration of [<sup>11</sup>C]BA-1.

GPR84 is a potential target for neuroinflammation. GPR84 expression in the healthy brain is low but is upregulated during inflammatory conditions. To date, no antibodies are available for GPR84, hence it might be interesting to develop a PET probe to visualise GPR-84 *in vivo*. G611 is a structural analogue of GLPG1205 (GPR84 antagonist), [<sup>11</sup>C]G611 was synthesised in good radiochemical yields, high radiochemical purities, and high molar activities. The specificity of [<sup>11</sup>C]G611 was verified by cell binding experiments with GPR84 transduced HEK 293 cells and with control cells. A biodistribution study confirmed good uptake of [<sup>11</sup>C]G611 into mouse brain. LPS pretreatment induced increase tracer binding in mouse brain *in vivo* and in THP-1 cells *in vitro*. These preliminary results suggest a role for GPR84 in the neuroinflammatory process and warrant further studies to evaluate [<sup>11</sup>C]G611 in other models of neuroinflammation.

In conclusion, the thesis demonstrated synthesis and preclinical evaluation of four radiotracers for biomarkers that have been associated with neuroinflammation.

## SAMENVATTING

Neuroinflammatie is een complexe goed georkestreerde reactie op verschillende schadelijke stimuli die het herstel van weefselhomeostase beoogt maar onder bepaalde pathologische omstandigheden de weefselschade onverwacht versterkt. NI is betrokken bij verschillende CZS-pathologieën zoals AD, PD, beroerte, MS, ALS, HD, neoplasie en hersentrauma. Microglia zijn residente CNS-cellen met vergelijkbare functies als macrofagen. Activering van microglia is een primaire aanpassingsreactie van het aangeboren immuunsysteem van de hersenen, dat optreedt in fysiologische en pathologische omstandigheden [2]. Tijdens hersenbeschadiging migreren microglia snel naar de plaats van de verwonding, afhankelijk van de directionele begeleiding door lokale chemotactische verbindingen. Tijdens activatie ondergaan microglia functionele en morfologische veranderingen die gekoppeld zijn aan de modulatie van de expressie van verschillende receptoren, enzymen en ionkanalen [7]. Daarom is het zeer relevant om deze gemoduleerde proteïnen als biomerkers voor neuroinflammatie te kwantificeren. Een niet-invasieve nauwkeurige en betrouwbare detectie van neuroinflammatie is van fundamenteel klinisch belang. Microglia activatie kan in vivo gekwantificeerd worden met positronemissie tomografie (PET) beeldvorming op voorwaarde dat er een combinatie beschikbaar is van een relevant moleculair target en een geschikte radiotracer.

De onderhavige studie had als doel om een met koolstof-11 gemerkt radioligand te ontwikkelen om het endocannabinoïd degradatie-enzyme MAGL in vivo te visualiseren met behulp van PET. Een PET-ligand kan nuttig zijn om de expressie van MAGL te meten in verschillende pathologieën zoals (neuro)inflammatie en verschillende soorten kanker. MA-PB-1 is een structureel analoog van JW642, waarbij substitutie van een fenoxycgroep met methoxycgroep (1) een betere affiniteit voor hMAGL geeft, (2) de clogD-waarde verlaagt en (3) de hersenpenetratie van MA-PB-1 verbetert. [<sup>11</sup>C]MA-PB-1 werd met succes gesynthetiseerd met goede radiochemische opbrengsten, hoge radiochemische zuiverheid en hoge molaire activiteit.

Significante hersenopname van [<sup>11</sup>C]MA-PB-1 werd waargenomen bij biodistributie en microPET experimenten bij muizen, ratten en apen. Zelfblok experimenten bevestigden de specificiteit van de binding. Blokking en vrijzettingsexperimenten met de structureel niet-gerelateerde MAGL-remmer MJN110 bij muizen, ratten en apen toonde aan dat [<sup>11</sup>C]MA-PB-1 een irreversibele MAGL-specifieke tracer is.

CB2 receptoren hebben een lage expressiegraad op microglia in gezonde hersenen, terwijl deze expressie werd opgereguleerd in microglia onder neuro-inflammatoire omstandigheden. Onze onderzoeksgroep rapporteerde twee CB2 agonist PET-tracers met hoge affiniteit [<sup>11</sup>C]MA2 en [<sup>18</sup>F]MA3. [<sup>18</sup>F]MA3 heeft een 100-voudige hogere affiniteit voor hCB<sub>2</sub>R vergeleken met [<sup>11</sup>C]MA2. [<sup>18</sup>F]MA3 werd daarom uitgebreid bestudeerd in een diermodel met lokale overexpressie van de humane CB<sub>2</sub> receptor-(hCB<sub>2</sub>R) variant. Evaluatie van [<sup>18</sup>F]MA3 in een ratmodel met lokale striatale overexpressie van hCB<sub>2</sub>R toonde specifieke en omkeerbare tracerbinding aan in het hCB<sub>2</sub>-vector geïnjecteerde striatum, wat aangeeft dat deze tracer het potentieel heeft voor *in vivo* visualisatie van de actieve fractie van CB<sub>2</sub>-receptoren met PET .

Het volgende potentiële doelwit voor visualisatie van neuroinflammatie, kanker en reumatoïde artritis is CSF-1R. Dit wordt tot expressie gebracht op verschillende celtypes, waaronder macrofagen, microglia en osteoclasten. De activatie en differentiatie van microglia en macrofagen zijn afhankelijk van CSF-1R. In de literatuur vonden we een hoge affiniteit, CSF-1R-inhibitor gesynthetiseerd door Johnson en Johnson. [<sup>11</sup>C]BA-1 werd gesynthetiseerd met goede radiochemische opbrengsten, hoge zuiverheid en hoge molaire activiteit. De biologische evaluatie bevestigde een hoge opname in de hersenen bij muizen, ratten en apen. Blokkeringsexperimenten uitgevoerd met niet-radioactieve referentie vertoonden geen effect. We veronderstellen dat de waargenomen hersenopstapeling te wijten is aan lysosomale trapping.

GPR84 is een potentieel doelwit voor neuroinflammatie. GPR84-expressie in de gezonde hersenen is laag maar wordt opgereguleerd tijdens neuroinflammatie. Tot op heden zijn er geen antilichamen beschikbaar voor GPR84 daarom is het interessant om een PET-probe te ontwikkelen om GPR-84 te visualiseren. G611 is een structureel analoog van de GPR84-antagonist GLPG1205, [<sup>11</sup>C]G611 werd gesynthetiseerd met goede radiochemische opbrengst, hoge radiochemische zuiverheid en hoge molaire activiteit. De specificiteit van de [<sup>11</sup>C]G611 werd geverifieerd door celbindingsexperimenten met GPR84-getransduceerde HEK 293-cellen en met controlecellen. Een biodistributiestudie toonde een goede opname van [<sup>11</sup>C]G611 in muizenhersenen. Verdere studies toonden een verhoogde tracer-binding in muizenhersenen *in vivo* en in THP-1-cellen *in vitro* na LPS-voorbehandeling. Deze resultaten suggereren een rol voor GPR84 in het neuro-inflammatoire proces en rechtvaardigen verdere studies met [<sup>11</sup>C]G611 in andere modellen van neuroinflammatie.

Samengevat rapporteert het proefschrift de synthese en preklinische evaluatie van vier radiotracers voor biomerkers die in verband gebracht worden met neuroinflammatie.



# CURRICULUM VITAE

## *Personal information*

---

Name : Bala Narsa Nageswara Rao Attili (Bala Attili)  
Email : bala.attili@yahoo.com  
Date of birth : 29-06-1986  
Place of Birth : Paderu, Visakhapatnam, India

## *Experience*

---

### *o Professional experience*

2013-2014 : Marie-Curie Early Stage Researcher  
Debrecen-Hungary  
2012-2013 : Analyst LC-MS/MS  
3S Pharmacological Research, Bucharest-Romania  
2011-2012 : Assistant Professor  
St Paul's College of Pharmacy, Hyderabad-India

### *o Volunteering experience*

2018- Present : Treasurer at Marie-Curie Alumni Association  
2016-2018 : Board member at Marie-Curie Alumni Association

## *Education*

---

2014-2018 : PhD in Pharmaceutical Sciences, Radiopharmaceutical Chemistry,  
Laboratory for Radiopharmaceutical Research, KU Leuven, Belgium.  
Promoter: Prof. Guy Bormans  
2009-2011 : Masters of Pharmacy, first class with distinction.  
University College of Pharmacy, Andhra University, Visakhapatnam, India.  
2006-2009 : Bachelor of Pharmacy, first class with distinction.  
Jawaharlal Nehru Technological University, Kakinada, India.

## *Grants/Awards*

---

- o* Academische Stichting travel grant to attend Annual Neuroscience Congress (Washington DC).
- o* Marie Curie early-stage research fellowship.

## *Courses followed during Doctoral training*

---

- Positron Emission Tomography (PET) Technology and Application course, King's College London, UK.
- PET and SPECT radiopharmaceuticals development: radiosynthesis, preclinical evaluation, GMP and clinical dossier: Radiochemistry and tracer Development, Amsterdam, The Netherlands.
- Recent advances in Neuropathology and Applied Neurobiology, Cerebrovascular diseases: Genetics and Pathophysiology. Cirencester, UK.
- GCP Training course for experienced researchers, EU clinical trial directive and its implications.
- Training course on Technology & Knowledge Transfer Exploitation of Research, KU Leuven.
- Laboratory Animal Science, FELESA B, KU Leuven.

## *List of publications*

---

- Publications in international peer-reviewed journals

M. Ahamed\*, **B. Attili\***, D. van Veghel, M. Ooms, P. Berben, S. Celen, M. Koole, L. Declercq, J.R. Savinainen, J.T. Laitinen, A. Verbruggen, G. Bormans, Synthesis and preclinical evaluation of [<sup>11</sup>C]MA-PB-1 for in vivo imaging of brain monoacylglycerol lipase (MAGL), Eur. J. Med. Chem. 136 (2017). (\*Shared first author)

M. Ooms, **B. Attili**, S. Celen, M. Koole, A. Verbruggen, K. Van Laere, G. Bormans, [<sup>18</sup>F]JNJ42259152 binding to phosphodiesterase 10A, a key regulator of medium spiny neuron excitability, is altered in the presence of cyclic AMP, J. Neurochem. (2016).

**B. Attili**, S.Celen, M. Ahamed, M.Koole, C. Van den Haute, W. Vanduffel, G.Bormans, Preclinical evaluation of [<sup>18</sup>F]MA3, a CB2 receptor agonist radiotracer for Positron Emission Tomography, Manuscript under revision, British Journal of Pharmacology.

- Participation at international meetings

Synthesis and preclinical evaluation of [<sup>11</sup>C]BA-1, a PET tracer for brain CSF-1R at 47<sup>th</sup> Annual Neuroscience Congress-17, Washington DC, USA. Poster

Synthesis and preclinical evaluation of [<sup>11</sup>C]-BA-1 PET tracer for the imaging of CSF-1 receptors, ULLA Summer school-17, KU Leuven, Belgium. Poster

*In vitro* evaluation of M1/M2 phenotype TAMs & imaging of Translocator protein (TSPO) in brain tumors with [<sup>18</sup>F]DPA-714, BelNuc Congress-17, Ghent, Belgium. Oral presentation

*In vitro* Positron emission tomography imaging of Translocator protein (TSPO) in brain tumors-16, KU Leuven, Belgium. Flash and poster presentation.

Synthesis and preclinical evaluation of [<sup>11</sup>C]-BA-1 PET tracer for the imaging of CSF-1R. ESRR-16, Salzburg, Austria. Oral presentation.

Synthesis of new carbon-11 labelled PET tracers for visualisation of CSF-1 receptors. BelNuc Congress-15, Maastricht, the Netherlands, Poster

# SCIENTIFIC ACKNOWLEDGEMENT, PERSONAL CONTRIBUTION AND CONFLICT OF INTEREST

## 1. Scientific acknowledgement

I would like to thank Dr. Jacqueline Blankman (Abide Therapeutics, USA) for the useful discussions on MAGL work and Professor Wim Vanduffel and Christophe Ulens (Laboratory of Neuro-and Psychophysiology) for providing the Macaque monkeys and assisting with the monkey studies. I thank Julie Cornelis, Ivan Sannen and Pieter Haspeslagh (Laboratory for Radiopharmaceutical Research, KU Leuven) for their help with the animal studies. I would like to thank Galapagos NV, Belgium for their contribution in synthesis of reference and precursor, providing GPR84 transduce and control cells (HEK 293), THP-1 cells and help with qPCR studies (Chapter V).

I would like to extend my gratitude towards my funding agencies European Union's Seventh Framework Programme (FP7/2007-2013) under grant agreement no. HEALTH-F2-2011-278850 (INMiND), IMIR (In Vivo Molecular Imaging Research), MIRIAD (Molecular Imaging Research Initiative for Acceleration of Drug Development-130065) and Academische Stichting for providing conference travel grant.

## 2. Personal contribution

Chapter II in this thesis manuscript, I shared first authorship, my contributions include radiosynthesis, biological experiments, data evaluation, writing the manuscript and submission.

## 3. Conflict of interest

With regard to chapter V, Frederic Labeguere, Pieter Claes, Kenji Shoji, Xavier Bock, Johan Beeten, Romain Gosmini and Steve De Vos are employed by Galapagos.



## REFERENCES

- [1] A.H. Jacobs, B. Tavitian, INMiND consortium, Noninvasive molecular imaging of neuroinflammation, *J. Cereb. Blood Flow Metab.* 32 (2012) 1393–415. doi:10.1038/jcbfm.2012.53.
- [2] R. Medzhitov, Origin and physiological roles of inflammation, *Nature*. 454 (2008) 428–435. doi:10.1038/nature07201.
- [3] M.B. Graeber, W. Li, M.L. Rodriguez, Role of microglia in CNS inflammation, *FEBS Lett.* 585 (2011) 3798–3805. doi:10.1016/j.febslet.2011.08.033.
- [4] S. Rivest, Regulation of innate immune responses in the brain, *Nat. Rev. Immunol.* 9 (2009) 429–39. doi:10.1038/nri2565.
- [5] F. Ginhoux, M. Greter, M. Leboeuf, S. Nandi, P. See, S. Gokhan, M.F. Mehler, S.J. Conway, L.G. Ng, E.R. Stanley, I.M. Samokhvalov, M. Merad, Fate mapping analysis reveals that adult microglia derive from primitive macrophages, *Science*. 330 (2010) 841–845. doi:10.1126/science.1194637.
- [6] M. Prinz, J. Priller, Microglia and brain macrophages in the molecular age: from origin to neuropsychiatric disease, *Nat. Rev. Neurosci.* 15 (2014) 300–312. doi:10.1038/nrn3722.
- [7] C. Cerami, L. Iaccarino, D. Perani, Molecular Imaging of Neuroinflammation in Neurodegenerative Dementias: The Role of In Vivo PET Imaging, *Int. J. Mol. Sci.* 18 (2017) 993. doi:10.3390/ijms18050993.
- [8] M.T. Heneka, M.P. Kummer, E. Latz, Innate immune activation in neurodegenerative disease, *Nat. Rev. Immunol.* 14 (2014) 463–477. doi:10.1038/nri3705.
- [9] R.M. Ransohoff, A polarizing question: do M1 and M2 microglia exist?, *Nat. Neurosci.* 19 (2016) 987–991. doi:10.1038/nn.4338.
- [10] V.H. Perry, J.A.R. Nicoll, C. Holmes, Microglia in neurodegenerative disease, *Nat. Rev. Neurol.* 6 (2010) 193–201. doi:10.1038/nrneurol.2010.17.
- [11] S. Venneti, B.J. Lopresti, C.A. Wiley, Molecular imaging of microglia/macrophages in the brain, *Glia*. 61 (2013) 10–23. doi:10.1002/glia.22357.
- [12] R.S. Chekol, Development of Radiolabeled PET Tracers for In Vivo Visualization of Phosphodiesterase Type 5 (PDE5), 2014. <https://lirias.kuleuven.be/handle/123456789/442743>.
- [13] D. van Veghel, Development and biological evaluation of PET-tracers for in vivo visualisation of the endovanilloid/endocannabinoid system, 2013. <https://lirias.kuleuven.be/handle/123456789/373597>.
- [14] D. Ory, S. Celen, A. Verbruggen, G. Bormans, PET radioligands for in vivo visualization of neuroinflammation, *Curr. Pharm. Des.* 20 (2014) 5897–913.
- [15] N. Evens, G.M. Bormans, Non-invasive imaging of the type 2 cannabinoid receptor, focus on positron emission tomography, *Curr. Top. Med. Chem.* 10 (2010) 1527–43.
- [16] V.W. Pike, PET radiotracers: crossing the blood-brain barrier and surviving metabolism, *Trends Pharmacol. Sci.* 30 (2009) 431–40. doi:10.1016/j.tips.2009.05.005.
- [17] N. Denora, G. Natile, An Updated View of Translocator Protein (TSPO), *Int. J. Mol. Sci.* 18 (2017). doi:10.3390/ijms18122640.
- [18] V. Papadopoulos, M. Baraldi, T.R. Guilarte, T.B. Knudsen, J.-J. Lacapère, P. Lindemann, M.D. Norenberg, D. Nutt, A. Weizman, M.-R. Zhang, M. Gavish, Translocator protein (18kDa): new nomenclature for the peripheral-type benzodiazepine receptor based on its structure and molecular function, *Trends Pharmacol. Sci.* 27 (2006) 402–409. doi:10.1016/j.tips.2006.06.005.
- [19] A. Batareseh, V. Papadopoulos, Regulation of translocator protein 18 kDa (TSPO) expression in health and disease states, *Mol. Cell. Endocrinol.* 327 (2010) 1–12. doi:10.1016/j.mce.2010.06.013.
- [20] A. Winkeler, R. Boisgard, A.R. Awde, A. Dubois, B. Thézé, J. Zheng, L. Ciobanu, F. Dollé, T. Viel, A.H. Jacobs, B. Tavitian, The translocator protein ligand [<sup>18</sup>F]DPA-714 images glioma and activated microglia in vivo, *Eur. J. Nucl. Med. Mol. Imaging.* 39 (2012) 811–23. doi:10.1007/s00259-011-2041-4.
- [21] B. Janssen, D.J. Vugts, U. Funke, G.T. Molenaar, P.S. Kruijer, B.N.M. van Berckel, A.A. Lammertsma, A.D. Windhorst, Imaging of neuroinflammation in Alzheimer’s disease, multiple sclerosis and stroke: Recent developments in positron emission tomography, *Biochim. Biophys. Acta - Mol. Basis Dis.* 1862

- (2016) 425–441. doi:10.1016/j.bbadis.2015.11.011.
- [22] S. Lavisse, D. Garcia-Lorenzo, M.-A. Peyronneau, B. Bodini, C. Thiriez, B. Kuhnast, C. Comtat, P. Remy, B. Stankoff, M. Bottlaender, Optimized Quantification of Translocator Protein Radioligand 18F-DPA-714 Uptake in the Brain of Genotyped Healthy Volunteers, *J. Nucl. Med.* 56 (2015) 1048–1054. doi:10.2967/jnumed.115.156083.
- [23] C. Rojas, M. Stathis, J.M. Coughlin, M. Pomper, B.S. Slusher, The Low-Affinity Binding of Second Generation Radiotracers Targeting TSPO is Associated with a Unique Allosteric Binding Site, *J. Neuroimmune Pharmacol.* 13 (2018) 1–5. doi:10.1007/s11481-017-9765-2.
- [24] Q. Guo, A. Colasanti, D.R. Owen, M. Onega, A. Kamalakaran, I. Bennacef, P.M. Matthews, E.A. Rabiner, F.E. Turkheimer, R.N. Gunn, Quantification of the Specific Translocator Protein Signal of 18F-PBR111 in Healthy Humans: A Genetic Polymorphism Effect on In Vivo Binding, *J. Nucl. Med.* 54 (2013) 1915–1923. doi:10.2967/jnumed.113.121020.
- [25] D.R.J. Owen, R.N. Gunn, E.A. Rabiner, I. Bennacef, M. Fujita, W.C. Kreisl, R.B. Innis, V.W. Pike, R. Reynolds, P.M. Matthews, C.A. Parker, Mixed-Affinity Binding in Humans with 18-kDa Translocator Protein Ligands, *J. Nucl. Med.* 52 (2011) 24–32. doi:10.2967/jnumed.110.079459.
- [26] D.R. Owen, A.J. Yeo, R.N. Gunn, K. Song, G. Wadsworth, A. Lewis, C. Rhodes, D.J. Pulford, I. Bennacef, C.A. Parker, P.L. StJean, L.R. Cardon, V.E. Mooser, P.M. Matthews, E.A. Rabiner, J.P. Rubio, An 18-kDa Translocator Protein (TSPO) Polymorphism Explains Differences in Binding Affinity of the PET Radioligand PBR28, *J. Cereb. Blood Flow Metab.* 32 (2012) 1–5. doi:10.1038/jcbfm.2011.147.
- [27] M. Fujita, M. Kobayashi, M. Ikawa, R.N. Gunn, E.A. Rabiner, D.R. Owen, S.S. Zoghbi, M.B. Haskali, S. Telu, V.W. Pike, R.B. Innis, Comparison of four <sup>11</sup>C-labeled PET ligands to quantify translocator protein 18 kDa (TSPO) in human brain: (R)-PK11195, PBR28, DPA-713, and ER176—based on recent publications that measured specific-to-non-displaceable ratios, *EJNMMI Res.* 7 (2017) 84. doi:10.1186/s13550-017-0334-8.
- [28] C. Vicidomini, M. Panico, A. Greco, S. Gargiulo, A.R.D. Coda, A. Zannetti, M. Gramanzini, G.N. Roviello, M. Quarantelli, B. Alfano, B. Tavitian, F. Dollé, M. Salvatore, A. Brunetti, S. Pappatà, In vivo imaging and characterization of [(18)F]DPA-714, a potential new TSPO ligand, in mouse brain and peripheral tissues using small-animal PET, *Nucl. Med. Biol.* 42 (2015) 309–16. doi:10.1016/j.nucmedbio.2014.11.009.
- [29] M.-A. Peyronneau, W. Saba, S. Goutal, A. Damont, F. Dollé, M. Kassiou, M. Bottlaender, H. Valette, Metabolism and quantification of [(18)F]DPA-714, a new TSPO positron emission tomography radioligand, *Drug Metab. Dispos.* 41 (2013) 122–31. doi:10.1124/dmd.112.046342.
- [30] J. Marik, A. Ogasawara, B. Martin-McNulty, J. Ross, J.E. Flores, H.S. Gill, J.N. Tinianow, A.N. Vanderbilt, M. Nishimura, F. Peale, C. Pastuskovas, J.M. Greve, N. van Bruggen, S.P. Williams, PET of glial metabolism using 2-18F-fluoroacetate, *J. Nucl. Med.* 50 (2009) 982–90. doi:10.2967/jnumed.108.057356.
- [31] S.S. Zoghbi, H.U. Shetty, M. Ichise, M. Fujita, M. Imaizumi, J.-S. Liow, J. Shah, J.L. Musachio, V.W. Pike, R.B. Innis, PET imaging of the dopamine transporter with 18F-FECNT: a polar radiometabolite confounds brain radioligand measurements, *J. Nucl. Med.* 47 (2006) 520–7.
- [32] V. Médran-Navarrete, N. Bernards, B. Kuhnast, A. Damont, G. Pottier, M.-A. Peyronneau, M. Kassiou, F. Marguet, F. Puech, R. Boisgard, F. Dollé, [<sup>18</sup>F]DPA-C5yne, a novel fluorine-18-labelled analogue of DPA-714: radiosynthesis and preliminary evaluation as a radiotracer for imaging neuroinflammation with PET, *J. Label. Compd. Radiopharm.* 57 (2014) 410–418. doi:10.1002/jlcr.3199.
- [33] V. Médran-Navarrete, A. Damont, M.-A. Peyronneau, B. Kuhnast, N. Bernards, G. Pottier, F. Marguet, F. Puech, R. Boisgard, F. Dollé, Preparation and evaluation of novel pyrazolo[1,5-a]pyrimidine acetamides, closely related to DPA-714, as potent ligands for imaging the TSPO 18 kDa with PET, *Bioorg. Med. Chem. Lett.* 24 (2014) 1550–1556. doi:10.1016/J.BMCL.2014.01.080.
- [34] P. Zanotti-Fregonara, B. Pascual, G. Rizzo, M. Yu, N. Pal, D. Beers, R. Carter, S. Appel, N. Atassi, J. Masdeu, Head-to-head comparison of <sup>11</sup>C-PBR28 and <sup>18</sup>F-GE180 for the quantification of TSPO in the human brain, *J. Nucl. Med.* (2018) jnumed.117.203109. doi:10.2967/jnumed.117.203109.
- [35] J.R. Backstrom, G.P. Lim, M.J. Cullen, Z.A. Tökés, Matrix metalloproteinase-9 (MMP-9) is synthesized in neurons of the human hippocampus and is capable of degrading the amyloid-beta peptide, *J. Neurosci.* 16 (1996) 7910–9.

- [36] G.A. Rosenberg, Matrix metalloproteinases and their multiple roles in neurodegenerative diseases, *Lancet Neurol.* 8 (2009) 205–216. doi:10.1016/S1474-4422(09)70016-X.
- [37] S. V. Selivanova, T. Stellfeld, T.K. Heinrich, A. Müller, S.D. Krämer, P.A. Schubiger, R. Schibli, S.M. Ametamey, B. Vos, J. Meding, M. Bauser, J. Hütter, L.M. Dinkelborg, Design, Synthesis, and Initial Evaluation of a High Affinity Positron Emission Tomography Probe for Imaging Matrix Metalloproteinases 2 and 9, *J. Med. Chem.* 56 (2013) 4912–4920. doi:10.1021/jm400156p.
- [38] V. Hugenberg, B. Riemann, S. Hermann, O. Schober, M. Schäfers, K. Szardenings, A. Lebedev, U. Gangadharmath, H. Kolb, J. Walsh, W. Zhang, K. Kopka, S. Wagner, Inverse 1,2,3-Triazole-1-yl-ethyl Substituted Hydroxamates as Highly Potent Matrix Metalloproteinase Inhibitors: (Radio)synthesis, in Vitro and First in Vivo Evaluation, *J. Med. Chem.* 56 (2013) 6858–6870. doi:10.1021/jm4006753.
- [39] J.S. Fowler, J. Logan, E. Shumay, N. Alia-Klein, G.-J. Wang, N.D. Volkow, Monoamine oxidase: radiotracer chemistry and human studies, *J. Label. Compd. Radiopharm.* 58 (2015) 51–64. doi:10.1002/jlcr.3247.
- [40] E. Rodriguez-Vieitez, R. Ni, B. Gulyás, M. Tóth, J. Häggkvist, C. Halldin, L. Voytenko, A. Marutle, A. Nordberg, Astrocytosis precedes amyloid plaque deposition in Alzheimer APPswe transgenic mouse brain: a correlative positron emission tomography and in vitro imaging study, *Eur. J. Nucl. Med. Mol. Imaging.* 42 (2015) 1119–1132. doi:10.1007/s00259-015-3047-0.
- [41] S. Nag, L. Lehmann, G. Ketschau, T. Heinrich, A. Thiele, A. Varrone, B. Gulyas, C. Halldin, Synthesis and evaluation of [18F]fluororasagiline, a novel positron emission tomography (PET) radioligand for monoamine oxidase B (MAO-B), *Bioorg. Med. Chem.* 20 (2012) 3065–3071. doi:10.1016/J.BMC.2012.02.056.
- [42] S. Nag, L. Lehmann, G. Ketschau, M. Toth, T. Heinrich, A. Thiele, A. Varrone, C. Halldin, Development of a novel fluorine-18 labeled deuterated fluororasagiline ([18F]fluororasagiline-D2) radioligand for PET studies of monoamine oxidase B (MAO-B), *Bioorg. Med. Chem.* 21 (2013) 6634–6641. doi:10.1016/J.BMC.2013.08.019.
- [43] S. Nag, G. Ketschau, T. Heinrich, A. Varrone, L. Lehmann, B. Gulyas, A. Thiele, É. Keller, C. Halldin, Synthesis and biological evaluation of novel propargyl amines as potential fluorine-18 labeled radioligands for detection of MAO-B activity, *Bioorg. Med. Chem.* 21 (2013) 186–195. doi:10.1016/J.BMC.2012.10.050.
- [44] P.M. Rusjan, A.A. Wilson, L. Miler, I. Fan, R. Mizrahi, S. Houle, N. Vasdev, J.H. Meyer, Kinetic modeling of the monoamine oxidase B radioligand [<sup>11</sup>C]SL25.1188 in human brain with high-resolution positron emission tomography, *J. Cereb. Blood Flow Metab.* 34 (2014) 883–9. doi:10.1038/jcbfm.2014.34.
- [45] J.W. Hicks, O. Sadoyski, J. Parkes, S. Houle, B.A. Hay, R.L. Carter, A.A. Wilson, N. Vasdev, Radiosynthesis and ex vivo evaluation of [(18)F]-(S)-3-(6-(3-fluoropropoxy)benzo[d]isoxazol-3-yl)-5-(methoxymethyl)oxazolidin-2-one for imaging MAO-B with PET, *Bioorg. Med. Chem. Lett.* 25 (2015) 288–91. doi:10.1016/j.bmcl.2014.11.048.
- [46] B. Kis, J.A. Snipes, D.W. Busija, Acetaminophen and the cyclooxygenase-3 puzzle: sorting out facts, fictions, and uncertainties, *J. Pharmacol. Exp. Ther.* 315 (2005) 1–7. doi:10.1124/jpet.105.085431.
- [47] S. Aid, F. Bosetti, Targeting cyclooxygenases-1 and -2 in neuroinflammation: Therapeutic implications, *Biochimie.* 93 (2011) 46–51. doi:10.1016/j.biochi.2010.09.009.
- [48] J.M. Schwab, T.D. Nguyen, E. Postler, R. Meyermann, H.J. Schluesener, Selective accumulation of cyclooxygenase-1-expressing microglial cells/macrophages in lesions of human focal cerebral ischemia, *Acta Neuropathol.* 99 (2000) 609–14.
- [49] J.J.M. Hoozemans, J.M. Rozemuller, E.S. van Haastert, R. Veerhuis, P. Eikelenboom, Cyclooxygenase-1 and -2 in the different stages of Alzheimer's disease pathology, *Curr. Pharm. Des.* 14 (2008) 1419–27.
- [50] S.-H. Choi, S. Aid, F. Bosetti, The distinct roles of cyclooxygenase-1 and -2 in neuroinflammation: implications for translational research, *Trends Pharmacol. Sci.* 30 (2009) 174–181. doi:10.1016/j.tips.2009.01.002.
- [51] M. Takashima-Hirano, M. Shukuri, T. Takashima, M. Goto, Y. Wada, Y. Watanabe, H. Onoe, H. Doi, M. Suzuki, General Method for the <sup>11</sup>C-Labeling of 2-Arylpropionic Acids and Their Esters: Construction of a PET Tracer Library for a Study of Biological Events Involved in COXs Expression, *Chem. - A Eur. J.* 16 (2010) 4250–4258. doi:10.1002/chem.200903044.

- [52] M. Shukuri, M. Takashima-Hirano, K. Tokuda, T. Takashima, K. Matsumura, O. Inoue, H. Doi, M. Suzuki, Y. Watanabe, H. Onoe, In Vivo Expression of Cyclooxygenase-1 in Activated Microglia and Macrophages During Neuroinflammation Visualized by PET with <sup>11</sup>C-Ketoprofen Methyl Ester, *J. Nucl. Med.* 52 (2011) 1094–1101. doi:10.2967/jnumed.110.084046.
- [53] J. Prabhakaran, M.D. Underwood, R. V. Parsey, V. Arango, V.J. Majo, N.R. Simpson, R. Van Heertum, J.J. Mann, J.S.D. Kumar, Synthesis and in vivo evaluation of [<sup>18</sup>F]-4-[5-(4-methylphenyl)-3-(trifluoromethyl)-1H-pyrazol-1-yl]benzenesulfonamide as a PET imaging probe for COX-2 expression, *Bioorg. Med. Chem.* 15 (2007) 1802–1807. doi:10.1016/J.BMC.2006.11.033.
- [54] E.F.J. de Vries, J. Doorduyn, R.A. Dierckx, A. van Waarde, Evaluation of [<sup>11</sup>C]rofecoxib as PET tracer for cyclooxygenase 2 overexpression in rat models of inflammation, *Nucl. Med. Biol.* 35 (2008) 35–42. doi:10.1016/j.nucmedbio.2007.07.015.
- [55] O. Tietz, A. Marshall, M. Wuest, M. Wang, F. Wuest, Radiotracers for Molecular Imaging of Cyclooxygenase-2 (COX-2) Enzyme, *Curr. Med. Chem.* 20 (2013) 4350–4369. doi:10.2174/09298673113206660260.
- [56] B.B. Fredholm, K. Bättig, J. Holmén, A. Nehlig, E.E. Zvartau, K. Jacobson, P. Leff, M. Williams, Actions of caffeine in the brain with special reference to factors that contribute to its widespread use, *Pharmacol. Rev.* 51 (1999) 83–133.
- [57] Z.-G. Gao, K.A. Jacobson, Emerging adenosine receptor agonists, *Expert Opin. Emerg. Drugs.* 12 (2007) 479–492. doi:10.1517/14728214.12.3.479.
- [58] A.R. Santiago, F.I. Baptista, P.F. Santos, G. Cristóvão, A.F. Ambrósio, R.A. Cunha, C.A. Gomes, Role of Microglia Adenosine A<sub>2A</sub> Receptors in Retinal and Brain Neurodegenerative Diseases, *Mediators Inflamm.* (2014) 1–13. doi:10.1155/2014/465694.
- [59] K. Ishiwata, R. Furuta, J.-I. Shimada, S.-I. Ishii, K. Endo, F. Suzuki, M. Senda, Synthesis and preliminary evaluation of [<sup>11</sup>C]KF15372, a selective adenosine A<sub>1</sub> antagonist, *Appl. Radiat. Isot.* 46 (1995) 1009–1013. doi:10.1016/0969-8043(95)00197-L.
- [60] J. Noguchi, K. Ishiwata, S. Wakabayashi, T. Nariai, S. Shumiya, S. Ishii, H. Toyama, K. Endo, F. Suzuki, M. Senda, Evaluation of carbon-11-labeled KF17837: a potential CNS adenosine A<sub>2a</sub> receptor ligand, *J. Nucl. Med.* 39 (1998) 498–503.
- [61] Y. Shimada, K. Ishiwata, M. Kiyosawa, T. Nariai, K. Oda, H. Toyama, F. Suzuki, K. Ono, M. Senda, Mapping adenosine A<sub>1</sub> receptors in the cat brain by positron emission tomography with [<sup>11</sup>C]MPDX, *Nucl. Med. Biol.* 29 (2002) 29–37. doi:10.1016/S0969-8051(01)00265-7.
- [62] K. Ishiwata, T. Nariai, Y. Kimura, K. Oda, K. Kawamura, K. Ishii, M. Senda, S. Wakabayashi, J. Shimada, Preclinical studies on [<sup>11</sup>C]MPDX for mapping adenosine A<sub>1</sub> receptors by positron emission tomography, *Ann. Nucl. Med.* 16 (2002) 377–382. doi:10.1007/BF02990074.
- [63] S. Paul, S. Khanapur, W. Boersma, J.W. Sijbesma, K. Ishiwata, P.H. Elsinga, P. Meerlo, J. Doorduyn, R.A. Dierckx, A. van Waarde, Cerebral adenosine A<sub>1</sub> receptors are upregulated in rodent encephalitis, *Neuroimage.* 92 (2014) 83–89. doi:10.1016/J.NEUROIMAGE.2014.01.054.
- [64] D. Elmenhorst, T. Kroll, F. Wedekind, A. Weisshaupt, S. Beer, A. Bauer, In Vivo Kinetic and Steady-State Quantification of <sup>18</sup>F-CPFPX Binding to Rat Cerebral A<sub>1</sub> Adenosine Receptors: Validation by Displacement and Autoradiographic Experiments, *J. Nucl. Med.* 54 (2013) 1411–1419. doi:10.2967/jnumed.112.115576.
- [65] D. Elmenhorst, P.T. Meyer, A. Matusch, O.H. Winz, K. Zilles, A. Bauer, Test–retest stability of cerebral A<sub>1</sub> adenosine receptor quantification using [<sup>18</sup>F]CPFPX and PET, *Eur. J. Nucl. Med. Mol. Imaging.* 34 (2007) 1061–1070. doi:10.1007/s00259-006-0309-x.
- [66] M. Naganawa, M. Mishina, M. Sakata, K. Oda, M. Hiura, K. Ishii, K. Ishiwata, Test-retest variability of adenosine A<sub>2A</sub> binding in the human brain with [<sup>11</sup>C]-TMSX and PET, *EJNMMI Res.* 4 (2014) 76. doi:10.1186/s13550-014-0076-9.
- [67] E. Rissanen, J.R. Virta, T. Paavilainen, J. Tuisku, S. Helin, P. Luoto, R. Parkkola, J.O. Rinne, L. Airas, Adenosine A<sub>2A</sub> Receptors in Secondary Progressive Multiple Sclerosis: A [<sup>11</sup>C]TMSX Brain PET Study, *J. Cereb. Blood Flow Metab.* 33 (2013) 1394–1401. doi:10.1038/jcbfm.2013.85.
- [68] R.M. Moresco, S. Todde, S. Belloli, P. Simonelli, A. Panzacchi, M. Rigamonti, M. Galli-Kienle, F. Fazio, In vivo imaging of adenosine A<sub>2A</sub> receptors in rat and primate brain using [<sup>11</sup>C]SCH442416, *Eur. J. Nucl.*



- Med. Mol. Imaging. 32 (2005) 405–413. doi:10.1007/s00259-004-1688-5.
- [69] S. Khanapur, S. Paul, A. Shah, S. Vatakuti, M.J.B. Koole, R. Zijlma, R.A.J.O. Dierckx, G. Luurtsema, P. Garg, A. van Waarde, P.H. Elsinga, Development of [<sup>18</sup>F]-Labeled Pyrazolo[4,3-*e*]-1,2,4-triazolo[1,5-*c*]pyrimidine (SCH442416) Analogs for the Imaging of Cerebral Adenosine A<sub>2A</sub> Receptors with Positron Emission Tomography, *J. Med. Chem.* 57 (2014) 6765–6780. doi:10.1021/jm500700y.
- [70] X. Zhou, S. Khanapur, A.P. Huizing, R. Zijlma, M. Schepers, R.A.J.O. Dierckx, A. van Waarde, E.F.J. de Vries, P.H. Elsinga, Synthesis and Preclinical Evaluation of 2-(2-Furanyl)-7-[2-[4-[4-(2-[<sup>11</sup>C]methoxyethoxy)phenyl]-1-piperazinyl]ethyl]7 *H*-pyrazolo[4,3-*e*][1,2,4]triazolo[1,5-*c*]pyrimidine-5-amine ([<sup>11</sup>C]Preladenant) as a PET Tracer for the Imaging of Cerebral Adenosine A<sub>2A</sub> Receptors, *J. Med. Chem.* 57 (2014) 9204–9210. doi:10.1021/jm501065t.
- [71] M. Sakata, K. Ishibashi, M. Imai, K. Wagatsuma, K. Ishii, X. Zhou, E.F.J. De Vries, P.H. Elsinga, K. Ishiwata, J. Toyohara, Initial evaluation of an adenosine A<sub>2A</sub> Receptor ligand, [<sup>11</sup>C]-preladenant, in healthy human subjects, *J. Nucl. Med.* (2017). doi:10.2967/jnumed.116.188474.
- [72] X. Zhou, R. Boellaard, K. Ishiwata, M. Sakata, R.A.J.O. Dierckx, J.R. de Jong, S. Nishiyama, H. Ohba, H. Tsukada, E.F.J. de Vries, P.H. Elsinga, In Vivo Evaluation of [<sup>11</sup>C]Preladenant for PET Imaging of Adenosine A<sub>2A</sub> Receptors in the Conscious Monkey, *J. Nucl. Med.* (2017). doi:10.2967/jnumed.116.182410.
- [73] O. Barret, J. Hannestad, D. Alagille, C. Vala, A. Tavares, C. Papin, T. Morley, K. Fowles, H. Lee, J. Seibyl, D. Tytgat, M. Laruelle, G. Tamagnan, Adenosine 2A receptor occupancy by tozadenant and preladenant in rhesus monkeys, *J. Nucl. Med.* 55 (2014) 1712–8. doi:10.2967/jnumed.114.142067.
- [74] S.J. Hill, C.R. Ganellin, H. Timmerman, J.C. Schwartz, N.P. Shankley, J.M. Young, W. Schunack, R. Levi, H.L. Haas, International Union of Pharmacology. XIII. Classification of histamine receptors., *Pharmacol. Rev.* 49 (1997) 253–78.
- [75] M.B. Passani, C. Ballerini, Histamine and neuroinflammation: insights from murine experimental autoimmune encephalomyelitis, *Front. Syst. Neurosci.* 6 (2012) 32. doi:10.3389/fnsys.2012.00032.
- [76] U. Funke, D.J. Vugts, B. Janssen, A. Spaans, P.S. Kruijer, A.A. Lammertsma, L.R. Perk, A.D. Windhorst, [<sup>11</sup>C]-labeled and [<sup>18</sup>F]-labeled PET ligands for subtype-specific imaging of histamine receptors in the brain, *J. Label. Compd. Radiopharm.* 56 (2013) 120–129. doi:10.1002/jlcr.3038.
- [77] A. Bhattacharya, K. Biber, The microglial ATP-gated ion channel P2X<sub>7</sub> as a CNS drug target, *Glia.* 64 (2016) 1772–1787. doi:10.1002/glia.23001.
- [78] A. Bhattacharya, R.A. Neff, A.D. Wickenden, The physiology, pharmacology and future of P2X<sub>7</sub> as an analgesic drug target: hype or promise?, *Curr. Pharm. Biotechnol.* 12 (2011) 1698–706.
- [79] R. Bartlett, L. Stokes, R. Sluyter, The P2X<sub>7</sub> receptor channel: recent developments and the use of P2X<sub>7</sub> antagonists in models of disease, *Pharmacol. Rev.* 66 (2014) 638–75. doi:10.1124/pr.113.008003.
- [80] A. Masuch, C.-H. Shieh, N. van Rooijen, D. van Calker, K. Biber, Mechanism of microglia neuroprotection: Involvement of P2X<sub>7</sub>, TNF $\alpha$ , and valproic acid, *Glia.* 64 (2016) 76–89. doi:10.1002/glia.22904.
- [81] B. Sperl agh, P. Illes, P2X<sub>7</sub> receptor: an emerging target in central nervous system diseases, *Trends Pharmacol. Sci.* 35 (2014) 537–47. doi:10.1016/j.tips.2014.08.002.
- [82] C.C. Chrovian, J.C. Rech, A. Bhattacharya, M.A. Letavic, P2X<sub>7</sub> Antagonists as Potential Therapeutic Agents for the Treatment of CNS Disorders, *Prog. Med. Chem.* 53 (2014) 65–100. doi:10.1016/B978-0-444-63380-4.00002-0.
- [83] B. Janssen, D.J. Vugts, U. Funke, A. Spaans, R.C. Schuit, E. Kooijman, M. Rongen, L.R. Perk, A.A. Lammertsma, A.D. Windhorst, Synthesis and initial preclinical evaluation of the P2X<sub>7</sub> receptor antagonist [<sup>11</sup>C]A-740003 as a novel tracer of neuroinflammation, *J. Label. Compd. Radiopharm.* 57 (2014) 509–516. doi:10.1002/jlcr.3206.
- [84] D. Ory, S. Celen, R. Gijsbers, C. Van Den Haute, A. Postnov, M. Koole, C. Vandeputte, J.-I. Andres, J. Alcazar, M. De Angelis, X. Langlois, A. Bhattacharya, M. Schmidt, M.A. Letavic, W. Vanduffel, K. Van Laere, A. Verbruggen, Z. Debyser, G. Bormans, Preclinical Evaluation of a P2X<sub>7</sub> Receptor-Selective Radiotracer: PET Studies in a Rat Model with Local Overexpression of the Human P2X<sub>7</sub> Receptor and in Nonhuman Primates, *J. Nucl. Med.* 57 (2016) 1436–1441. doi:10.2967/jnumed.115.169995.
- [85] Final Report Summary - INMIND (Imaging of Neuroinflammation in Neurodegenerative Diseases), 2017.

[https://cordis.europa.eu/result/rcn/203157\\_en.html](https://cordis.europa.eu/result/rcn/203157_en.html).

- [86] A. Bhattacharya, Recent Advances in CNS P2X7 Physiology and Pharmacology: Focus on Neuropsychiatric Disorders, *Front. Pharmacol.* 9 (2018) 30. doi:10.3389/fphar.2018.00030.
- [87] B. Janssen, D.J. Vugts, S.M. Wilkinson, D. Ory, S. Chalon, J.J.M. Hoozemans, R.C. Schuit, W. Beaino, E.J.M. Kooijman, J. van den Hoek, M. Chishty, A. Doméné, A. Van der Perren, A. Villa, A. Maggi, G.T. Molenaar, U. Funke, R. V. Shevchenko, V. Baekelandt, G. Bormans, A.A. Lammertsma, M. Kassiou, A.D. Windhorst, Identification of the allosteric P2X7 receptor antagonist [11C]SMW139 as a PET tracer of microglial activation, *Sci. Rep.* 8 (2018) 6580. doi:10.1038/s41598-018-24814-0.
- [88] M. Gao, M. Wang, M.A. Green, G.D. Hutchins, Q.-H. Zheng, Synthesis of [11C]GSK1482160 as a new PET agent for targeting P2X7 receptor, *Bioorg. Med. Chem. Lett.* 25 (2015) 1965–1970. doi:10.1016/J.BMCL.2015.03.021.
- [89] P.R. Territo, J.A. Meyer, J.S. Peters, A.A. Riley, B.P. McCarthy, M. Gao, M. Wang, M.A. Green, Q.-H. Zheng, G.D. Hutchins, Characterization of 11C-GSK1482160 for Targeting the P2X7 Receptor as a Biomarker for Neuroinflammation, *J. Nucl. Med.* 58 (2017) 458–465. doi:10.2967/jnumed.116.181354.
- [90] J. Han, H. Liu, C. Liu, H. Jin, J.S. Perlmutter, T.M. Egan, Z. Tu, Pharmacologic characterizations of a P2X7 receptor-specific radioligand, [11C]GSK1482160 for neuroinflammatory response, *Nucl. Med. Commun.* 38 (2017) 372–382. doi:10.1097/MNM.0000000000000660.
- [91] E.R. Fantoni, D. Dal Ben, S. Falzoni, F. Di Virgilio, S. Lovestone, A. Gee, Design, synthesis and evaluation in an LPS rodent model of neuroinflammation of a novel 18F-labelled PET tracer targeting P2X7, *EJNMMI Res.* 7 (2017) 31. doi:10.1186/s13550-017-0275-2.
- [92] J.-W. Lee, H. Nam, S.-W. Yu, Systematic Analysis of Translocator Protein 18 kDa (TSPO) Ligands on Toll-like Receptors-mediated Pro-inflammatory Responses in Microglia and Astrocytes, *Exp. Neurobiol.* 25 (2016) 262. doi:10.5607/en.2016.25.5.262.
- [93] C. Tronel, B. Largeau, M. Santiago Ribeiro, D. Guilloteau, A.-C. Dupont, N. Arlicot, Molecular Targets for PET Imaging of Activated Microglia: The Current Situation and Future Expectations, *Int. J. Mol. Sci.* 18 (2017) 802. doi:10.3390/ijms18040802.
- [94] R.G. Pertwee, C. Howlett, M.E. Abood, S.P.H. Alexander, V. Di Marzo, M.R. Elphick, P.J. Greasley, H.S. Hansen, G. Kunos, International Union of Basic and Clinical Pharmacology. LXXIX. Cannabinoid Receptors and Their Ligands: Beyond CB1 and CB2, *Pharmacol. Rev.* 62 (2010) 588–631. doi:10.1124/pr.110.003004.588.
- [95] F. Spinelli, L. Mu, S.M. Ametamey, Radioligands for Positron Emission Tomography Imaging of Cannabinoid type 2 Receptor, *J. Label. Compd. Radiopharm.* (2017). doi:10.1002/jlcr.3579.
- [96] D. McHugh, GPR18 in microglia: Implications for the CNS and endocannabinoid system signalling, *Br. J. Pharmacol.* 167 (2012) 1575–1582. doi:10.1111/j.1476-5381.2012.02019.x.
- [97] L. Console-Bram, E. Brailoiu, G.C. Brailoiu, H. Sharir, M.E. Abood, Activation of GPR18 by cannabinoid compounds: A tale of biased agonism, *Br. J. Pharmacol.* 171 (2014) 3908–3917. doi:10.1111/bph.12746.
- [98] P. Pacher, S. Bátkai, G. Kunos, The Endocannabinoid System as an Emerging Target of Pharmacotherapy, *Pharmacol. Rev.* 58 (2006) 389–462. doi:10.1124/pr.58.3.2.
- [99] V. Di Marzo, D. Melck, T. Bisogno, L. De Petrocellis, Endocannabinoids: Endogenous cannabinoid receptor ligands with neuromodulatory action, *Trends Neurosci.* 21 (1998) 521–528. doi:10.1016/S0166-2236(98)01283-1.
- [100] K. Ahn, M.K. McKinney, B.F. Cravatt, Enzymatic pathways that regulate endocannabinoid signaling in the nervous system, *Chem. Rev.* 108 (2008) 1687–1707. doi:10.1021/cr0782067.
- [101] J.L. Blankman, G.M. Simon, B.F. Cravatt, A Comprehensive Profile of Brain Enzymes that Hydrolyze the Endocannabinoid 2-Arachidonoylglycerol, *Chem. Biol.* 14 (2007) 1347–1356. doi:10.1016/j.chembiol.2007.11.006.
- [102] J.R. Savinainen, S.M. Saario, J.T. Laitinen, The serine hydrolases MAGL, ABHD6 and ABHD12 as guardians of 2-arachidonoylglycerol signalling through cannabinoid receptors, *Acta Physiol.* 204 (2012) 267–276. doi:10.1111/j.1748-1716.2011.02280.x.
- [103] M.M. Mulvihill, D.K. Nomura, Therapeutic potential of monoacylglycerol lipase inhibitors, in: *Life Sci.*, 2013: pp. 492–497. doi:10.1016/j.lfs.2012.10.025.

- [104] J.W. Chang, M.J. Niphakis, K.M. Lum, A.B. Coggnetta, C. Wang, M.L. Matthews, S. Niessen, M.W. Buczynski, L.H. Parsons, B.F. Cravatt, Highly selective inhibitors of monoacylglycerol lipase bearing a reactive group that is bioisosteric with endocannabinoid substrates., *Chem. Biol.* 19 (2012) 579–88. doi:10.1016/j.chembiol.2012.03.009.
- [105] J.W. Hicks, J. Parkes, J. Tong, S. Houle, N. Vasdev, A.A. Wilson, Radiosynthesis and ex vivo evaluation of [11C-carbonyl]carbamate- and urea-based monoacylglycerol lipase inhibitors, *Nucl. Med. Biol.* 41 (2014) 688–694. doi:10.1016/j.nucmedbio.2014.05.001.
- [106] C. Wang, M.S. Placzek, G.C. Van De Bittner, F.A. Schroeder, J.M. Hooker, A Novel Radiotracer for Imaging Monoacylglycerol Lipase in the Brain Using Positron Emission Tomography, *ACS Chem. Neurosci.* 7 (2016) 484–489. doi:10.1021/acscchemneuro.5b00293.
- [107] L. Wang, W. Mori, R. Cheng, J. Yui, A. Hatori, L. Ma, Y. Zhang, B.H. Rotstein, M. Fujinaga, Y. Shimoda, T. Yamasaki, L. Xie, Y. Nagai, T. Minamimoto, M. Higuchi, N. Vasdev, M.R. Zhang, S.H. Liang, Synthesis and preclinical evaluation of sulfonamidobased [11C-Carbonyl]-carbamates and ureas for imaging monoacylglycerol lipase, *Theranostics.* 6 (2016) 1145–1159. doi:10.7150/thno.15257.
- [108] R. Cheng, W. Mori, L. Ma, M. Alhouayek, A. Hatori, Y. Zhang, D. Ogasawara, G. Yuan, Z. Chen, X. Zhang, H. Shi, T. Yamasaki, L. Xie, K. Kumata, M. Fujinaga, Y. Nagai, T. Minamimoto, M. Svensson, L. Wang, Y. Du, M.J. Ondrechen, N. Vasdev, B.F. Cravatt, C. Fowler, M.-R. Zhang, S.H. Liang, In Vitro and in Vivo Evaluation of <sup>11</sup>C-Labeled Azetidincarboxylates for Imaging Monoacylglycerol Lipase by PET Imaging Studies, *J. Med. Chem.* 61 (2018) 2278–2291. doi:10.1021/acs.jmedchem.7b01400.
- [109] H.D. Burns, K. Van Laere, S. Sanabria-Bohórquez, T.G. Hamill, G. Bormans, W. Eng, R. Gibson, C. Ryan, B. Connolly, S. Patel, S. Krause, A. Vanko, A. Van Hecken, P. Dupont, I. De Lepeleire, P. Rothenberg, S.A. Stoch, J. Cote, W.K. Hagmann, J.P. Jewell, L.S. Lin, P. Liu, M.T. Goulet, K. Gottesdiener, J.A. Wagner, J. de Hoon, L. Mortelmans, T.M. Fong, R.J. Hargreaves, [18F]MK-9470, a positron emission tomography (PET) tracer for in vivo human PET brain imaging of the cannabinoid-1 receptor, *Proc. Natl. Acad. Sci. U. S. A.* 104 (2007) 9800–5. doi:10.1073/pnas.0703472104.
- [110] B.K. Atwood, K. Mackie, CB2: a cannabinoid receptor with an identity crisis, *Br. J. Pharmacol.* 160 (2010) 467–479. doi:10.1111/j.1476-5381.2010.00729.x.
- [111] Y. Yiangou, P. Facer, P. Durrenberger, I.P. Chessell, A. Naylor, C. Bountra, R.R. Banati, P. Anand, COX-2, CB2 and P2X7-immunoreactivities are increased in activated microglial cells/macrophages of multiple sclerosis and amyotrophic lateral sclerosis spinal cord, *BMC Neurol.* 6 (2006) 12. doi:10.1186/1471-2377-6-12.
- [112] E. Núñez, C. Benito, R.M. Tolón, C.J. Hillard, W.S.T. Griffin, J. Romero, Glial expression of cannabinoid CB2 receptors and fatty acid amide hydrolase are beta amyloid-linked events in Down's syndrome, *Neuroscience.* 151 (2008) 104–110. doi:10.1016/J.NEUROSCIENCE.2007.10.029.
- [113] B. Cécyre, S. Thomas, M. Pfito, C. Casanova, J.-F. Bouchard, Evaluation of the specificity of antibodies raised against cannabinoid receptor type 2 in the mouse retina, *Naunyn. Schmiedebergs. Arch. Pharmacol.* 387 (2014) 175–184. doi:10.1007/s00210-013-0930-8.
- [114] B.K. Atwood, J. Wager-Miller, C. Haskins, A. Straiker, K. Mackie, Functional selectivity in CB2 cannabinoid receptor signaling and Regulation: Implications for the Therapeutic Potential of CB2 ligands, *Mol. Pharmacol.* 81 (2012) 250–63. doi:10.1124/mol.111.074013.
- [115] J. Guindon, G. Hohmann, Cannabinoid CB2 receptors: a therapeutic target for the treatment of inflammatory and neuropathic pain, *Br. J. Pharmacol.* 153 (2008) 319–334. doi:10.1038/sj.bjp.0707531.
- [116] A.G. Horti, Y. Gao, H.T. Ravert, P. Finley, H. Valentine, D.F. Wong, C.J. Endres, A. V. Savonenko, R.F. Dannals, Synthesis and biodistribution of [11C]A-836339, a new potential radioligand for PET imaging of cannabinoid type 2 receptors (CB2), *Bioorganic Med. Chem.* 18 (2010) 5202–5207. doi:10.1016/j.bmc.2010.05.058.
- [117] G. Pottier, V. Gómez-Vallejo, D. Padro, R. Boisgard, F. Dollé, J. Llop, A. Winkeler, A. Martín, PET imaging of cannabinoid type 2 receptors with [11C]A-836339 did not evidence changes following neuroinflammation in rats, *J. Cereb. Blood Flow Metab.* 37 (2017) 1163–1178. doi:10.1177/0271678X16685105.
- [118] R. Meletta, R. Slavik, L. Mu, Z. Rancic, N. Borel, R. Schibli, S.M. Ametamey, S.D. Krämer, A. Müller Herde, Cannabinoid receptor type 2 (CB2) as one of the candidate genes in human carotid plaque imaging: Evaluation of the novel radiotracer [11C]RS-016 targeting CB2 in atherosclerosis, *Nucl. Med. Biol.* 47

- (2017) 31–43. doi:10.1016/j.nucmedbio.2017.01.001.
- [119] F. Caillé, F. Cacheux, M.-A. Peyronneau, B. Jegou, E. Jaumain, G. Pottier, C. Ullmer, U. Grether, A. Winkeler, F. Dollé, A. Damont, B. Kuhnast, From Structure–Activity Relationships on Thiazole Derivatives to the *In Vivo* Evaluation of a New Radiotracer for Cannabinoid Subtype 2 PET Imaging, *Mol. Pharm.* (2017) acs.molpharmaceut.7b00746. doi:10.1021/acs.molpharmaceut.7b00746.
- [120] N. Evens, G.G. Muccioli, N. Houbrechts, D.M. Lambert, A.M. Verbruggen, K. Van Laere, G.M. Bormans, Synthesis and biological evaluation of carbon-11- and fluorine-18-labeled 2-oxoquinoline derivatives for type 2 cannabinoid receptor positron emission tomography imaging, 36 (2009). doi:10.1016/j.nucmedbio.2009.01.009.
- [121] N. Evens, C. Vandeputte, C. Coolen, P. Janssen, R. Sciot, V. Baekelandt, A.M. Verbruggen, Z. Debyser, K. Van Laere, G.M. Bormans, Preclinical evaluation of [<sup>11</sup>C]NE40, a type 2 cannabinoid receptor PET tracer, *Nucl. Med. Biol.* 39 (2012) 389–399. doi:10.1016/j.nucmedbio.2011.09.005.
- [122] R. Ahmad, M. Koole, N. Evens, K. Serdons, A. Verbruggen, G. Bormans, K. Van Laere, Whole-body biodistribution and radiation dosimetry of the cannabinoid type 2 receptor ligand [<sup>11</sup>C]-NE40 in healthy subjects, *Mol. Imaging Biol.* 15 (2013) 384–390. doi:10.1007/s11307-013-0626-y.
- [123] V. Chitu, E.R. Stanley, Colony-stimulating factor-1 in immunity and inflammation, *Curr. Opin. Immunol.* 18 (2006) 39–48. doi:10.1016/j.coi.2005.11.006.
- [124] E.R. Stanley, P.M. Heard, Factors regulating macrophage production and growth. Purification and some properties of the colony stimulating factor from medium conditioned by mouse L cells, *J. Biol. Chem.* 252 (1977) 4305–12.
- [125] H. Lin, E. Lee, K. Hestir, C. Leo, M. Huang, E. Bosch, R. Halenbeck, G. Wu, A. Zhou, D. Behrens, D. Hollenbaugh, T. Linnemann, M. Qin, J. Wong, K. Chu, S.K. Doberstein, L.T. Williams, Discovery of a cytokine and its receptor by functional screening of the extracellular proteome, *Science*. 320 (2008) 807–11. doi:10.1126/science.1154370.
- [126] V. Chitu, Ş. Gokhan, S. Nandi, M.F. Mehler, E.R. Stanley, Emerging Roles for CSF-1 Receptor and its Ligands in the Nervous System, *Trends Neurosci.* 39 (2016) 378–393. doi:10.1016/j.tins.2016.03.005.
- [127] M.I. El-Gamal, H.S. Anbar, K.H. Yoo, C.-H. Oh, FMS Kinase Inhibitors: Current Status and Future Prospects, *Med. Res. Rev.* 33 (2013) 599–636. doi:10.1002/med.21258.
- [128] M.I. El-Gamal, S.K. Al-Ameen, D.M. Al-Koumi, M.G. Hamad, N.A. Jalal, C.-H. Oh, Recent Advances of Colony-Stimulating Factor-1 Receptor (CSF-1R) Kinase and Its Inhibitors, *J. Med. Chem.* (2018) acs.jmedchem.7b00873. doi:10.1021/acs.jmedchem.7b00873.
- [129] S. Patel, M.R. Player, Colony-stimulating factor-1 receptor inhibitors for the treatment of cancer and inflammatory disease, *Curr. Top. Med. Chem.* 9 (2009) 599–610. doi:10.2174/156802609789007327.
- [130] C.H. Ries, S. Hoves, M.A. Cannarile, D. Rüttinger, CSF-1/CSF-1R targeting agents in clinical development for cancer therapy, *Curr. Opin. Pharmacol.* 23 (2015) 45–51. doi:10.1016/j.coph.2015.05.008.
- [131] M.R.P. Elmore, A.R. Najafi, M.A. Koike, N.N. Dagher, E.E. Spangenberg, R.A. Rice, M. Kitazawa, B. Matusow, H. Nguyen, B.L. West, K.N. Green, Colony-Stimulating Factor 1 Receptor Signaling Is Necessary for Microglia Viability, Unmasking a Microglia Progenitor Cell in the Adult Brain, *Neuron*. 82 (2014) 380–397. doi:10.1016/J.NEURON.2014.02.040.
- [132] A. Sica, T. Schioppa, A. Mantovani, P. Allavena, Tumour-associated macrophages are a distinct M2 polarised population promoting tumour progression: potential targets of anti-cancer therapy, *Eur. J. Cancer*. 42 (2006) 717–27. doi:10.1016/j.ejca.2006.01.003.
- [133] D. Achkova, J. Maher, Role of the colony-stimulating factor (CSF)/CSF-1 receptor axis in cancer, *Biochem. Soc. Trans.* 44 (2016) 333–341. doi:10.1042/BST20150245.
- [134] S. Chockalingam, S.S. Ghosh, Macrophage colony-stimulating factor and cancer: a review, *Tumor Biol.* 35 (2014) 10635–10644. doi:10.1007/s13277-014-2627-0.
- [135] S.M. Jung, K.W. Kim, C.-W. Yang, S.-H. Park, J.H. Ju, Cytokine-Mediated Bone Destruction in Rheumatoid Arthritis, *J. Immunol. Res.* 2014 (2014) 1–15. doi:10.1155/2014/263625.
- [136] C.R. Illig, J. Chen, M.J. Wall, K.J. Wilson, S.K. Ballentine, M.J. Rudolph, R.L. DesJarlais, Y. Chen, C. Schubert, I. Petronia, C.S. Crysler, C.J. Molloy, M.A. Chaikin, C.L. Manthey, M.R. Player, B.E.

- Tomczuk, S.K. Meegalla, Discovery of novel FMS kinase inhibitors as anti-inflammatory agents, (2008). doi:10.1016/j.bmcl.2008.01.059.
- [137] V. Bernard-Gauthier, R. Schirmacher, 5-(4-((4-[18F]fluorobenzyl)oxy)-3-methoxybenzyl)pyrimidine-2,4-diamine: A selective dual inhibitor for potential PET imaging of Trk/CSF-1R, *Bioorg. Med. Chem. Lett.* 24 (2014) 4784–4790. doi:10.1016/j.bmcl.2014.09.014.
- [138] T. Wittenberger, H.C. Schaller, S. Hellebrand, An expressed sequence tag (EST) data mining strategy succeeding in the discovery of new G-protein coupled receptors, *J. Mol. Biol.* 307 (2001) 799–813. doi:10.1006/jmbi.2001.4520.
- [139] C. Bouchard, J. Pagé, A. Bédard, P. Tremblay, L. Vallières, G protein-coupled receptor 84, a microglia-associated protein expressed in neuroinflammatory conditions, *Glia.* 55 (2007) 790–800. doi:10.1002/glia.20506.
- [140] H. Nagasaki, T. Kondo, M. Fuchigami, H. Hashimoto, Y. Sugimura, N. Ozaki, H. Arima, A. Ota, Y. Oiso, Y. Hamada, Inflammatory changes in adipose tissue enhance expression of GPR84, a medium-chain fatty acid receptor, *FEBS Lett.* 586 (2012) 368–372. doi:10.1016/j.febslet.2012.01.001.
- [141] M. Suzuki, S. Takaishi, M. Nagasaki, Y. Onozawa, I. Iino, H. Maeda, T. Komai, T. Oda, Medium-chain fatty acid-sensing receptor, GPR84, is a proinflammatory receptor, *J. Biol. Chem.* 288 (2013) 10684–91. doi:10.1074/jbc.M112.420042.
- [142] J. Wang, X. Wu, N. Simonavicius, H. Tian, L. Ling, Medium-chain Fatty Acids as Ligands for Orphan G Protein-coupled Receptor GPR84, *J. Biol. Chem.* 281 (2006) 34457–34464. doi:10.1074/jbc.M608019200.
- [143] D.Y. Oh, W.S. Lagakos, The role of G-protein-coupled receptors in mediating the effect of fatty acids on inflammation and insulin sensitivity, *Curr. Opin. Clin. Nutr. Metab. Care.* 14 (2011) 322–327. doi:10.1097/MCO.0b013e3283479230.
- [144] E.L. Gautier, T. Shay, J. Miller, M. Greter, C. Jakubzick, S. Ivanov, J. Helft, A. Chow, K.G. Elpek, S. Gordonov, A.R. Mazloom, A. Ma'ayan, W.-J. Chua, T.H. Hansen, S.J. Turley, M. Merad, G.J. Randolph, E.L. Gautier, C. Jakubzick, G.J. Randolph, A.J. Best, J. Knell, A. Goldrath, J. Miller, B. Brown, M. Merad, V. Jovic, D. Koller, N. Cohen, P. Brennan, M. Brenner, T. Shay, A. Regev, A. Fletcher, K. Elpek, A. Bellemare-Pelletier, D. Malhotra, S. Turley, R. Jianu, D. Laidlaw, J. Collins, K. Narayan, K. Sylvia, J. Kang, R. Gazit, B.S. Garrison, D.J. Rossi, F. Kim, T.N. Rao, A. Wagers, S.A. Shinton, R.R. Hardy, P. Monach, N.A. Bezman, J.C. Sun, C.C. Kim, L.L. Lanier, T. Heng, T. Kreslavsky, M. Painter, J. Ericson, S. Davis, D. Mathis, C. Benoist, Gene-expression profiles and transcriptional regulatory pathways that underlie the identity and diversity of mouse tissue macrophages, *Nat. Immunol.* 13 (2012) 1118–1128. doi:10.1038/ni.2419.
- [145] L. Wei, K. Tokizane, H. Konishi, H.-R. Yu, H. Kiyama, Agonists for G-protein-coupled receptor 84 (GPR84) alter cellular morphology and motility but do not induce pro-inflammatory responses in microglia, *J. Neuroinflammation.* 14 (2017) 198. doi:10.1186/s12974-017-0970-y.
- [146] J. Audoy-Rémus, L. Bozoyan, A. Dumas, M. Filali, C. Lecours, S. Lacroix, S. Rivest, M.-E. Tremblay, L. Vallières, GPR84 deficiency reduces microgliosis, but accelerates dendritic degeneration and cognitive decline in a mouse model of Alzheimer's disease, *Brain. Behav. Immun.* 46 (2015) 112–120. doi:10.1016/j.bbi.2015.01.010.
- [147] L.S.C. Nicol, J.M. Dawes, F. La Russa, A. Didangelos, A.K. Clark, C. Gentry, J. Grist, J.B. Davies, M. Malcangio, S.B. McMahon, The Role of G-Protein Receptor 84 in Experimental Neuropathic Pain, *J. Neurosci.* 35 (2015) 8959–8969. doi:10.1523/JNEUROSCI.3558-14.2015.
- [148] L.A. Matsuda, S.J. Lolait, M.J. Brownstein, A.C. Young, T.I. Bonner, Structure of a cannabinoid receptor and functional expression of the cloned cDNA, *Nature.* 346 (1990) 561–564. doi:10.1038/346561a0.
- [149] N. Aaltonen, C. Riera Ribas, M. Lehtonen, J.R. Savinainen, J.T. Laitinen, Brain regional cannabinoid CB1 receptor signalling and alternative enzymatic pathways for 2-arachidonoylglycerol generation in brain sections of diacylglycerol lipase deficient mice, *Eur. J. Pharm. Sci.* 51 (2014) 87–95. doi:10.1016/j.ejps.2013.08.035.
- [150] B.F. Cravatt, A.H. Lichtman, The endogenous cannabinoid system and its role in nociceptive behavior, *J. Neurobiol.* 61 (2004) 149–160. doi:10.1002/neu.20080.
- [151] R.A. Kohnz, D.K. Nomura, Chemical approaches to therapeutically target the metabolism and signaling of the endocannabinoid 2-AG and eicosanoids, *Chem. Soc. Rev.* 43 (2014) 6859–69.

doi:10.1039/c4cs00047a.

- [152] J.K. Makara, M. Mor, D. Fegley, S.I. Szabó, S. Kathuria, G. Astarita, A. Duranti, A. Tontini, G. Tarzia, S. Rivara, T.F. Freund, D. Piomelli, Selective inhibition of 2-AG hydrolysis enhances endocannabinoid signaling in hippocampus, *Nat. Neurosci.* 8 (2005) 1139–1141. doi:10.1038/nn1521.
- [153] D.K. Nomura, B.E. Morrison, J.L. Blankman, J.Z. Long, S.G. Kinsey, M.C.G. Marcondes, A.M. Ward, Y.K. Hahn, A.H. Lichtman, B. Conti, B.F. Cravatt, Endocannabinoid hydrolysis generates brain prostaglandins that promote neuroinflammation, *Science*. 334 (2011) 809–813. doi:10.1126/science.1209200.
- [154] Z. Cao, M.M. Mulvihill, P. Mukhopadhyay, H. Xu, K. Erdélyi, E. Hao, E. Holovac, G. Haskó, B.F. Cravatt, D.K. Nomura, P. Pacher, Monoacylglycerol lipase controls endocannabinoid and eicosanoid signaling and hepatic injury in mice, *Gastroenterology*. 144 (2013). doi:10.1053/j.gastro.2012.12.028.
- [155] C. Costola-de-Souza, A. Ribeiro, V. Ferraz-de-Paula, A.S. Calefi, T.P.A. Aloia, J.A. Gimenes-Júnior, V.I. de Almeida, M.L. Pinheiro, J. Palermo-Neto, Monoacylglycerol Lipase (MAGL) Inhibition Attenuates Acute Lung Injury in Mice, *PLoS One*. 8 (2013). doi:10.1371/journal.pone.0077706.
- [156] J.Z. Long, W. Li, L. Booker, J.J. Burston, S.G. Kinsey, J.E. Schlosburg, F.J. Pavón, A.M. Serrano, D.E. Selley, L.H. Parsons, A.H. Lichtman, B.F. Cravatt, Selective blockade of 2-arachidonoylglycerol hydrolysis produces cannabinoid behavioral effects, *Nat. Chem. Biol.* 5 (2009) 37–44. doi:10.1038/nchembio.129.
- [157] G. Hernández-Torres, M. Cipriano, E. Hedén, E. Björklund, Á. Canales, D. Zian, A. Feliú, M. Mecha, C. Guaza, C.J. Fowler, S. Ortega-Gutiérrez, M.L. López-Rodríguez, A Reversible and Selective Inhibitor of Monoacylglycerol Lipase Ameliorates Multiple Sclerosis, *Angew. Chemie Int. Ed.* 53 (2014) 13765–13770. doi:10.1002/anie.201407807.
- [158] L. Morera, G. Labar, G. Ortar, D.M. Lambert, Development and characterization of endocannabinoid hydrolases FAAH and MAGL inhibitors bearing a benzotriazol-1-yl carboxamide scaffold, *Bioorganic Med. Chem.* 20 (2012) 6260–6275. doi:10.1016/j.bmc.2012.09.011.
- [159] J.Z. Patel, S. Ahenkorah, M. Vaara, M. Staszewski, Y. Adams, T. Laitinen, D. Navia-Paldanius, T. Parkkari, J.R. Savinainen, K. Walczyński, J.T. Laitinen, T.J. Nevalainen, Loratadine analogues as MAGL inhibitors, *Bioorg. Med. Chem. Lett.* 25 (2015) 1436–1442. doi:10.1016/j.bmcl.2015.02.037.
- [160] N. Aaltonen, J.R. Savinainen, C.R. Ribas, J. Rönkkö, A. Kuusisto, J. Korhonen, D. Navia-Paldanius, J. Häyrynen, P. Takabe, H. Käsnänen, T. Pantsar, T. Laitinen, M. Lehtonen, S. Pasonen-Seppänen, A. Poso, T. Nevalainen, J.T. Laitinen, Piperazine and piperidine triazole ureas as ultrapotent and highly selective inhibitors of monoacylglycerol lipase, *Chem. Biol.* 20 (2013) 379–390. doi:10.1016/j.chembiol.2013.01.012.
- [161] R.N. Waterhouse, Determination of lipophilicity and its use as a predictor of blood-brain barrier penetration of molecular imaging agents, *Mol. Imaging Biol.* 5 (2003) 376–389. doi:10.1016/j.mibio.2003.09.014.
- [162] M.J. Niphakis, A.B. Coggnetta, J.W. Chang, M.W. Buczynski, L.H. Parsons, F. Byrne, J.J. Burston, V. Chapman, B.F. Cravatt, Evaluation of NHS carbamates as a potent and selective class of endocannabinoid hydrolase inhibitors, *ACS Chem. Neurosci.* 4 (2013) 1322–32. doi:10.1021/cn400116z.
- [163] J.R. Savinainen, E. Kansanen, T. Pantsar, D. Navia-Paldanius, T. Parkkari, M. Lehtonen, T. Laitinen, T. Nevalainen, A. Poso, A.-L. Levonen, J.T. Laitinen, Robust Hydrolysis of Prostaglandin Glycerol Esters by Human Monoacylglycerol Lipase (MAGL), *Mol. Pharmacol.* 86 (2014) 522–535. doi:10.1124/mol.114.094284.
- [164] D. Navia-Paldanius, J.R. Savinainen, J.T. Laitinen, Biochemical and pharmacological characterization of human  $\alpha/\beta$ -hydrolase domain containing 6 (ABHD6) and 12 (ABHD12), *J. Lipid Res.* 53 (2012) 2413–24. doi:10.1194/jlr.M030411.
- [165] C.J. Fielding, Monoglyceride hydrolase activities of rat plasma and platelets. Their properties and roles in the activity of lipoprotein lipase, *J. Biol. Chem.* 256 (1981) 876–81.
- [166] M. Karlsson, J.A. Contreras, U. Hellman, H. Tornqvist, C. Holm, cDNA cloning, tissue distribution, and identification of the catalytic triad of monoglyceride lipase. Evolutionary relationship to esterases, lysophospholipases, and haloperoxidases, *J. Biol. Chem.* 272 (1997) 27218–23.
- [167] J.-I. Andrés, M. De Angelis, J. Alcázar, L. Iturrino, X. Langlois, S. Dedeurwaerdere, I. Lenaerts, G.

- Vanhoof, S. Celen, G. Bormans, Synthesis, In Vivo Occupancy, and Radiolabeling of Potent Phosphodiesterase Subtype-10 Inhibitors as Candidates for Positron Emission Tomography Imaging, *J. Med. Chem.* 54 (2011) 5820–5835. doi:10.1021/jm200536d.
- [168] A.R. Fritzberg, W.P. Whitney, C.C. Kuni, W. Klingensmith, Biodistribution and renal excretion of  $^{99m}\text{Tc}$ -N,N'-bis-(mercaptoacetamido) ethylenediamine. Effect of renal tubular transport inhibitors, *Int. J. Nucl. Med. Biol.* 9 (1982) 79–82. doi:10.1016/0047-0740(82)90081-X.
- [169] C. Casteels, P. Vermaelen, J. Nuyts, A. Van Der Linden, V. Baekelandt, L. Mortelmans, G. Bormans, K. Van Laere, Construction and evaluation of multitracer small-animal PET probabilistic atlases for voxel-based functional mapping of the rat brain, *J. Nucl. Med.* 47 (2006) 1858–66.
- [170] C.C. Felder, K.E. Joyce, E.M. Briley, J. Mansouri, K. Mackie, O. Blond, Y. Lai, A.L. Ma, R.L. Mitchell, Comparison of the pharmacology and signal transduction of the human cannabinoid CB1 and CB2 receptors, *Mol. Pharmacol.* 48 (1995) 443–50.
- [171] P.D. Freund TF, Katona I, Role of Endogenous Cannabinoids in Synaptic Signaling, *Physiol. Rev.* 83 (2003) 1017–1066. doi:10.1152/physrev.00004.2003.
- [172] A.B. Lynn, M. Herkenham, Localization of cannabinoid receptors and nonsaturable high-density cannabinoid binding sites in peripheral tissues of the rat: implications for receptor-mediated immune modulation by cannabinoids., *J. Pharmacol. Exp. Ther.* 268 (1994) 1612–23.
- [173] R.-P. Moldovan, R. Teodoro, Y. Gao, W. Deuther-Conrad, M. Kranz, Y. Wang, H. Kuwabara, M. Nakano, H. Valentine, S. Fischer, M.G. Pomper, D.F. Wong, R.F. Dannals, P. Brust, A.G. Horti, Development of a High-Affinity PET Radioligand for Imaging Cannabinoid Subtype 2 Receptor, *J. Med. Chem.* 59 (2016) 7840–7855. doi:10.1021/acs.jmedchem.6b00554.
- [174] J.C. Ashton, M. Glass, The cannabinoid CB2 receptor as a target for inflammation-dependent neurodegeneration, *Curr. Neuropharmacol.* 5 (2007) 73–80. doi:10.2174/157015907780866884.
- [175] T. Cassano, S. Calcagnini, L. Pace, F. De Marco, A. Romano, S. Gaetani, Cannabinoid receptor 2 signaling in neurodegenerative disorders: From pathogenesis to a promising therapeutic target, *Front. Neurosci.* 11 (2017). doi:10.3389/fnins.2017.00030.
- [176] N. Evens, B. Bosier, B.J. Lavey, J.A. Kozlowski, P. Vermaelen, L. Baudemprez, R. Busson, D.M. Lambert, K. Van Laere, A.M. Verbruggen, G.M. Bormans, Labelling and biological evaluation of [ $^{11}\text{C}$ ]methoxy-Sch225336: a radioligand for the cannabinoid-type 2 receptor, *Nucl. Med. Biol.* 35 (2008) 793–800. doi:10.1016/j.nucmedbio.2008.07.004.
- [177] N. Evens, C. Vandeputte, G.G. Muccioli, D.M. Lambert, V. Baekelandt, A.M. Verbruggen, Z. Debyser, K. Van Laere, G.M. Bormans, Synthesis, in vitro and in vivo evaluation of fluorine-18 labelled FE-GW405833 as a PET tracer for type 2 cannabinoid receptor imaging, *Bioorg. Med. Chem.* 19 (2011) 4499–4505. doi:10.1016/j.bmc.2011.06.033.
- [178] N. Turkman, A. Shavrin, R.A. Ivanov, B. Rabinovich, A. Volgin, J.G. Gelovani, M.M. Alauddin, Fluorinated cannabinoid CB2 receptor ligands: Synthesis and in vitro binding characteristics of 2-oxoquinoline derivatives, *Bioorg. Med. Chem.* 19 (2011) 5698–5707. doi:10.1016/j.bmc.2011.07.062.
- [179] N. Turkman, A. Shavrin, V. Paolillo, H.H. Yeh, L. Flores, S. Soghomonian, B. Rabinovich, A. Volgin, J. Gelovani, M. Alauddin, Synthesis and preliminary evaluation of [ $^{18}\text{F}$ ]-labeled 2-oxoquinoline derivatives for PET imaging of cannabinoid CB2 receptor, *Nucl. Med. Biol.* 39 (2012) 593–600. doi:10.1016/j.nucmedbio.2011.10.019.
- [180] M. Ahamed, D. van Veghel, C. Ullmer, K. Van Laere, A. Verbruggen, G.M. Bormans, Synthesis, Biodistribution and In vitro Evaluation of Brain Permeable High Affinity Type 2 Cannabinoid Receptor Agonists [ $^{11}\text{C}$ ]MA2 and [ $^{18}\text{F}$ ]MA3, *Front. Neurosci.* 10 (2016) 431. doi:10.3389/fnins.2016.00431.
- [181] S. Gullapalli, D. Amrutkar, S. Gupta, M.R. Kandadi, H. Kumar, M. Gandhi, V. Karande, S. Narayanan, Characterization of active and inactive states of CB1 receptor and the differential binding state modulation by cannabinoid agonists, antagonists and inverse agonists, *Neuropharmacology.* 58 (2010) 1215–1219. doi:10.1016/j.neuropharm.2010.03.001.
- [182] C. Kilkenny, W. Browne, I.C. Cuthill, M. Emerson, D.G. Altman, NC3Rs Reporting Guidelines Working Group, Animal research: reporting in vivo experiments: the ARRIVE guidelines, *Br. J. Pharmacol.* 160 (2010) 1577–9. doi:10.1111/j.1476-5381.2010.00872.x.
- [183] J.C. McGrath, E. Lilley, Implementing guidelines on reporting research using animals (ARRIVE etc.):

- new requirements for publication in *BJP*, *Br. J. Pharmacol.* 172 (2015) 3189–3193. doi:10.1111/bph.12955.
- [184] C. Vandeputte, N. Evens, J. Toelen, C.M. Deroose, B. Bosier, A. Ibrahimi, A. Van der Perren, R. Gijssbers, P. Janssen, D.M. Lambert, A. Verbruggen, Z. Debyser, G. Bormans, V. Baekelandt, K. Van Laere, A PET Brain Reporter Gene System Based on Type 2 Cannabinoid Receptors, *J. Nucl. Med.* 52 (2011) 1102–1109. doi:10.2967/jnumed.110.084426.
- [185] M.J. Curtis, R.A. Bond, D. Spina, A. Ahluwalia, S.P.A. Alexander, M.A. Giembycz, A. Gilchrist, D. Hoyer, P.A. Insel, A.A. Izzo, A.J. Lawrence, D.J. MacEwan, L.D.F. Moon, S. Wonnacott, A.H. Weston, J.C. McGrath, Experimental design and analysis and their reporting: new guidance for publication in *BJP*, *Br. J. Pharmacol.* 172 (2015) 3461–3471. doi:10.1111/bph.12856.
- [186] C. Southan, J.L. Sharman, H.E. Benson, E. Faccenda, A.J. Pawson, S.P.H. Alexander, O.P. Buneman, A.P. Davenport, J.C. McGrath, J.A. Peters, M. Spedding, W.A. Catterall, D. Fabbro, J.A. Davies, NC-IUPHAR, The IUPHAR/BPS Guide to PHARMACOLOGY in 2016: towards curated quantitative interactions between 1300 protein targets and 6000 ligands, *Nucleic Acids Res.* 44 (2016) D1054–68. doi:10.1093/nar/gkv1037.
- [187] S.P. Alexander, A. Christopoulos, A.P. Davenport, E. Kelly, N. V Marrion, J.A. Peters, E. Faccenda, S.D. Harding, A.J. Pawson, J.L. Sharman, C. Southan, J.A. Davies, CGTP Collaborators, THE CONCISE GUIDE TO PHARMACOLOGY 2017/18: G protein-coupled receptors, *Br. J. Pharmacol.* 174 (2017) S17–S129. doi:10.1111/bph.13878.
- [188] J. Luo, F. Elwood, M. Britschgi, S. Villeda, H. Zhang, Z. Ding, L. Zhu, H. Alabsi, R. Getachew, R. Narasimhan, R. Wabl, N. Fainberg, M.L. James, G. Wong, J. Relton, S.S. Gambhir, J.W. Pollard, T. Wyss-Coray, Colony-stimulating factor 1 receptor (CSF1R) signaling in injured neurons facilitates protection and survival, *J. Exp. Med.* 210 (2013) 157–72. doi:10.1084/jem.20120412.
- [189] A.-J. Hao, S. Dheen, E.-A. Ling, Expression of macrophage colony-stimulating factor and its receptor in microglia activation is linked to teratogen-induced neuronal damage, *Neuroscience.* 112 (2002) 889–900. doi:10.1016/S0306-4522(02)00144-6.
- [190] S.M. Pyonteck, L. Akkari, A.J. Schuhmacher, R.L. Bowman, L. Sevenich, D.F. Quail, O.C. Olson, M.L. Quick, J.T. Huse, V. Teijeiro, M. Setty, C.S. Leslie, Y. Oei, A. Pedraza, J. Zhang, C.W. Brennan, J.C. Sutton, E.C. Holland, D. Daniel, J.A. Joyce, CSF-1R inhibition alters macrophage polarization and blocks glioma progression, *Nat. Med.* 19 (2013) 1264–1272. doi:10.1038/nm.3337.
- [191] N. Butowski, H. Colman, J.F. De Groot, A.M. Omuro, L. Nayak, P.Y. Wen, T.F. Cloughesy, A. Marimuthu, S. Haidar, A. Perry, J. Huse, J. Phillips, B.L. West, K.B. Nolop, H.H. Hsu, K.L. Ligon, A.M. Molinaro, M. Prados, Orally administered colony stimulating factor 1 receptor inhibitor PLX3397 in recurrent glioblastoma: an Ivy Foundation Early Phase Clinical Trials Consortium phase II study, *Neuro. Oncol.* 18 (2016) 557–564. doi:10.1093/neuonc/nov245.
- [192] J.G. van den Boorn, G. Hartmann, Therapeutic tissue regeneration by a macrophage colony-stimulating factor Fc conjugate, *Mol. Ther.* 22 (2014) 1577–9. doi:10.1038/mt.2014.150.
- [193] H. Moriyama, T. Yamamoto, H. Takatsuka, H. Umezu, K. Tokunaga, T. Nagano, M. Arakawa, M. Naito, Expression of macrophage colony-stimulating factor and its receptor in hepatic granulomas of Kupffer-cell-depleted mice, *Am. J. Pathol.* 150 (1997) 2047–60.
- [194] Z. Al Mahmud, L. Jenkins, T. Ulven, F. Labéguère, R. Gosmini, S. De Vos, B.D. Hudson, I.G. Tikhonova, G. Milligan, Three classes of ligands each bind to distinct sites on the orphan G protein-coupled receptor GPR84, *Sci. Rep.* 7 (2017) 17953. doi:10.1038/s41598-017-18159-3.
- [195] S. Yousefi, P.R. Cooper, S.L. Potter, B. Mueck, G. Jarai, Cloning and expression analysis of a novel G-protein-coupled receptor selectively expressed on granulocytes, *J. Leukoc. Biol.* 69 (2001) 1045–1052. doi:10.1189/JLB.69.6.1045.
- [196] C. Venkataraman, F. Kuo, The G-protein coupled receptor, GPR84 regulates IL-4 production by T lymphocytes in response to CD3 crosslinking, *Immunol. Lett.* 101 (2005) 144–153. doi:10.1016/j.imlet.2005.05.010.
- [197] M. Greter, I. Lelios, A.L. Croxford, Microglia Versus Myeloid Cell Nomenclature during Brain Inflammation., *Front. Immunol.* 6 (2015) 249. doi:10.3389/fimmu.2015.00249.
- [198] F.L. Heppner, M. Greter, D. Marino, J. Falsig, G. Raivich, N. Hövelmeyer, A. Waisman, T. Rüllicke, M. Prinz, J. Priller, B. Becher, A. Aguzzi, Experimental autoimmune encephalomyelitis repressed by



- microglial paralysis, *Nat. Med.* 11 (2005) 146–152. doi:10.1038/nm1177.
- [199] N.W. DeLapp, W.H. Gough, S.D. Kahl, A.C. Porter, T.R. Wiernicki, *GTP $\gamma$ S Binding Assays*, Eli Lilly & Company and the National Center for Advancing Translational Sciences, 2004.
- [200] R. Imperatore, G. Morello, L. Luongo, U. Taschler, R. Romano, D. De Gregorio, C. Belardo, S. Maione, V. Di Marzo, L. Cristino, Genetic deletion of monoacylglycerol lipase leads to impaired cannabinoid receptor CB<sub>1</sub>R signaling and anxiety-like behavior, *J. Neurochem.* 135 (2015) 799–813. doi:10.1111/jnc.13267.
- [201] R. Chen, J. Zhang, Y. Wu, D. Wang, G. Feng, Y.-P. Tang, Z. Teng, C. Chen, Monoacylglycerol Lipase Is a Therapeutic Target for Alzheimer’s Disease, *Cell Rep.* 2 (2012) 1329–1339. doi:10.1016/J.CELREP.2012.09.030.
- [202] R. Pihlaja, J. Takkinen, O. Eskola, J. Vasara, F.R. López-Picón, M. Haaparanta-Solin, J.O. Rinne, Monoacylglycerol lipase inhibitor JZL184 reduces neuroinflammatory response in APdE9 mice and in adult mouse glial cells, *J. Neuroinflammation.* 12 (2015) 81. doi:10.1186/s12974-015-0305-9.
- [203] D.K. Nomura, D.P. Lombardi, J.W. Chang, S. Niessen, A.M. Ward, J.Z. Long, H.H. Hoover, B.F. Cravatt, Monoacylglycerol Lipase Exerts Dual Control over Endocannabinoid and Fatty Acid Pathways to Support Prostate Cancer, *Chem. Biol.* 18 (2011) 846–856. doi:10.1016/j.chembiol.2011.05.009.
- [204] A. Savonenko, T. Melnikova, Y. Wang, H. Ravert, Y. Gao, J. Koppel, D. Lee, O. Pletnikova, E. Cho, N. Sayyida, A. Hiatt, J. Troncoso, P. Davies, R.F. Dannals, M.G. Pomper, A.G. Horti, Cannabinoid CB<sub>2</sub> Receptors in a Mouse Model of A $\beta$  Amyloidosis: Immunohistochemical Analysis and Suitability as a PET Biomarker of Neuroinflammation, *PLoS One.* 10 (2015) e0129618. doi:10.1371/journal.pone.0129618.
- [205] M. Fernández-Trapero, F. Espejo-Porras, C. Rodríguez-Cueto, J.R. Coates, C. Pérez-Díaz, E. de Lago, J. Fernández-Ruiz, Upregulation of CB<sub>2</sub> receptors in reactive astrocytes in canine degenerative myelopathy, a disease model of amyotrophic lateral sclerosis, *Dis. Model. Mech.* 10 (2017) 551–558. doi:10.1242/dmm.028373.
- [206] M.L. De Jesús, C. Hostalot, J.M. Garibi, J. Sallés, J.J. Meana, L.F. Callado, Opposite changes in cannabinoid CB<sub>1</sub> and CB<sub>2</sub> receptor expression in human gliomas, *Neurochem. Int.* 56 (2010) 829–33. doi:10.1016/j.neuint.2010.03.007.
- [207] J. Sosna, S. Philipp, R. Albay, J.M. Reyes-Ruiz, D. Baglietto-Vargas, F.M. LaFerla, C.G. Glabe, Early long-term administration of the CSF1R inhibitor PLX3397 ablates microglia and reduces accumulation of intraneuronal amyloid, neuritic plaque deposition and pre-fibrillar oligomers in 5XFAD mouse model of Alzheimer’s disease, *Mol. Neurodegener.* 13 (2018) 11. doi:10.1186/s13024-018-0244-x.
- [208] A. Olmos-Alonso, S.T.T. Schettters, S. Sri, K. Askew, R. Mancuso, M. Vargas-Caballero, C. Holscher, V.H. Perry, D. Gomez-Nicola, Pharmacological targeting of CSF1R inhibits microglial proliferation and prevents the progression of Alzheimer’s-like pathology, *Brain.* 139 (2016) 891–907. doi:10.1093/brain/awv379.
- [209] A.C. Knight, S.A. Brill, S.E. Queen, P.M. Tarwater, J.L. Mankowski, Increased Microglial CSF1R Expression in the SIV/Macaque Model of HIV CNS Disease, *J. Neuropathol. Exp. Neurol.* 77 (2018) 199–206. doi:10.1093/jnen/nlx115.
- [210] S.J. Coniglio, E. Eugenin, K. Dobrenis, E.R. Stanley, B.L. West, M.H. Symons, J.E. Segall, Microglial stimulation of glioblastoma invasion involves epidermal growth factor receptor (EGFR) and colony stimulating factor 1 receptor (CSF-1R) signaling, *Mol. Med.* 18 (2012) 519–27. doi:10.2119/molmed.2011.00217.
- [211] F. Navarrete, M.S. García-Gutiérrez, A. Aracil-Fernández, J.L. Lanciego, J. Manzanares, Cannabinoid CB<sub>1</sub> and CB<sub>2</sub> Receptors, and Monoacylglycerol Lipase Gene Expression Alterations in the Basal Ganglia of Patients with Parkinson’s Disease, *Neurotherapeutics.* (2018). doi:10.1007/s13311-018-0603-x.
- [212] H. Feldwisch-Drentrup, New clues to why a French drug trial went horribly wrong, *Science* (80-. ). (2017). doi:10.1126/science.aan6949.
- [213] A.C.M. van Esbroeck, A.P.A. Janssen, A.B. Cognetta, D. Ogasawara, G. Shpak, M. van der Kroeg, V. Kantae, M.P. Baggelaar, F.M.S. de Vrij, H. Deng, M. Allarà, F. Fezza, Z. Lin, T. van der Wel, M. Soethoudt, E.D. Mock, H. den Dulk, I.L. Baak, B.I. Florea, G. Hendriks, L. De Petrocellis, H.S. Overkleeft, T. Hankemeier, C.I. De Zeeuw, V. Di Marzo, M. Maccarrone, B.F. Cravatt, S.A. Kushner, M. van der Stelt, Activity-based protein profiling reveals off-target proteins of the FAAH inhibitor BIA 10-2474, *Science.* 356 (2017) 1084–1087. doi:10.1126/science.aaf7497.

- [214] L.A. McAllister, C.R. Butler, S. Mente, S. V. O'Neil, K.R. Fonseca, J.R. Piro, J.A. Cianfrogna, T.L. Foley, A.M. Gilbert, A.R. Harris, C.J. Helal, D.S. Johnson, J.I. Montgomery, D.M. Nason, S. Noell, J. Pandit, B.N. Rogers, T.A. Samad, C.L. Shaffer, R.G. da Silva, D.P. Uccello, D. Webb, M.A. Brodney, Discovery of Trifluoromethyl Glycol Carbamates as Potent and Selective Covalent Monoacylglycerol Lipase (MAGL) Inhibitors for Treatment of Neuroinflammation, *J. Med. Chem.* 61 (2018) 3008–3026. doi:10.1021/acs.jmedchem.8b00070.
- [215] C. Granchi, I. Caligiuri, E. Bertelli, G. Poli, F. Rizzolio, M. Macchia, A. Martinelli, F. Minutolo, T. Tuccinardi, Development of terphenyl-2-methyloxazol-5(4*H*)-one derivatives as selective reversible MAGL inhibitors, *J. Enzyme Inhib. Med. Chem.* 32 (2017) 1240–1252. doi:10.1080/14756366.2017.1375484.
- [216] M. Aghazadeh Tabrizi, P.G. Baraldi, S. Baraldi, E. Ruggiero, L. De Stefano, F. Rizzolio, L. Di Cesare Mannelli, C. Ghelardini, A. Chicca, M. Lapillo, J. Gertsch, C. Manera, M. Macchia, A. Martinelli, C. Granchi, F. Minutolo, T. Tuccinardi, Discovery of 1,5-Diphenylpyrazole-3-Carboxamide Derivatives as Potent, Reversible, and Selective Monoacylglycerol Lipase (MAGL) Inhibitors, *J. Med. Chem.* 61 (2018) 1340–1354. doi:10.1021/acs.jmedchem.7b01845.
- [217] Q. Tao, M.E. Abood, Mutation of a highly conserved aspartate residue in the second transmembrane domain of the cannabinoid receptors, CB1 and CB2, disrupts G-protein coupling, *J. Pharmacol. Exp. Ther.* 285 (1998) 651–8.
- [218] G.A. Cabral, L. Griffin-Thomas, Emerging role of the cannabinoid receptor CB2 in immune regulation: therapeutic prospects for neuroinflammation, *Expert Rev. Mol. Med.* 11 (2009) e3. doi:10.1017/S1462399409000957.
- [219] E. Aso, I. Ferrer, CB2 Cannabinoid Receptor As Potential Target against Alzheimer's Disease, *Front. Neurosci.* 10 (2016) 243. doi:10.3389/fnins.2016.00243.
- [220] F. Kazmi, T. Hensley, C. Pope, R.S. Funk, G.J. Loewen, D.B. Buckley, A. Parkinson XenoTech, Lysosomal Sequestration (Trapping) of Lipophilic Amine (Cationic Amphiphilic) Drugs in Immortalized Human Hepatocytes (Fa2N-4 Cells), *DRUG Metab. Dispos. Drug Metab Dispos.* 41 (2013) 897–905. doi:10.1124/dmd.112.050054.
- [221] R. Chekol, O. Gheysens, M. Ahamed, J. Cleynhens, P. Pokreisz, G. Vanhoof, S. Janssens, A. Verbruggen, G. Bormans, Carbon-11 and Fluorine-18 Radiolabeled Pyridopyrazinone Derivatives for Positron Emission Tomography (PET) Imaging of Phosphodiesterase-5 (PDE5), *J. Med. Chem.* 60 (2017) 486–496. doi:10.1021/acs.jmedchem.6b01666.
- [222] S. Garcia, L.M. Hartkamp, B. Malvar-Fernandez, I.E. van Es, H. Lin, J. Wong, L. Long, J.A. Zanghi, A.L. Rankin, E.L. Masteller, B.R. Wong, T.R.D.J. Radstake, P.P. Tak, K.A. Reedquist, Colony-stimulating factor (CSF) 1 receptor blockade reduces inflammation in human and murine models of rheumatoid arthritis, *Arthritis Res. Ther.* 18 (2016) 75. doi:10.1186/s13075-016-0973-6.